PH.D. THESIS

The development of applications for components selection to the ejector refrigeration systems, driven by low-temperature waste heat from industrial processes, based on the mathematical model and the experiments on the prototype refrigeration aggregats

Author:
Mikołaj MASTROWSKI

Supervisors:
Jacek SMOŁKA
Dariusz BUTRYMOWICZ
Łukasz ANTCZAK

Silesian University of Technology

Scientific discipline: Environmental Engineering, Mining and Energy

Gliwice, Poland, 2024

Author:
Mikołaj Mastrowski, M.Sc.
Silesian University of Technology
Faculty of Energy and Environmental Engineering
Department of Thermal Technology
Konarskiego 22, 44-100 Gliwice, Poland
e-mail: mikolaj.mastrowski@polsl.pl

Supervisor:
Prof. Jacek Smołka
Silesian University of Technology
Faculty of Energy and Environmental Engineering
Department of Thermal Technology
Konarskiego 22, 44-100 Gliwice, Poland
e-mail: jacek.smolka@polsl.pl

Supervisor:
Prof. Dariusz Butrymowicz
Bialystok University of Technology
Faculty of Mechanical Engineering
Wiejska 45C, 15-351 Białystok, Poland
e-mail: d.butrymowicz@pb.edu.pl

Assistant Supervisor:
Łukasz Antczak, Ph.D.
Marani Ltd.
Research and Development Department
Szybowa 14C, 41-808 Zabrze, Poland
e-mail: antczak@marani.pl

Polish title:
Opracowanie aplikacji do doboru komponentów dla strumienicowych układów chłodniczych napędzanych niskotemperaturowym ciepłem odpadowym z procesów przemysłowych na podstawie modelu obliczeniowego i pomiarów eksperymentalnych na prototypowych agregatach chłodniczych

to my dearest wife Magdalena and
daughter Ula

Acknowledgements

I want to express my deep gratitude to Dr Marek Madej, President of MARANI Ltd., for employing me in a research project to develop prototypes of ejector cooling systems and allowing me to work on PhD thesis. I thank him for the confidence he has shown, the prospect of growth as a researcher he has given me, and his incredible willingness to develop the company by increasing the competence of its employees. I thank him for his support in research and other tasks and for never refusing to help me.

I wish to convey my heartfelt thanks to my supervisor, Prof. Jacek Smolka, for his instrumental role in shaping my scientific work. His guidance, advice, and vast experience have been invaluable. I am very grateful for his time spent in meetings, reviewing my work, and helping solve many formal issues related to my Ph.D. thesis.

Allow me to express my most profound appreciation to my supervisor, Prof. Dariusz Butrymowicz, for his significant contribution to the research project on prototype refrigeration systems. His vast knowledge and experience in the field of refrigeration have been invaluable.

My sincere thanks to my assistant supervisor from Marani, Dr Łukasz Antczak, for the helpfulness shown in solving current research problems and setting the direction of the work.

I would also like to thank all my colleagues at the Bialystok University of Technology who worked with me on the research project and dissertation. Our collective efforts, especially those of Prof. Jerzy Gagan and Prof. Kamil Śmierciew, who were most involved in the experimental and design work, have been instrumental in the success of our project.

I also thank all the MARANI co-workers involved in the research project. Each of you, whether through the preparation of tenders, the formal handling of the project, the manufacture of prototype refrigeration systems, the development of control systems, or their preparation for experimental testing, played a crucial role in our project's success. Your specific roles and contributions have been integral to our achievements.

This work was co-financed by the Ministry of Education and Science of Poland under grant no DWD/3/7/2019-RJO15/SDW/001-35/001-2019/20. The author thanks the Ministry and the Silesian University of Technology authorities for the opportunity to participate in the program.

The research project directly related to the dissertation topic was funded by the European Union as part of the implementation by MARANI Sp. z o.o. in cooperation with Bialystok University of Technology of project No. POIR.01.01.01-00-0301/18, entitled "Development of two prototypes of refrigeration systems using waste heat with a driving thermal power of 600 kW and 200 kW adapted to chilled water temperature and high-temperature cooling" under the Intelligent Development Operational Program 2014-2020, Priority Axis I: "Support for the conduct of R&D work by enterprises," Measure 1.1 "R&D projects of enterprises," Sub-measure 1.1.1 "Industrial research and development work carried out by enterprises."

I would also like to thank the Board of Directors and employees of TIMKEN Ltd. in Sosnowiec for the opportunity to carry out experimental measurements on the company's premises and for their substantive and logistical support.

Last but not least, I would like to thank most sincerely my relatives, especially my wife Magdalena and daughter Ula, for their love and support shown, great forbearance for accepting the extra hours I spend working, and my parents and the rest of my family, for the abutment shown, understanding and care of the child.

Preface

This dissertation was written in close connection with a research project conducted by MARANI in cooperation with Bialystok University of Technology under the direction of Prof. Dariusz Butrymowicz.

The project's aim was "Development of two prototypes of refrigeration systems using waste heat with a driving thermal power of 600 kW and 200 kW adapted to chilled water temperature and high-temperature cooling." The project's primary objective was to develop, build, and test an innovative technology for ejector cooling systems driven by waste heat from industrial processes. In addition, an essential feature of the developed technology was the use of a working medium that fully meets the restrictive legal requirements for so-called F-Gases. This constitutes a unique technology that allows the use of waste heat from industrial processes with temperatures below the range available for competitive absorption and adsorption technologies, i.e., motive heat temperatures below 85°C with the possibility to use motive heat sources of temperatures even below 70°C. The solutions have been developed to achieve both chilled water temperatures dedicated to the standard operating parameters of air-conditioning units or technological processes cooling systems. Configurations of prototype solutions were developed to fit the prototype systems operational requirements under industrial applications conditions. The numerical calculations of supersonic ejectors were performed, allowing the development of their geometry and thermal-fluid calculations of the entire prototype refrigeration systems. Experimental validation of model calculations under on-design and off-design conditions was carried out on a test stand with control of driving heat input and the refrigeration capacity. The research also covers principles of operation control of the developed prototype refrigeration units. As part of the research work, the constructed innovative systems have been experimentally validated under actual operating conditions, i.e., under conditions of waste heat recovered from the industrial-scale air compression systems.

Documentation of prototypes complying with the pressure equipment directive and allowing MARANI to grant the CE mark on its products was developed. Two patent applications have also been filed, i.e., a manifold of three R1233zd(E) ejectors working in parallel and a refrigeration system configuration with separation of heat exchangers taking waste heat to a generator and preheater, of which the author of this dissertation is a co-author.

The Ph. D. student's responsibilities as a project engineer in the completed research project included participation in the modeling of the supersonic ejectors, entire refrigeration systems configuration, selection of the systems components, supervising implementation work, making corrections, supervising the development of the control system, implementing the test rig in an industrial plant, conducting validation tests, and finalizing refrigeration systems based on current regulations.

The Ph. D. student, cooperating as part of the research team with the Bialystok University of Technology, is also a co-author of a scientific article entitled "Experimental assessment of the first industrial implementation of ejector refrigeration system operating with R1233zd(E) driven by ultra-low temperature heat source" [1], which was written as a summary of part of the project's research work. Some of the research work conclusions described in the article were used in the dissertation.

The results from the experimental work carried out within the framework of the research project were used directly for the main topic of the dissertation, which is the construction of a mathematical model for the selection of components for ejector refrigeration systems, and they were used to validate the model. Implementing the model for the selection of refrigeration systems components is essential for MARANI from the perspective of designing commercial refrigeration systems.

In part, the results of the dissertation on the mathematical model of the ejector are described in the article titled "Experimental validation of the theoretical ejector model in a low-grade waste heat refrigeration system using R1233zdE as a working fluid" [2], which is considered part of the Ph. D. dissertation and directly quoted in this document.

As it has been indicated in the title of one of the above-cited papers, to the best knowledge of the author, the two developed prototypes are thought to be the first industrial-scale ejector refrigeration systems operating with fluid other than steam. Therefore, the provided research results covered not only modeling and experimentation research activities but also the development of technical solutions for industrial-scale refrigeration systems driven by low-grade waste heat using environmentally safe working fluid. The validation tests carried out under industrial conditions confirmed the technical readiness level that allows the implementation of developed technology of the heat-driven ejector refrigeration systems.

Contents

Nomenclature

Abbreviations

CFD	Computational Fluid Dynamics	
COP	Coefficient Of Performance	
DAQ	Data Acquisition	
EJA	Ejector Analysis Mode	
EJD	Ejector Design Mode	
GWP	Global Warming Potential	
HFC	Hydrofluorocarbon	
HFO	Hydrofluoroolefin	
HXA	Heat Exchanger Analysis	
HXD	Heat Exchanger Design	
LMTD	Logarithmic Mean Temperature Difference	
MC	Measuring Campaign	
MER	Mass Entrainment Ratio	
OHTC	Overall Heat Transfer Coefficient,	$\mathrm{kW\,m^{-2}K^{-1}}$

Subscripts

a	heat exchanger section end
avg	average
b	heat exchanger section end
c	heat exchanger section end
ch	heat exchanger single channel
$cond$	condenser
d	heat exchanger section end
dif	diffuser
ej	ejector
eq	equivalent
f	fluid or frictional
g	gas
gen	generator
hyp	hypothetical
in	inlet
is	isentropic
l	liquid
lm	logarithmic mean

m	mean	
me	mechanical-electric	
$mhyp$	motive fluid flow in hypothetical throat cross-section	
mix	mixing section or mixing process	
mn	motive nozzle	
nom	nominal	
out	outlet	
pp	pinch point	
rec	recuperator	
ref	refrigerant	
sat	saturation	
$shyp$	secondary fluid flow in hypothetical throat cross-section	
sn	suction nozzle	
th	throat	
w	wall	
Superscripts		
$cold$	cold fluid in the heat exchanger	
cw	cold water	
gl	glycol-water solution	
hot	hot fluid in the heat exchanger	
hw	hot water	
r	refrigerant	
Roman Symbols		
$\dot{G}$	mass flux density	kg $\mathrm{m}^2 s^1$
$\dot{m}$	mass flow rate	kg s^{-1}
$\dot{Q}$	heat transfer rate	kW
$\dot{Q}_0$	refrigeration capacity	kW
$\dot{Q}_{gen}$	generator thermal capacity	kW
A	surface area	m^2
a	speed of sound	m s^{-1}
A_t	effective heat transfer area of a single plate	m^2
b	spacing between heat exchanger plates	m
d	diameter	m
D_h	hydraulic diameter	m
D_p	port diameter of the heat exchanger	m
f	friction factor coefficient	-
f_m	friction factor	-
h	specific enthalpy	kJ kg^{-1}
k_{mix}	ejector mixing chamber length/diameter ratio	-
k_w	thermal conductivity of the wall	W m^{-1} K−1
l	length	m
L_h	horizontal distance between orifices	m

L_p	heat exchanger plate length	m
L_v	vertical distance between orifices	m
N_p	number of channels per pass	-
N_t	number of plates	-
N_{cp}	number of one-pass channels	-
P	electric power demand	kW
p	absolute pressure	bar
p_{ratio}	ejector pressure ratio	-
q	wet vapor quality	-
R_f	fouling factor	$m^2\,K\,W^{-1}$
s	specific entropy	$kJ\,kg^{-1}K^{-1}$
t	temperature	°C
w	velocity	$m\,s^{-1}$
W_p	heat exchanger plate width	m
Ma	Mach number	-
Nu	Nusselt number	-
Pr	Prandtl number	-
Re	Reynolds number	-
Greek Symbols		
α	convective heat transfer coefficient	$W\,m^{-2}\,K^{-1}$
β	chevron angle of the heat exchanger plate	deg
Δ	difference or pressure drop	-
δ	wall width or relative error	m or -
η	efficiency	-
γ	diverging angle	rad
κ	isentropic expansion coefficient	-
λ	thermal conductivity of the fluid	$W\,m^{-1}\,K{-}1$
μ	dynamic viscosity	Pa s
ϕ	surface enlargement factor	-
ρ	density	$kg\,m^{-3}$

Chapter 1

Introduction

1.1 Background

In the manufacturing industry, a large part of the energy supplied for the process is converted into waste heat, which reduces production efficiency and increases power consumption and costs. According to Kosmadakis [3], the waste heat potential in European Union (EU) countries was at the level of 221 TWh/year in 2021, while even 3100 TWh/year may be available to recover globally [4]. According to Forman et al. [5], the waste heat sources may be divided into high-grade of temperature above 300°C, medium-grade of temperature from 100°C to 299°C and finally low-grade of temperature below 100°C, which can account for up to 40% of waste heat in the industrial sector. The utilization of this type of heat source leads to significant savings in the form of reducing the consumption of primary fuel or electricity, reducing emissions of harmful compounds into the atmosphere, or leading to the production of an additional heat carrier such as hot water [6].

There are many areas where waste heat is in low-temperature form. According to Soda et al. [7], up to 60% of thermal energy is wasted as low or ultra-low quality through exhaust systems. Hung et al. [8] also similarly pointed out that low-temperature waste heat indicates about 50% of all heat generated in the industry. In the EU, potential applications of this waste heat are seen mainly in the food industry, where it accounts for 1.25 TWh/year [9]. In Europe, noticeable potential in low-temperature waste heat also exists in the mining or paper industries [10]. It occurs in various forms, for example, condensate from steam heating, cooling water from cooling systems, blast furnace gas from steelmaking processes, steam from evaporation and distillation in the food industry, dyed wastewater from drying in the textile industry, etc.[11]. Also, the share of waste heat from data centers is increasing significantly in the global low-temperature waste energy mix. [12].

A process that generates large amounts of low-temperature waste heat is air compression, during which, according to the compressors producers [13], [14], almost all of the electrical energy supplied to the compressor is converted into heat, about 70% of which is the heat received by the compressor oil cooling system. Because the production of compressed air demands 3% of the total electricity consumption in

Europe [15] and even 15% to 20% of global industry electricity consumption [16], the usage of waste heat from that process is an essential way to save energy. On the other hand, due to its low-temperature parameters, its possible application is very limited. Depending on the needs, it can be used both passively to produce hot water or heating and actively to produce heat with higher parameters, electricity, or cooling capacity [17]. An interesting idea is the creation of networks for industrial waste heat, which allows its maximum utilization [18], but this is not always possible due to the location and operation features of industrial plants.

Various technologies are being developed to produce electricity from waste heat, such as Organic Rankin Cycle (ORC) systems [19], thermoelectric power generation systems [20] or the combination of two of them [21]. Other technologies allow waste heat to generate electricity, such as pyroelectric, thermomagnetic, or thermogalvanic generators [22]. ORC systems increase their efficiency as the temperature of the waste heat used increases [23]. However, they already show around 5% efficiency for ultra-low temperature sources below 85°C [24]. Given that a "free" energy source such as waste heat is being considered, obtaining additional electricity despite relatively low efficiency is worth economic consideration.

Low-temperature waste heat can also be upgraded to high temperature using so-called high-temperature heat pumps, achieving a COP of around 5 [25]. They have numerous industrial applications, such as drying, thermal separation, and preservation, particularly in the food, paper, chemical, metal, and plastic manufacturing sectors [26].

Many industrial plants with waste heat at their disposal have a significant demand for cooling capacity. For example, in forges, cooling capacity is required for cooling hydraulic oil and bearing plants for hardening furnaces. Coal mines require cooling capacity for ventilation air, while steel mills need it for the operators rooms cooling. In virtually all plants, cooling capacity can be used to air conditioning of production halls or office spaces [27]. In such cases, refrigeration systems driven by waste heat may be cost-effective. One can distinguish absorption and adsorption refrigeration and ejector systems among such solutions.

Zhai et al. [28] presented the absorption refrigeration systems driven by the waste heat of around 80°C, achieving the COP of 0.5 - 0.8, depending on the cooling chilled water temperature. Many papers in the literature show this technology development through various configurations and the use of multiple mixtures of working fluids [29]–[31]. Such systems are also commercially available. Unfortunately, due to the required concentration difference in the working fluid mixture, there is a minimum motive heat temperature necessary for the relevant operation of these systems. In general, the above temperature significantly exceeds 80°C. It may be considered the main limitation of the practical application of the robust technology of the absorption refrigeration systems in the utilization of available low-grade waste heat under industrial applications [32]. These disadvantages are not possessed by refrigeration systems based on an ejector.

In particular, ejector-based refrigeration systems are considered a promising application for generating cooling capacity from low-temperature waste heat, as well as delivering promising performance [33]. Among the most significant advantages are reliability, low maintenance requirements, and low investment and operating costs [34].

1.2 Literature review

1.2.1 Concept of ejector-based refrigeration system

The well-known concept of a waste heat-driven ejector-supported cooling system has been developed since the 20th century, as documented in the literature [35]. A layout of the most straightforward ejector cooling cycle driven by waste heat is shown in Fig. 1.1. In this device, the ejector plays a role similar to the compressor in conventional refrigeration cycles, implementing the Linde cycle [36].

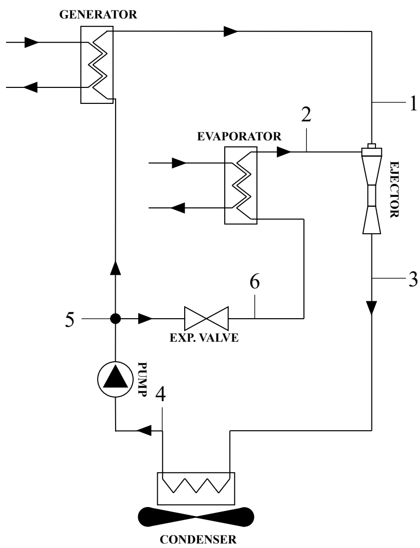

FIGURE 1.1: Simplified ejector refrigeration cycle

The process begins with the recovery of waste heat in the generator, where high-pressure vapor of the working fluid is produced (1). This vapor then flows to the ejector motive nozzle, where it expands, reaching supersonic speed. Due to the pressure difference and the momentum transfer between motive and secondary fluids, the low-pressure working fluid is entrained into the ejector suction nozzle (2). Due to the mixing of two streams and momentum transfer, the mixed streams absolute pressure is then increased to condensation (medium) pressure within the ejector diffuser (3). Following this, the working fluid is directed to the condenser, where it releases heat to the surroundings during the condensation process. The circulation pump pressurizes the subcooled liquid working fluid back to high pressure in the vapor generator (4-5). At this stage, the working fluid is split. A part returns to the generator while the rest is throttled through an expansion valve to reach the evaporation pressure (6). In the evaporator, the working fluid absorbs heat from the chilled water, which corresponds to the system refrigeration capacity. Finally, the evaporated working fluid is redirected to the ejector suction nozzle, completing the cycle.

The crucial component of the system is a supersonic ejector that acts as a compressor from a conventional refrigeration system and is used to raise the refrigerant pressure from evaporating to condensation pressure. Its proper design determines the performance of the entire refrigeration system.

The ejector is a simple flow device that raises the pressure of the entrained fluid. The simplified geometry of the ejector, including the pressure distribution along the flow direction, is shown in Fig. 1.2. It consists of a convergent-divergent motive nozzle, a suction chamber, a mixing chamber, and a divergent diffuser [37]. Due to the momentum transfer resulting from the significant difference in velocity between the motive stream (primary flow) and the entrained stream (secondary flow), the entrained stream is expanded and accelerated, and the motive stream is decelerated. As a result of the transition from supersonic to subsonic flow in the mixing chamber, a shock wave phenomenon is created, in which there is an increase in static pressure and a decrease in velocity, which is continued in the diffuser due to the increase in cross-sectional area [36].

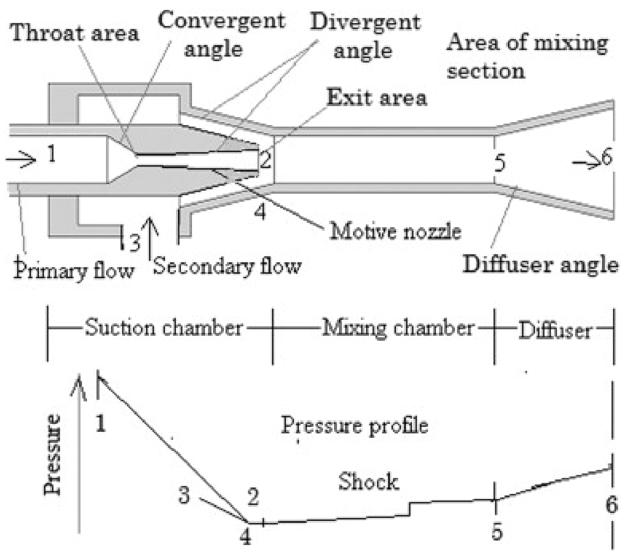

FIGURE 1.2: Simplified ejector geometry and pressure distribution along the axis [37]

The most important parameter determining the operation of an ejector is the Mass Entrainment Ratio (MER), which determines the suction flow to the motive flow ratio. The main operating characteristic of an ejector is defined as the relationship between MER and discharge pressure. The operating characteristic of an ejector-based refrigeration system is shown in Fig. 1.3. Under certain condensation pressure conditions, the ejector operates under double-choked mode, where both the primary and secondary streams reach the speed of sound. In this mode, the ejector reaches a maximum and constant MER value. This area of operation is called the critical mode or on-design operation mode, where the desired operation of an ejector occurs. This regime is mainly considered in ejector design and to which the other devices of the ejector-based system are adjusted. After exceeding a certain pressure value called the critical pressure (p_c), the critical flow of the entrained fluid flow disappears. In this mode, as the pressure increases, the entrained fluid flow through the ejector decreases, and only the motive flow reaches the speed of sound (single choking). This mode is called the subcritical or off-design operation mode. As the pressure rises to the limiting pressure p_l, the ejector stops working, and backflows occur [38].

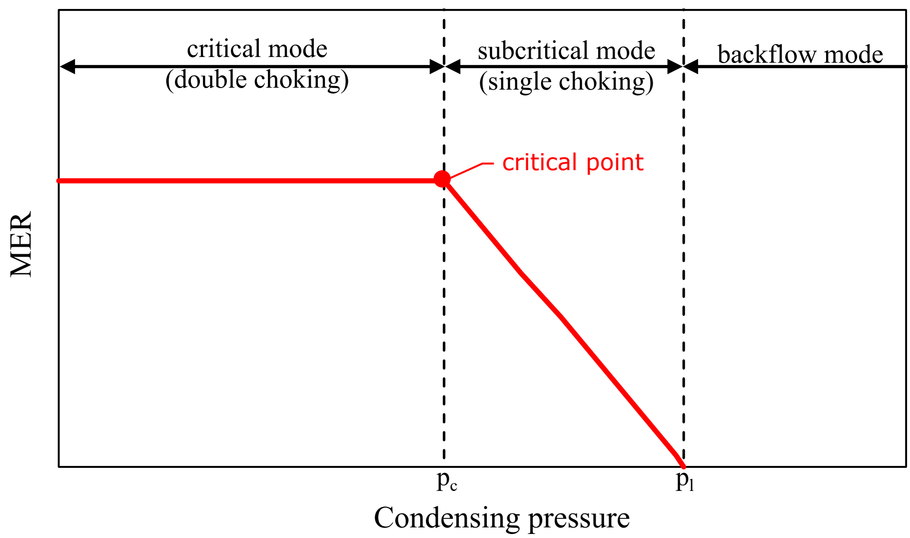

FIGURE 1.3: Operation modes of the ejector [38]

1.2.2 Configurations of ejector-based refrigerations systems

The concept of an ejector-based refrigeration system driven by waste heat is widely presented in the literature, where mathematical models and experimental tests were shown for several configurations and applications and many refrigerants as working fluids. Eames et al. [39] presented an ejector-based refrigeration system in standard configuration, while the modified version with a regenerator and precooler was indicated by Huang et al. [40]. Smierciew et al. [41] showed the experimental results for a solar-driven ejector air-conditioning system using isobutane as a refrigerant. The authors confirmed a maximal COP of 0.19 and cooling capacity of 1.75 kW for a generator saturation temperature of 55°C, an evaporation temperature of 7°C, and a condensation temperature below 25°C. Several works have also been developed on supersonic flow cooling systems driven by the heat of solar collectors, where the cross-section of the motive nozzle is adjusted using a sliding needle, providing the possibility to control the efficiency of the cooling system operation for a variable range of driving heat flux [42], [43]. A modification to the multi-ejector system was proposed by Beyrami and Hakkaki-Fard et al. [44] to increase the device operating flexibility to varying operating conditions using the example of a system running with R134a as a working fluid. They maximized the value of seasonal COP to 0.322 compared to a seasonal COP of 0.182 for a single ejector unit. The concept of an ejector-based refrigeration system without a refrigerant pump, using the second ejector to lift the refrigerant to high pressure in the cycle, appeared in the work of Shen et al. [45]. They presented a calculation for several refrigerants reaching a maximal COP of 0.26 for ammonia at saturation temperatures in a generator, condenser, and evaporator of 80°C, 35°C, and 8°C, respectively. Also, two-stage ejector-based refrigeration systems are considered in the literature. Jaruwongwittaya and Chen [46] showed a two-stage ejector air-conditioning system driven by heat from bus engine exhaust gas and with water as the working fluid. They calculated the system performance for an evaporation temperature of 5°C and condensation temperature of 54°C, reaching a COP of 0.29 for the assumed temperature of 100°C in the generator. Anan et al. [47] considered a double-stage with ejectors connected in series showing good performance in high condenser temperatures above 50°C. Combined systems are also available in the literature. Ersayın et al. [48] presented a combined geothermal-ejector-based refrigeration system utilizing waste heat of 82°C and 70°C, using four refrigerants R290, R717, R600 and R1234ze. Incorporating the ejector refrigeration cycle led to a 12% boost in overall energy efficiency compared to conventional power-only systems, achieving a peak COP of 0.72 under ideal conditions. Parvez et al. [49] introduced a design that combines the Rankine cycle with an ejector and absorption refrigeration cycle, using the low-temperature energy from the steam turbine's exit to generate both power and cooling at the same time. Shestopalov et al. [50] presented the concept of a hybrid ejector-compression cooling system for storage areas on cargo ships. Other similar devices may be indicated in the literature; however, they have never been used commercially [34]. With the rising price of electricity and the need to meet environmental requirements, heat utilization to drive such systems is becoming increasingly attractive to entrepreneurs.

1.2.3 Working fluids for ejector-based refrigeration systems

As a result of the Kigali Amendment to the Montreal Protocol [51] and previous international agreements, the HFC refrigerants, despite being a suitable working fluid for low-grade waste heat ejector refrigeration equipment, as confirmed experimentally in [52], [53], are being phased out. Consequently, the potential refrigerants for application in ejector-based refrigeration systems have been severely limited. Recent research on refrigeration ejector cycles has focused on the selection of appropriate working fluids that meet stringent regulatory requirements and ensure optimal system performance. The industry is forced to use natural refrigerants. Despite attempts at the experimental application of natural refrigerants such as ammonia [54] or isobutane [55] in ejector-based refrigeration systems driven by low-temperature waste heat below 80°C, the use of these refrigerants commercially is troublesome due to the chemical reactivity and toxicity of ammonia and the flammability of hydrocarbons. Al-Sayyab et al. [56] considered R450A and R513A as potential substitutes for R134a. The findings indicated that the proposed system enhances the cooling COP by 7% when using R450A, compared to a traditional R134a vapor compression system. However, the 5% decrease in COP was obtained using R513A.

A new generation of synthetic refrigerants, such as HFO refrigerants, appears to be a good compromise, which was confirmed in the literature. Fang et al. [57] presented a numerical analysis of the replacement of R134a with HFO refrigerants such as R1234yf and R1234ze(E) in ejector-based refrigeration systems driven by waste-heat, finding comparable performance with similar motive nozzle parameters and pressure ratios. Smierciew et al. [58] showed experimental results for an ejector-based refrigeration system operating with R1234ze(E) as the working fluid. A COP of up to 0.45 was obtained for critical operation with low-temperature waste heat supply conditions. In their theoretical assessment, Suresh and Datta [59] evaluated refrigerants R152a, R440a, R1234yf, R1243zf, R1234ze(E), and R513a in a hybrid ejector-compressor refrigeration cycle. The proposed system was designed for mobile air conditioning. The results indicated that in hybrid mode, R1234yf achieved the highest entrainment ratio and COP, whereas in ejector mode, R152a provided the maximum COP. Rostamnejad Takleh and Zare [60] provided a theoretical work concerning two-phase ejector using different fluids: R134a, R236fa, R227ea, R500, R1234yf, R1234ze(E), indicating the best performance improvement for R1234ze(E). Atmaca et al. [61] performed a similar mathematical study that compared R1234yf and R1234ze(E) refrigerants for the ejector expansion refrigeration cycle. Mateu-Royo et al. [62] presented theoretical studies on the performance of a high-temperature heat pump equipped with an ejector using R245fa, R600, R601, R514a, R1336mzz(Z), R1233zd(E), and R1224yd(Z) as refrigerant, employing a two-phase ejector in their studies. A comparative experimental study was also conducted by Iskan and Direk [63], who tested the dual-evaporator ejector-based refrigeration system using environmentally friendly refrigerants of R1234ze(E), ND, R515a, R456a, and R516a. Other similar works were performed by Wang et al. [64], who mathematically verified the compatibility of HFO refrigerants for a hybrid refrigeration system driven by heat from solar panels, showing the highest COP for R1234ze(Z). Within the HFO refrigerants, R1336mzz(Z) had the most significant COP improvement compared to R245fa, which was used as a reference. Unal et al. [65] compared R1234yf, R1234ze(E), and R600a as a potential substitute for R134a to use in two-phase ejectors for bus air-conditioning systems. The authors mathematically compared the refrigerants due to the crucial size of the ejector in the application under study. Applications of HFO refrigerants have been summarized by Nair [66] indicating theoretical or bench work, mainly in small applications, e.g., replacing phased-out refrigerants in domestic refrigerators.

Among the HFO refrigerants, the new refrigerant R1233zd(E) can be distinguished, having the A1 safety category according to ASHRAE 34 Standard, indicating its non-flammability and non-toxicity. Moreover, under the conditions corresponding to refrigeration cycles driven by low-grade heat sources, it can be classified as a low-pressure fluid. The above characteristics are advantageous when introducing refrigeration systems to the market, as they eliminate the need for special safety measures or special strength requirements for the materials used. This might be especially important when dealing with large-scale refrigeration systems with substantial refrigerant volumes. The refrigerant R1233zd(E) was tested experimentally by Mahmoudian et al. [67], achieving a COP of 0.4 under critical conditions at an evaporating temperature of 10°C while maintaining a generator saturation temperature of 97°C during testing. The above work is the only one found where the refrigeration system was studied with the above refrigerant. Still, the system operating conditions corresponded to a medium-temperature waste heat supply above 100°C. Works treating experimental studies of ejector-based refrigeration systems using the working fluid R1233zd(E) driven by low-temperature waste heat are unavailable in the literature.

1.2.4 Ejector mathematical models

Commercially available components such as heat exchangers or a pump are required for this ejector refrigeration installation, and the ejector must be designed individually at this stage. The crucial consideration in developing this component is appropriately evaluating the geometry and estimating the critical performance factors to match the system parameters. Simultaneously, a fast-running model is required for optimization processes. For this purpose, many examples of so-called zero and one-dimensional (0-D/1-D) models that allow the evaluation of the operation of a gas ejector under on-design and off-design operation modes can be found in the literature. Huang et al. [68] presented a 1-D model for the ejector performance prediction at critical conditions, assuming the ideal gas properties. A relative error below 10% of MER estimation was obtained for the R141b ejector. Zhu et al. [69] presented a vapor ejector model with ideal gas properties by introducing the suction fluid flow close to the inner walls of the ejector mixing chamber in 2-D form and a shock circle representing the choking condition of ejector critical mode operation. The model was more accurate in estimating MER than the 1-D mentioned above, using only two assumed coefficients. Khalil et al. [70] developed a mathematical model to design an R134a ejector considering friction losses in the mixing chamber. Kumar and Ooi [71] presented the 1-D model of a gas ejector operated under critical conditions by assuming Fanno flow in the mixing chamber and improving the model accuracy in comparison with results obtained by Huang et al. [68], and the absolute relative error in MER estimation was below 4%. Shi et al. [72], [73] proposed a 1-D model using real gas properties and calculating the ejector performance in critical and subcritical conditions. Implementing the real-gas properties provided higher accuracy than ideal-gas properties, especially in the subcritical region. Saleh [74] also developed a mathematical model based on previous literature to find the potential working fluids for ejector-based refrigeration systems. Kumar and Sachdeva [75] introduced into their mathematical model the concepts of Prandtl mixing length, Prandtl–Meyer expansion wave, Kelvin–Helmholtz instability, and Baroclinic effect, reaching a relative error in MER estimation at an average level of 2.5%. Guo et al. [76] presented the theoretical model of ejectors based on the foundation of compound-choking theory and gas dynamic relations, which predicts the ejector performance under the on-design and off-design conditions. The authors validated the model using experimental data from R245fa, R134a, and R600a ejector-based refrigeration systems published in the literature. They achieved the mean relative errors of 2.45%, 5.49%, and 3.67% in estimating the critical pressure for the above refrigerants. A different approach was considered by Zhu et al. [77], [78]. The authors combined the ideal gas model of the ejector with an adaptive error compensation algorithm based on neural networks to improve critical pressure prediction accuracy. The authors also used the data from the literature to validate their model. Van den Berghe et al. [79] presented a 1-D transient model combining 1-D unsteady Euler equations with a junction model. The model was calibrated using the CFD results. An ejector mathematical model was built to calculate the ejector performance for R1233zd(E) refrigerant by Mwesigye and Dworkin [80]. The authors proposed the correlations for ejector loss coefficients based on an ejector model validated by experimental results for R141b and R245fa refrigerants.

Many other 0-D and 1-D models were described in the literature; however, they were mainly validated by experimental results of vapor ejectors using HFC refrigerants that are in the phase-out process as shown in [68] for R141b, in [81] for R11, and [52] for R134a. Low GWP-validated 0-D models are missing from the literature.

1.3 Motivation and objectives

A literature review shows a lack of well-described system models of ejector-based refrigeration systems covering all components and allowing the selection of each element separately. Research publications primarily focus on modeling the supersonic ejector, presenting many 0-D and 1-D models describing single-phase ejectors. They are dominated by models validated based on experiments performed on phased-out refrigerants, mainly from the HFC group. They do not consider low-pressure refrigerants under low-temperature waste heat recovery conditions. Moreover, much of the work on ejector-based refrigeration systems for new, environmentally friendly refrigerant groups includes work carried out for waste heat supply conditions with temperatures higher than 100°C. These include a small number of cases of experimental work on laboratory benches and a lot of theoretical work based on models calibrated for old refrigerants. There is currently a lack of commercial ejector-based refrigeration systems driven by low-grade waste heat worldwide, and thus, there is no testing under real-load operating conditions. All of the developed theoretical models of supersonic ejectors require a set of the efficiencies of the ejector components that are based on the experimental data. Although these component efficiencies have been well developed for the conventional working fluids, there is still a gap of knowledge concerning available levels of the above efficiencies for the new perspective generation of working fluids. The above may be considered as additional motivation for the experimental tests.

Based on the presented in the previous section state of the art the following innovations and novelties have been identified, which will be the basis of the present thesis:

- development of the first ejector refrigeration systems driven by the low-grade waste heat of temperatures 85°C and below, at full industrial scale,
- application of new generation of working fluids operated with low-grade motive heat,
- development of a comprehensive design procedure for the entire ejector refrigeration system that will be validated under full industrial scale,
- the need to recognize supersonic ejector components efficiencies for the new working fluid generation.

For this reason, this work aimed to develop a fast-running model for the selection of the components for the ejector-based refrigeration system along with experimental validation for the first prototypes of the ejector-based refrigeration system from MARANI Ltd. operating with low GWP HFO and non-flammable refrigerants R1233zd(E) and R1234ze(E) driven by ultra-low-grade waste heat. In particular, the following partial goals have been formulated:

- formulation of mathematical model for components selection of ejector refrigeration cycle driven by low-grade waste heat with ejector 0-D fast-running model,
- conducting tests of the first two prototypes of ejector-based refrigeration systems driven by the waste-heat of the motive thermal capacity of 200 kW and 600 kW under real industrial conditions using new environmentally friendly and low-pressure HFO refrigerants,
- validation and calibration of the ejector refrigeration cycle components models based on the results of the experiment,
- experimental comparison of two types of refrigerants, R1233zd(E) and R1234ze(E), for use in refrigeration equipment for conventional chilled water temperatures and increased chilled water temperatures dedicated for high-temperature air conditioning systems.

1.4 Scope

The thesis consists of the following chapters:

Chapter 1 is this chapter.

Chapter 2 describes the two prototype ejector-based refrigeration systems developed for this research, one with a 200 kW capacity and the other with a 600 kW capacity. It details the design considerations, specific components of the systems, and the challenges encountered during construction and testing.

Chapter 3 presents the experimental setup and methodology for testing the two prototype systems. It discusses the measurement system, the experimental procedures, and the modifications made to the systems and test rigs during the measurement campaigns.

Chapter 4 presents the development of a comprehensive mathematical model for the ejector-based refrigeration system, focusing on individual components such as the ejector, heat exchangers (generator, preheater, evaporator, condenser, and recuperator), expansion valve, and pump. The chapter explains the assumptions, equations, and algorithms for modeling each component, highlighting the importance of accurate parameter estimation for reliable model predictions.

Chapter 5 analyzes the experimental results obtained from testing the two prototype systems, focusing on validating the mathematical model and evaluating the performance of the ejector-based refrigeration system under different operating conditions. It also compares the performance of the R1233zd(E) and R1234ze(E) refrigerants, considering their thermodynamic efficiency and utilization possibility for specified cooling parameters.

Chapter 6 summarizes the essential findings and conclusions of the research. It highlights the importance of utilizing low-grade waste heat for sustainable cooling, the potential of ejector-based refrigeration systems, the challenges and limitations of the research, and the future directions for continued development and commercialization of this technology.

Chapter 2

Problem description

The thesis objects were two innovative and first-time manufactured prototypes of ejector refrigeration systems driven by low-grade waste heat of 200 kW and 600 kW recovered from industrial processes, including air compression systems. Managing the significant amounts of heat generated by these systems poses a considerable technical challenge because it is overwhelmingly low-temperature heat at 85°C, or even below 70°C in exceptional cases. For reasons arising from the reduction in energy efficiency associated with converting this heat to electricity, a rational course of action is to manage this heat for technically and economically valuable purposes other than electricity production. CAD models of both systems are presented in Fig. 2.1.

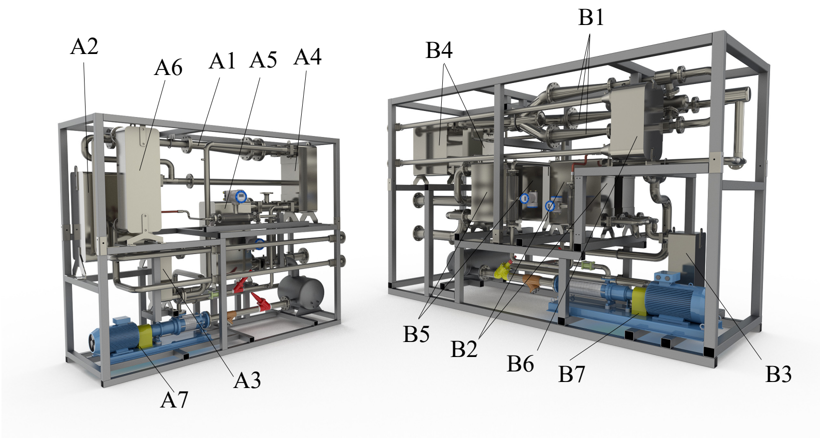

FIGURE 2.1: CAD models of ejector refrigeration system prototypes (on the left - MARANI CHILLER 200, on the right - MARANI CHILLER 600), where A1, B1 - ejectors, A2, B2 - generators, A3, B3 - preheaters, A4, B4 - recuperators, A5, B5 - condensers, A6, B6 - evaporators, A7, B7 - circulating pumps

The above systems represent innovative technology for convertion of low-grade heat into cooling capacity, which can be used for both process cooling and air conditioning of industrial facilities. They are designed to operate in two cooling modes.

In the conventional version, named for this paper, standard parameters, where it is required to obtain a chilled water temperature of 6°C enable their application for air-conditioning units. For the new solutions in air-conditioning of premises, including industrial premises, they can operate in high-temperature cooling, requiring a temperature of 16°C. Due to the low temperatures of waste heat, it is impossible to use known technologies of sorption systems. One of the youngest refrigeration system technologies, i.e., ejector systems, has been developed, tested, and implemented for the first time.

The research assumptions indicated that the prototype 200 kW refrigeration system should operate under nominal conditions, driven by waste heat with a temperature not higher than 85°C, and producing cooling capacity with nominal parameters required by commercially available air-conditioning systems, i.e., chilled water at a temperature of 6°C (return from the chilled water receiver 12°C). The project goal was to develop a system solution that would enable its operation for a new approach to technological cooling, utilizing a cold fluid temperature of 16°C on the inlet and 19°C on the return from the cooling receiver. The MARANI CHILLER 600 prototype was assumed to operate driven by waste heat with a temperature not higher than 85°C and producing cooling capacity with the parameters required by commercially available air conditioning systems, i.e., chilled water at a temperature of 6°C (return from the chilled water receiver 12°C). It was also planned to develop a solution for this system in such a way as to enable its operation for waste heat from industrial sources at a temperature level of 150°C.

Simplified technological schemes of the prototype refrigeration systems were presented in Fig. 2.2 and 2.3. The refrigeration systems consisted of a refrigerant cycle (1-9) and heat transfer loops, i.e., a hot water loop (hw1 - hw3) for transportation of waste heat to drive the refrigeration system, a glycol-in-water solution loop (gl1 - gl2) for transportation of cooling capacity, and a condenser cooling water loop (cw1 - cw2). The prototype refrigeration systems consisted of plate heat exchangers, i.e., a generator (A2 or B2) and preheater (A3 or B3) to receive waste heat, an evaporator (A6 or B6) to receive heat from the cooled fluid, a condenser (A5 or B5) to transfer heat to the surroundings, and a recuperator (A4 or B4) to recover part of the discharged vapor superheating to preheat the liquid refrigerant. In the 600 kW system, it was necessary to duplicate the generators, recuperators, and condensers to achieve the required thermal capacities. The plate heat exchangers had flanged connections to quickly replace individual components during refrigeration system tests. The technical data of used heat exchangers is shown in Table 2.1.

In addition, the refrigeration systems were equipped with side-channel refrigerant circulating pumps (A7 or B7) to pump the refrigerant to the generator. The special design of the pumps ensured low required NPSH (Net Positive Suction Head) values at the pump suction port, which means necessary pressure anti-cavitation surplus at the pump inlet. This made it possible to use the above pumps with low-pressure refrigerant without additional feed pumps or a significant increase in the liquid column

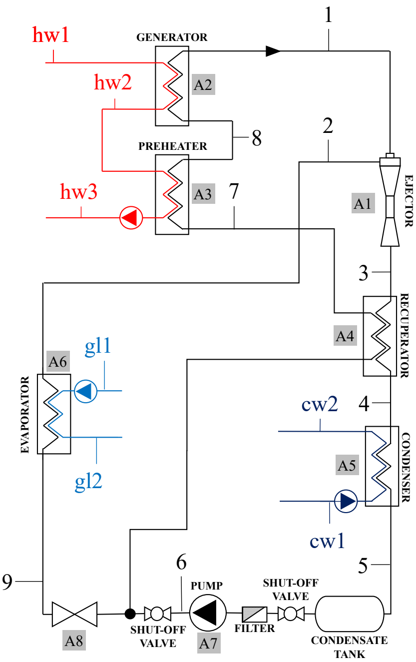

FIGURE 2.2: Layout of ejector refrigeration unit driven by waste heat of 200 kW - MARANI CHILLER 200, where A1 - ejector, A2 - generator, A3 - preheater, A4 - recuperator, A5 - condenser, A6 - evaporator, A7 - circulating pump, A8 - expansion valve, hw - hot water, cw - cold water, gl - glycol-water solution

height in front of the pump. Additional fittings were used to protect the pumps and provide access during tests, like a filter protecting the pumps before the suction port and two shut-off valves to cut-off the pump from the rest of the refrigeration system. The technical parameters of the circulating pumps were presented in Table 2.2. The operating capacity of individual pumps was adjusted using frequency inverters Mitsubishi Electric FR-F840 in the range of 0 Hz to 50 Hz.

The systems featured electronic expansion valves Danfoss ETS 24C (A8) and Danfoss ETS 100C (B8) to achieve evaporator saturation pressure. The Danfoss EKE-1C superheat controller controlled the expansion valve, allowing for percentage adjustment of its opening degree to maintain the required superheat of steam at the suction inlet of the ejector.

The key components of the refrigeration systems were supersonic ejectors made by MARANI Ltd. A system of three parallel ejectors presented in Fig. 2.4 was required for the 600 kW system to achieve the required parameters. The ejectors were made of separate components such as a suction chamber, mixing chamber, and diffuser, which were terminated with flanges, which allowed for any combination of components during testing. In addition, the motive nozzle of the ejector was screwed into the

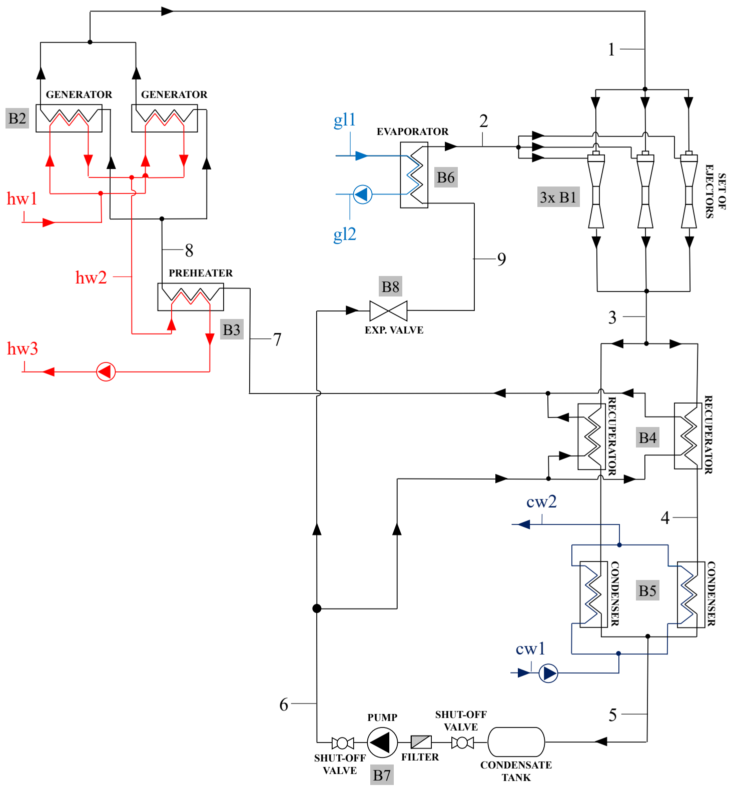

FIGURE 2.3: Layout of ejector refrigeration unit driven by waste heat of 600 kW - MARANI CHILLER 600, where 3xB1 - set of ejectors, B2 - generators, B3 - preheater, B4 - recuperators, B5 - condensers, B6 - evaporator, B7 - circulating pump, B8 - expansion valve, hw - hot water, cw - cold water, gl - glycol-water solution

suction chamber of the ejector using spacer rings that allowed the end of the drive nozzle to be moved closer and further away from the inlet of the mixing chamber. Three ejector geometries were designed to meet the parameters of the milestones declared in the research project. The most important dimensions of the used ejectors are shown in Table. 2.3.

Prototype refrigeration systems were manufactured by MARANI Ltd. for testing under industrial conditions. The components of the refrigeration systems were placed on steel frames to allow the transport of both refrigeration systems. The prototypes were equipped with bleeder valves to enable the systems to be filled and emptied of refrigerant. The piping and heat exchangers were thermally insulated. Leakage tests with compressed air, nitrogen, and refrigerant were carried out at various project stages. Leakage tests were also performed on the low vacuum before filling the systems. For the pneumatic tests, systems were filled with compressed air at up to 7 bar(a) and tested for leaks for 24 hours. Tightness was also tested visually using a special foam. In the case

TABLE 2.1: Heat exchangers parameters in both ejector refrigeration prototypes

Heat exchanger	Prototype	Manufacturer	Model	Nominal heat load	Surface area
Preheater A3	200 kW	KELVION	GBS 700L-50	40 kW	6.48 m^2
Generator A2		KELVION	GBS 1000H-260	160 kW	77.40 m^2
Recuperator A4		KELVION	GBS 1000M-120	15 kW	35.40 m^2
Evaporator A6		SWEP	B500TMx92	45 kW	26.90 m^2
Condenser A5		KELVION	GBS 1000H-190	235 kW	56.40 m^2
Preheater B3	600 kW	KELVION	GBS 1000M-120	100 kW	35.40 m^2
Generator B2		KELVION	2 x GBS 1000H-310	500 kW	184.80 m^2
Recuperator B4		KELVION	2 x GBS 1000H-330	40 kW	196.80 m^2
Evaporator B6		SWEP	B633Mx140	125 kW	57.20 m^2
Condenser B5		KELVION	2 x GBS 1000L-260	700 kW	154.80 m^2

TABLE 2.2: Pumps parameters in both ejector refrigeration prototypes

Symbol	Prototype	Model	Electric power	Flow rate	Pressure dif.	NPSH
A7	200 kW	SERO SEMA-S 333	5.5 kW	4.3 m^3/h	9.6 bar	0.52 m
B7	600 kW	SERO SEMA-S 556	30 kW	12.6 m^3/h	23.6 bar	0.43 m

TABLE 2.3: Ejector dimensions

Ejector set	Diameter of:			Length of:	
	Motive nozzle throat	Mixer	Diffuser outlet	Mixer	Diffuser
I	27.9 mm	59.5 mm	178 mm	601 mm	832 mm
II	27.9 mm	52.3 mm	157 mm	543 mm	744 mm
III	29.7 mm	52.3 mm	157 mm	543 mm	744 mm

of the MARANI CHILLER 600 refrigeration system, which was filled with high-pressure refrigerant R1234zd(E) in the final tests, leaks were previously tested using nitrogen at a pressure of about 20 bar(a). The vacuum tests resulted in a low vacuum of less than 270 Pa(a); however, refrigeration systems achieved a vacuum as low as 150 Pa(a). The low vacuum was maintained until the system was filled with refrigerant, which took from several hours to a day. The tightness of the systems was also monitored several times after they were filled with refrigerant using dedicated detectors.

Detailed information on the measurement systems of the refrigeration systems in question is presented in Chapter 3.

FIGURE 2.4: Set of ejectors in MARANI CHILLER 600 prototype

Chapter 3

Test rigs and experiments

3.1 Measurement system

The prototype refrigeration systems were prepared to conduct experimental tests. The MARANI CHILLER 200 was implemented at the MARANI compressor plant in operation at the bearing factory TIMKEN Ltd. in Sosnowiec, Poland, and powered by waste heat from the compressor oil system of 3 air compressors with an electric drive power of 200 kW each. Fig. 3.1 shows the installed industrial-scale test rig.

FIGURE 3.1: MARANI CHILLER 200 kW installed in the air compressor station

A schematic of the refrigeration system, including the measurement system and heat transfer fluids connections, is shown in Fig. 3.2. Waste heat from the air compression installation was transferred from the oil-cooling loop of the air compressors to the preheater and generator of the refrigeration system utilizing a hot water loop (hw1 - hw3), causing heating and evaporation of the high-pressure refrigerant (7-1), which was then the driving fluid of the ejector (1). The cooling water received the heat from the condenser (cw1 - cw2), causing the condensation of the refrigerant (4-5), and then dissipated into the surroundings in the cooling tower. An aqueous glycol solution loop was applied at the second side of the evaporator (gl1 - gl2). For testing purposes, the heat load was delivered by the electric heater with the controlled heating capacity connected to a chilled water buffer tank, which simulated the refrigeration capacity.

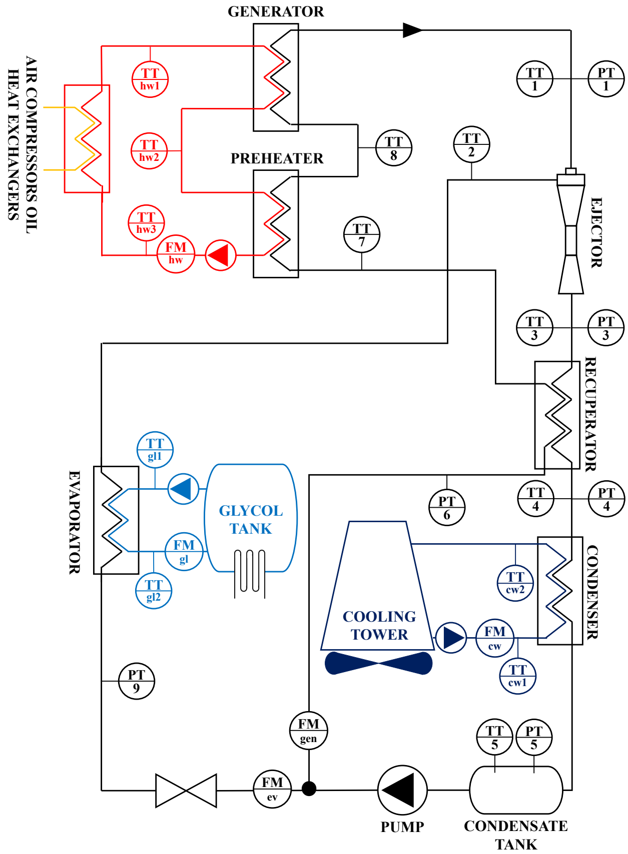

FIGURE 3.2: MARANI CHILLER 200 kW test rig installed in the air compressor station with the measurement instruments marked as follows: PT - pressure transmitter, TT - temperature transmitter, FM - flow meter, and fluids indexes as follows: hw - hot water, gl - glycol-water solution, cw - cold water.

Key parameters were measured to determine the entire system performance and evaluate the operation of individual components. The sensors were limited in some places to reduce refrigerant leakage from the system. The temperature of the refrigerant was measured at the ejector inlets (TT-1, TT-2) and outlet (TT-3), at the condenser inlet (TT-4), in the condensate tank (TT-5), before the preheater (TT-7) and at the generator inlet (TT-8), using the resistance temperature sensors PT100. Moreover, the absolute pressure of the refrigerant was read at characteristic points, i.e., ejector motive inlet (PT-1) and outlet (PT-3), condenser inlet (PT-4), in the condensate tank (PT-5), at the recuperator cold inlet (PT-6) and the evaporator inlet (PT-9), using piezoelectric pressure sensors. Also, the heat transportation loops were measured. The temperature of hot water was read at the generator inlet (TT-hw1), generator outlet (TT-hw2), and preheater outlet (TT-hw3). The temperature of the glycol-water solution was measured at the evaporator inlet (TT-gl1) and outlet (TT-gl2). Finally, the cold water temperature was measured at the condenser inlet (TT-cw1) and outlet (TT-cw2). The mass flow rates of the motive and secondary fluid flows were measured using Coriolis mass flow meters indicated in the refrigeration cycle layout as FM-gen and FM-ev. The flow values were measured in all heat transfer loops (hot water loop - FM-hw, glycol loop - FM-gl, and cold water loop - FM-cw) using electromagnetic volumetric flow meters to balance the heat exchangers. The list of measurement sensors applied in the system is shown in Tab. 3.1, along with the operating parameters and measurement accuracy. The measurement readings were transmitted by a 4...20 mA current signal to the National Instruments measurement DAQ system module, which allowed the measurement results to be recorded over time in database files and the system to be controlled using the LabView software. The sampling time was 1 s. All measuring instruments have been calibrated within the required measurement range.

TABLE 3.1: Measuring instruments

Symbol	**Quantity**	**Instrument**	**Sensor type**	**Accuracy**	**Range**
TT-1	t_1	Energosilesia TR1	PT100	Class A (max ±0.35°C)	-10...+150°C
TT-2	t_2	Energosilesia TR1	PT100	Class A (max ±0.35°C)	-10...+150°C
TT-3	t_3	Energosilesia TR1	PT100	Class A (max ±0.35°C)	-10...+150°C
TT-4	t_4	Energosilesia TR1	PT100	Class A (max ±0.35°C)	-10...+150°C
TT-5	t_5	Energosilesia TR1	PT100	Class A (max ±0.35°C)	-10...+150°C
TT-7	t_7	Energosilesia TR1	PT100	Class A (max ±0.35°C)	-10...+150°C
TT-8	t_8	Energosilesia TR1	PT100	Class A (max ±0.35°C)	-10...+150°C
TT-hw1	t_{hw1}	Energosilesia TR1	PT100	Class A (max ±0.35°C)	-10...+150°C
TT-hw2	t_{hw2}	Energosilesia TR1	PT100	Class A (max ±0.35°C)	-10...+150°C
TT-hw3	t_{hw3}	Energosilesia TR1	PT100	Class A (max ±0.35°C)	-10...+150°C
TT-gl1	t_{gl1}	Energosilesia TR1	PT100	Class A (max ±0.35°C)	-10...+150°C
TT-gl2	t_{gl2}	Energosilesia TR1	PT100	Class A (max ±0.35°C)	-10...+150°C
TT-cw1	t_{cw1}	Energosilesia TR1	PT100	Class A (max ±0.35°C)	-10...+150°C
TT-cw2	t_{cw2}	Energosilesia TR1	PT100	Class A (max ±0.35°C)	-10...+150°C
PT-1	p_1	WIKA S-20	Piezoresistance	±0.15% of the set span	0...25 bar
PT-3	p_3	WIKA S-20	Piezoresistance	±0.15% of the set span	0...25 bar
PT-4	p_4	WIKA S-20	Piezoresistance	±0.15% of the set span	0...25 bar
PT-5	p_5	WIKA S-20	Piezoresistance	±0.15% of the set span	0...25 bar
PT-6	p_6	WIKA S-20	Piezoresistance	±0.15% of the set span	0...25 bar
PT-9	p_9	WIKA S-20	Piezoresistance	±0.15% of the set span	0...16 bar
FM-gen	$\dot{m}_{gen}$	Krohne Optimass 1000-S25	Coriolis	max ±0.25% of read	0...1.8 kg/s
FM-ev	$\dot{m}_{evap}$	Krohne Optimass 1000-S15	Coriolis	max ±0.35% of read	0...0.6 kg/s
FM-hw	$\dot{m}_{hw}$	Krohne Optiflux 4300	Electromagnetic	max ±0.25% of read	0...20.0 l/s
FM-cw	$\dot{m}_{cw}$	Krohne Optiflux 2300	Electromagnetic	max ±0.25% of read	0...50.0 l/s
FM-gl	$\dot{m}_{gl}$	Krohne Optiflux 4300	Electromagnetic	max ±0.25% of read	0...12.5 l/s

The second refrigeration system tested was the MARANI CHILLER 600 prototype. Due to difficulties securing an industrial location for testing, the device was installed on a specially prepared test stand at the Bialystok University of Technology. The above test stand consisted of a containerized steam generator with available thermal power of 1.2 MW and a cooling tower with similar thermal capacity. The installation allowed infinitely variable power control from about 300 kW to the maximum power. It provided a maximum of 1,500 kg/h of steam with a quality of at least 0.97. The refrigeration system prototype installed in the test stand was presented in Fig. 3.3. To drive the prototype refrigeration system, the steam system was modified and equipped with a control valve to control the steam flow rate directed to the heat exchangers, simulating recovered waste heat transportation. In addition, a steam generator system was made to allow the artificial loading of the evaporator by an additional loop with a plate heat exchanger, where the steam flow rate was also controlled. To control the steam mass flow rates in the above-discussed loops, Schubert&Salzer electrically operated control valves were used, controlled by a 0-10 V voltage signal and allowing steam control in the range of 50 - 300 kg/h for the evaporator load and 120 - 900 kg/h for the simulation of the motive heat source.

FIGURE 3.3: MARANI CHILLER 600 kW installed in the test stand

A refrigeration system layout, including the measuring sensors, is shown in Fig. 3.4. The measurement sensors were arranged similarly to the MARANI CHILLER 200 kW. The temperature and pressure sensors correspond to the sensors shown in Table 3.1. Due to the mass flow rate measurement ranges in the refrigeration system and heat transfer loops, mass flow meters, and volumetric flow meters shown in Table 3.2 were used. Due to the change of the hot fluid feeding the heater and generator from hot water to steam, no electromagnetic flow meter was used in the hot loop.

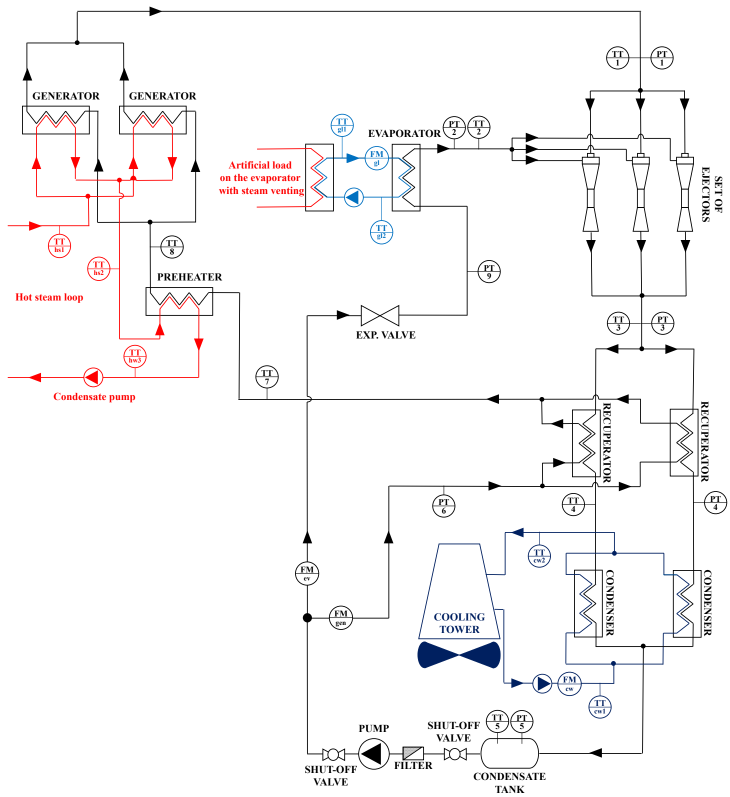

FIGURE 3.4: MARANI CHILLER 600 kW test rig installed in test rig in Bialystok University of Technology with the measurement instruments marked as follows: PT - pressure transmitter, TT - temperature transmitter, FM - flow meter, and fluids indexes as follows: hw - hot steam/water, gl - glycol-water solution, cw - cold water

3.2 Experimental tests

The experiment encompassed the start-up running of the prototype refrigeration systems, addressing and resolving early-stage issues, and performing comprehensive tests. These early-stage issues included installing sensors, sealing the installation, and eliminating refrigerant leaks. Multiple leakage tests were conducted under pressure and vacuum conditions to ensure system integrity. Additionally, the installation was filled with refrigerant, and the operation of pumps and inverters was thoroughly checked. The commissioning of the refrigeration systems was also a critical step.

These tests aimed to evaluate the system and the ejector performance under conditions that matched the design specifications (on-design) and those that deviated from them (off-design). Furthermore, the experiment provided valuable insights into the operational efficiency and potential areas for improvement, ensuring the system reliability and robustness in various scenarios. To achieve this goal, the performance

TABLE 3.2: Flow meters used for MARANI CHILLER 600 experimental tests

Symbol	Quantity	Instrument	Sensor type	Accuracy	Range
FM-gen	$\dot{m}_{gen}$	Krohne Optimass 1000-S25	Coriolis	max ±0.25% of read	0...5 kg/s
FM-ev	$\dot{m}_{evap}$	Krohne Optimass 1000-S25	Coriolis	max ±0.35% of read	0...2 kg/s
FM-gl	$\dot{m}_{gl}$	Krohne Optiflux 4300	Electromagnetic	max ±0.25% of read	0...20.0 l/s
FM-cw	$\dot{m}_{cw}$	Krohne Optiflux 2300	Electromagnetic	max ±0.25% of read	0...50.0 l/s

characteristics of the system and ejector, i.e., key performance parameters as a function of condensation temperature, were studied.

The tests can be divided into several measurement campaigns, distinguished by testing a smaller or larger prototype, using different heat exchanger configurations, applying a different ejector geometry, using different refrigerants, or conducting tests for different measurement parameters. The changes made during the tests in the refrigeration systems are explained in Chapter 3.4 and justified in Chapter 5.

Measurement campaign MC-1 examined the MARANI CHILLER 200 prototype in its basic version under design and off-design conditions. The waste heat used to drive the refrigeration system came from the oil system of the air compressors. The ejector set I showed in Table 2.3 was used in this configuration. The refrigerant tested was R1233zd(E). Measurements were made for the variant of high-temperature cooling, i.e., with the evaporation temperature at about 11°C and the chilled water temperature at 19°C/16°C, respectively at inlet/outlet of the evaporator. The cooling system was tested in two measurement sessions, with variations in heat source of 150 kW and 170 kW and the hot water temperature in the range of 60°C to 63°C.

After modifying the heating system and replacing the ejector mixing chamber and diffuser with set II (Table 2.3), the MC-2 measurement campaign was repeated for MARANI CHILLER 200. The refrigerant was not changed, but the ejector-based system could be operated at design conditions with a waste heat transfer rate supply of 200 kW and a hot water temperature of about 70°C. The refrigeration system was tested under standard cooling conditions, where the glycol temperature was maintained at 12°C/6°C and under high-temperature cooling conditions of 19°C/16°C, respectively, at the evaporator inlet/outlet.

The last measurement campaign for the MARANI CHILLER 200 refrigeration system was the MC-3, performed after the refrigeration system was modified to operate without the recuperative exchanger downstream of the ejector. For this measurement campaign, measurement series were again performed for standard and high-temperature cooling at variable condensation temperatures, again obtaining the operating characteristics of the refrigeration system. The supply conditions remained unchanged at a heat transfer rate of 200 kW and a hot water temperature of 70°C. The working fluid used again was R1233zd(E).

In the case of the MARANI CHILLER 600 prototype, after commissioning the system driven with the steam and solving the start-up problems, a test was carried out using

R1233zd(E) refrigerant, which was designated as MC-4. A set of three ejectors was used, the geometry of which corresponded to the dimensions of the ejectors designated as set II in Table 2.3. Due to the cumbersome control of the steam system in terms of the required operating parameters, five measuring points were recorded with varying cooling capacity parameters ranging from those for high-temperature cooling to those for standard cooling at a constant saturation temperature in the condenser of 23°C and with a variable driving heat transfer rate in the range of 490 - 570 kW and a steam inlet temperature of 140°C to 145°C.

Finally, after another modification of the heating system described in Chapter 3.4 to lower the parameters of the drive steam and modification of the refrigeration system to accommodate testing on R1234zd(E) refrigerant, another measurement campaign was carried out for the MARANI CHILLER 600 prototype designated as MC-5. This measurement series used a single ejector, specified in Table 2.3 as set II. Several results were obtained under standard 12°C/6°C cooling conditions and several measurement points for elevated condensation temperatures. Heating power simulating waste heat ranged from 570 - 645 kW with steam temperatures at the generator inlet in the 95°C - 120°C range.

3.3 Data processing and measurement uncertainty

All measurement points were recorded under steady-state conditions to monitor changes in crucial refrigeration system operating parameters over a period of about 10 min for each operating point, which corresponded to about 600 individual readings. In addition, the steady-state conditions were verified in the generated database files by selecting steady-state areas. According to Eq. (3.1), the results were arithmetically averaged for each operating point.

$$\bar{x} = \frac{1}{n}\sum_{i=1}^{n} x_i \tag{3.1}$$

where x is a directed measured quantity and n is the number of measurements.

The type A measurement uncertainty was calculated using the standard deviation for each directly measured quantity, based on Eq. (3.2).

$$u_A = \sqrt{\frac{1}{n-1}\sum_{i=1}^{n}(x_i - \bar{x})^2} \tag{3.2}$$

Based on the reference measurement accuracy of the measurement equipment, shown in Tab. 3.1 and 3.2, the systematic error representing the Type B measurement uncertainty was also calculated, assuming a rectangular probability distribution from Eq. (3.3).

$$u_B = \frac{a}{\sqrt{3}} \tag{3.3}$$

where a is an absolute limit error. The absolute limit error a is calculated individually for each measuring instrument. For Pt100 class A temperature sensors, a is determined using Eq. (3.4)

$$a = \pm (0.002 \cdot t + 0.15)\,\mathrm{K} \tag{3.4}$$

where t is the measured temperature. In the case of pressure transmitters, the a value is the accuracy determined in Table 3.1 as ± 0.15% of the set span. In the case of flow meters, the magnitude a was read by linear interpolation from the individual accuracy tables of the measuring instrument depending on the readings in the calibrated range.

Finally, the standard complex uncertainty of a single directly measured quantity representing the composite uncertainty was calculated as the root of the sum of squares of the two aforementioned types of uncertainty, based on Eq. (3.5).

$$u = \sqrt{u_A^2 + u_B^2} \tag{3.5}$$

The thermodynamic properties of the R1233zd(E) refrigerant and heat transfer fluids at each operating point were calculated using REFPROP 10.0 [82]. Based on direct measurements, the crucial system performance parameters were calculated. The uncertainty of indirectly measured quantities was computed using the Law of Propagation of Uncertainties, according to Eq. (3.6).

$$u(y) = \sqrt{\left(\frac{\partial y}{\partial x_i}\right)^2 \cdot u^2(x_i)} \tag{3.6}$$

where y is indirectly measured quantity and x_i represents all quantities taken into account to calculate y. All calculations were performed using Microsoft Excel software with Visual Basic for Applications.

3.4 Modifications made during the test campaign

As mentioned in the previous sections of this chapter, several modifications to refrigeration systems were carried out to enable experimental testing, get closer to the nominal parameters of the designed refrigeration units, and, finally, improve the efficiency of their operation. Modifications also touched the auxiliary installations simulating the source of waste heat in the case of the MARANI CHILLER 600 refrigeration system or the actual source of waste heat, the air compressors in the case of an experimental campaign of MARANI CHILLER 200.

The first changes to the ejector-based system driven by low-temperature 200 kW waste heat were made after the first commissioning tests. One such measure was eliminating a faulty check valve at the outlet of the circulating pump. Its improper operation caused the lack of refrigerant flow. This was due to low saturation pressure, which caused design pressure drops in the connecting pipelines assumed at the conventional level to be unacceptable for the applied working fluid. This required changes in the low-pressure part of the system to avoid excessive pressure drops. After the above modifications, the system operated correctly regarding the required mass flow rates.

After the first tests of the ejector-based system MC-1, it was found that the performance of the ejector operating with the low-pressure refrigerant R1233zd(E) differed from those known in the literature refrigerants applied to similar installations. Therefore, differences in the available overall ejector efficiency were demonstrated in comparison with a theoretical prediction, which will be analyzed further in the next part of the thesis. This led to verifying the efficiency ratios of the ejector adopted for calculations, introducing a correction using a smaller diameter mixing chamber, and changing the ejector geometry from ejector set I to ejector set II. Experimental results leading to the above conclusions are presented in Chapter 5.

Moreover, during the test campaign MC-1, it was impossible to obtain design conditions because the waste heat transfer rate was too low. These problems were due to the mismatch between the oil-water heat exchangers receiving heat from the oil system of the air compressors, which were selected for much higher temperature differentials for heating domestic water, thus having an insufficient heat exchange surface. For this reason, the heating system was modified by attaching heat recovery from the oil system of the third air compressor, providing an additional heat transfer rate.

Subsequently, after the MC-2 measurement campaign, further changes were made to the refrigeration system, resulting from the need to reduce pressure drops in the refrigeration system and allow the system to work under standard cooling conditions. A layout of the modified refrigeration system, including the measurement sensors used in the MC-3 measurement campaign, is shown in Fig. 3.5. In that case, the recuperator, a source of pressure loss at the ejector outlet, was eliminated. The recuperator lowered the condensation temperature by about 3 - 4 K, causing the unit operating characteristics to break down prematurely and go into the off-design mode, which is described in Chapter 5. In addition, a second plate heat exchanger acting as a condenser was installed in parallel, reducing the required difference between the condensing refrigerant and cooling water temperatures.

Significant challenges were encountered for the 600 kW waste heat-driven refrigeration system in accessing the required high-temperature thermal power and providing additional power to load the evaporator. Additionally, ensuring adequate discharge of the total heat transfer rate from the condenser required particular infrastructure. Given the current conditions, the Thermal Technology Laboratory at Bialystok University of Technology was the only facility capable of providing such power while maintaining stable operating conditions.

Extensive construction and supporting infrastructure were required to connect the system to the heat load and discharge system. This included adjustments to heat transfer loops, connection modifications, and hydraulic system enhancements. Numerous commissioning and repair works were undertaken to address issues related to

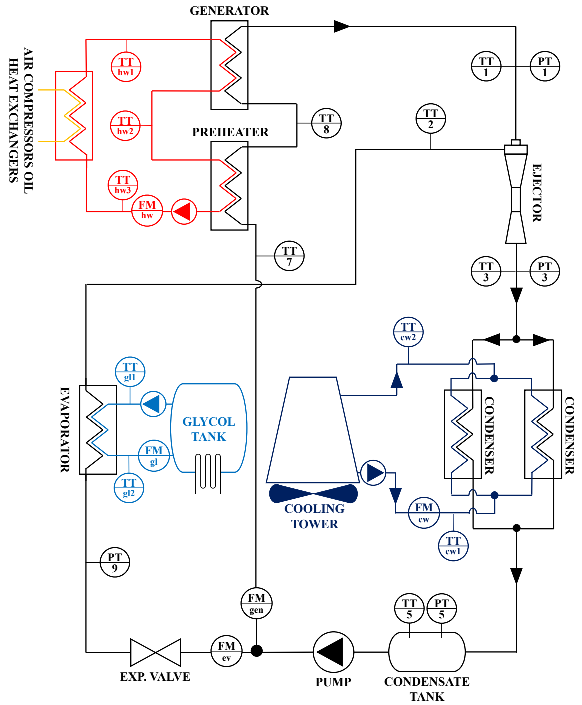

FIGURE 3.5: Modified MARANI CHILLER 200 kW test rig, with the measurement instruments marked as follows: PT - pressure transmitter, TT - temperature transmitter, FM - flow meter, and fluids indexes as follows: hw - hot steam/water, gl - glycol-water solution, cw - cold water

achieving stable system operation.

The metering system was upgraded with an additional measurement and control system to ensure a stable heating power supply at the required level and temperature. It is worth noting that the refrigeration system heat exchangers (generator and preheater) were initially designed to operate with a glycol solution as the waste heat source. However, due to the lack of available infrastructure with very high thermal power for research purposes, it was necessary to use heating steam, which altered the operating conditions of these two heat exchangers.

For the above reason, after testing the refrigeration system in the MC-4 measurement campaign, the preheater and one of the two generators were eliminated in the next stage to reduce refrigerant overheating at the motive inlet to the ejector. In addition, as a result of the need to test the system on R1234ze(E) refrigerant in the MC-5 measurement campaign, the set of three ejectors was replaced by a single ejector with a geometry corresponding to set III from Tab. 2.3. The modified refrigeration system with measuring instruments is shown in Fig. 3.6.

Moreover, before the MC-5 campaign, the steam plant was modified again by installing heat buffers with the possibility of connecting a vacuum pump, which translated into the possibility of lowering the steam saturation pressure below the ambient pressure. Thus, it was possible to achieve steam temperatures below 100°C to simulate a low-temperature waste heat source.

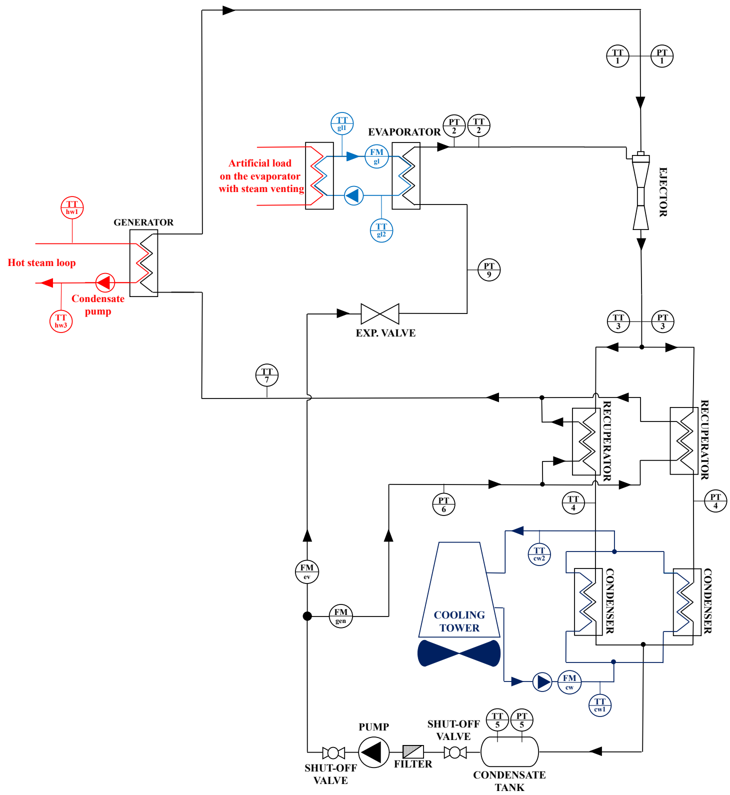

FIGURE 3.6: Modified MARANI CHILLER 600 kW test rig, with the measurement instruments marked as follows: PT - pressure transmitter, TT - temperature transmitter, FM - flow meter, and fluids indexes as follows: hw - hot steam/water, gl - glycol-water solution, cw - cold water

Chapter 4

Mathematical model of the system components

An iterative model has been developed for the thermodynamic analysis of the ejector-based refrigeration system, specifically focusing on designing cooling aggregates of different capacities and a range of configurations based on two tested refrigeration systems. This model, built from the models of the individual components, features a mathematical algorithm that includes models of standard refrigeration system components, i.e., expansion valve, evaporator, and condenser, and non-standard devices, i.e., supersonic ejector, circulating pump, and generator. The system model also includes a simulation of an additional heat exchanger - a recuperator, and the possibility of modeling the separation of heat exchangers used to collect waste heat to the generator and preheater. Consequently, there are four design configurations of the refrigeration system, highlighted in Fig. 4.1:

- V1 - system without a recuperator and without a preheater
- V2 - system with a recuperator and without a preheater
- V3 - system without a recuperator and with a preheater
- V4 - system with a recuperator and with a preheater

The software can estimate the crucial performance parameters of refrigeration systems, such as COP, electric power demand, and heat transfer rates. It also predicts the critical dimensions and efficiency parameters of the ejector and heat exchangers, considering information about waste heat and the demand for cooling capacity as input data. The model assumes three levels of refrigerant pressure present in the refrigeration system: high saturation pressure in the generator p^r_{gen}, fluid saturation pressure in the condenser p^r_{cond}, and low saturation pressure in the evaporator p^r_{evap}. The model calculates pressure drops across the heat exchangers, which are used to evaluate the selection of heat exchangers and the selection of the circulating pump.

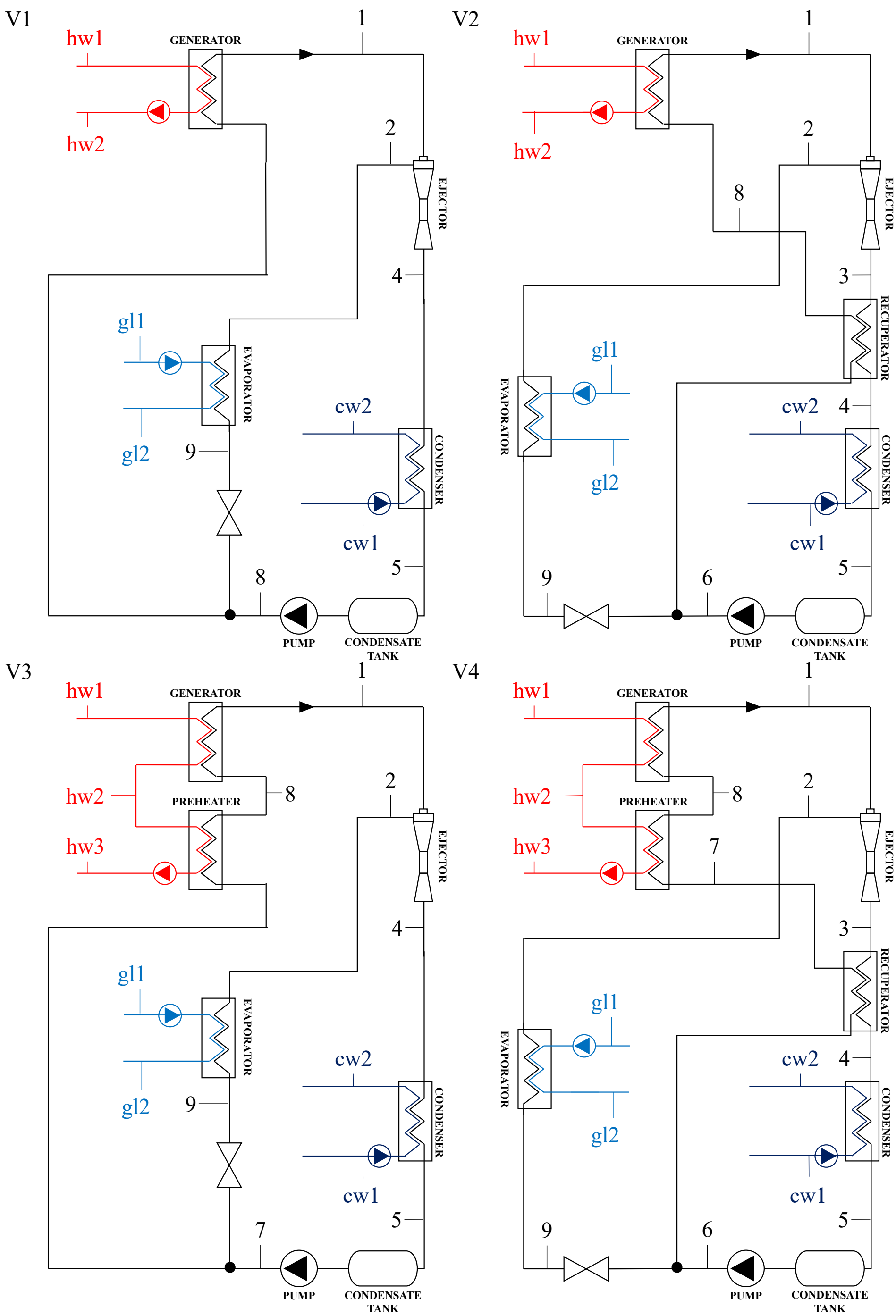

FIGURE 4.1: Variants of refrigeration system configurations

4.1 Ejector

The most crucial part in modeling the ejector-based refrigeration system is appropriately estimating ejector performance and outlet parameters, with minimal computational cost to optimize the system in many operation conditions and power range variants. For this reason, a simple 0-D ejector model, based on the work of Chen et al. [73] and Kumar et al. [71], was used. Combining these two models allows the ejector performance to be calculated at critical and subcritical conditions, considering the frictional losses in the mixing chamber. The following assumptions were made:

- a steady, adiabatic flow was assumed along the ejector,
- flow velocities at the motive and suction inlets were assumed as 0,
- the absolute pressure and specific enthalpy at the inlets and the absolute pressure at the outlet of the ejector were taken as the boundary conditions of the model,
- motive and suction streams start mixing under constant pressure in a hypothetical throat cross-section of the ejector; before the independent streams were considered,
- a constant frictional factor throughout the mixing chamber was assumed,
- Fanno flow in the mixing chamber was assumed,
- the real gas properties were assumed.

The model uses the author's approach to calculating a hypothetical throat in an ejector mixing chamber. In the literature, models are dominated by the assumption of reaching the speed of sound by the medium entrained into the ejector. Here, the assumption of an iterative adjustment of the pressure in the hypothetical throat between the critical pressure and the suction inlet pressure for which the entrained flow is the highest was adopted.

The model is divided into two sections: one for prediction of the ejector geometry, called ejector design mode (EJD), and the second for performance evaluation of the ejector with known geometry, called ejector analysis mode (EJA), where calculation under on-design and off-design conditions is possible.

The following input values are required for a particular mode:

- for EJD:
  - the motive nozzle and the diffuser divergence angle γ_{mn} and γ_{dif},
  - mixing chamber length/diameter ratio k_{mix},
  - inlet motive and suction nozzle mass flow rates $\dot{m}_{mn} = \dot{m}^r_{gen}$, $\dot{m}_{sn} = \dot{m}^r_{evap}$,
- for EJA:

  - the characteristic diameters of the ejector motive nozzle throat $d_{mn,th}$, motive nozzle outlet $d_{mn,out}$, mixing chamber d_{mix}, and diffuser outlet $d_{dif,out}$,
  - the characteristic lengths of motive nozzle divergence section $l_{mn,th-out}$, mixing chamber l_{mix}, and diffuser l_{dif},

- for both modes:
  - the inlet thermodynamic parameters: specific enthalpy at the motive nozzle inlet $h_{mn,in} = h_1$, absolute pressure at the motive nozzle inlet $p_{mn,in} = p^r_{gen}$, specific enthalpy at the suction nozzle inlet $h_{sn,in} = h_2$, absolute pressure at the suction nozzle inlet $p_{sn,in} = p^r_{evap}$,
  - outlet pressure: p^r_{cond},
  - type of refrigerant,
  - the characteristic efficiencies of the ejector: motive nozzle (η_{mn}), of expansion from the motive nozzle to hypothetical throat ($\eta_{mn,out,hyp}$), suction nozzle (η_{sn}), mixing chamber (η_{mix}), diffuser (η_{dif}).

Motive and suction nozzle inlets

Regardless of the mode of calculation, first, the temperature, specific entropy, and density of the refrigerant at the motive ($T_{mn,in}$, $s_{mn,in}$, $\rho_{mn,in}$) and suction nozzle inlets ($T_{sn,in}$, $s_{sn,in}$, $\rho_{sn,in}$) are calculated using REFPROP libraries based on absolute pressure and specific enthalpy, according to Eqs (4.1) and (4.2).

$$T_{mn,in}, s_{mn,in}, \rho_{mn,in} = f\left(p_{mn,in}, h_{mn,in}\right) \tag{4.1}$$

$$T_{sn,in}, s_{sn,in}, \rho_{sn,in} = f\left(p_{sn,in}, h_{sn,in}\right) \tag{4.2}$$

Motive nozzle throat

Then, the motive nozzle throat pressure $p_{mn,th}$ is iteratively adjusted to obtain the speed of sound in that cross-section, assuming isentropic expansion of the primary fluid inside the converging section of the nozzle. Thus, the specific enthalpy and speed of sound in that cross-section, respectively $h_{mn,th,is}$ and $a_{mn,th,is}$, is calculated from Eqs (4.3) and (4.4), based on the absolute pressure in that cross-section ($p_{mn,th}$) and the specific entropy at the motive nozzle inlet ($s_{mn,in}$). The velocity of the fluid reached in the motive nozzle throat is calculated from the energy conservation equation (Eq. (4.5)). The velocity at the motive nozzle inlet $w_{mn,in}$ is assumed to be 0.

$$h_{mn,th,is} = h\left(p_{mn,th}, s_{mn,in}\right) \tag{4.3}$$

$$a_{mn,th,is} = h\left(p_{mn,th}, s_{mn,in}\right) \tag{4.4}$$

$$w_{mn,th} = \sqrt{2 \cdot \left(h_{mn,in} - h_{mn,th,is}\right) + w_{mn,in}^2} \tag{4.5}$$

Then, in EJD the motive nozzle throat diameter $d_{mn,th}$ is calculated from the equation for the area of a circular cross-section (Eq. (4.6)), where the area of nozzle throat $A_{mn,th}$ is evaluated based on mass conservation equation (Eq. (4.7)). The same equations are used for EJA to calculate the motive mass flow rate $\dot{m}_{mn}$ based on known geometry.

$$d_{mn,th} = \sqrt{\frac{4 \cdot A_{mn,th}}{\pi}} \tag{4.6}$$

$$A_{mn,th} = \frac{w_{mn,th} \cdot \rho_{mn,th}}{\dot{m}_{mn}} \tag{4.7}$$

Motive nozzle outlet

To calculate the motive nozzle outlet parameters in EJD mode, $p_{mn,out} = p_{sn,in}$ is assumed. The specific enthalpy at the motive nozzle outlet $h_{mn,out}$ is calculated from Eq. (4.8) assuming the isentropic efficiency of the nozzle diverging part η_{mn}.

$$h_{mn,out} = h_{mn,th} - \eta_{mn} \cdot \left(h_{mn,th} - h_{mn,out,is}\right) \tag{4.8}$$

The required properties of the working fluid in this cross-section, i.e., temperature ($T_{mn,out}$), density ($\rho_{mn,out}$), specific entropy ($s_{mn,out}$), and speed of sound ($a_{mn,out}$) are then calculated using REFPROP libraries from Eq. (4.9).

$$T_{mn,out}, \rho_{mn,out}, s_{mn,out}, a_{mn,out} = f\left(p_{mn,out}, h_{mn,out}\right) \tag{4.9}$$

The velocity at the motive nozzle outlet $w_{mn,out}$ is calculated from Eq. (4.10).

$$w_{mn,out} = \sqrt{2 \cdot \left(h_{mn,th} - h_{mn,out}\right) + w_{mn,th}^2} \tag{4.10}$$

For EJA, $p_{mn,out}$ is iteratively adjusted to obtain the same $w_{mn,out}$ from Eq. (4.10) and mass conservation equation (Eq. (4.11)),

$$w_{mn,out} = \frac{\dot{m}_{mn}}{A_{mn,out} \cdot \rho_{mn,out}} \tag{4.11}$$

where $A_{mn,out}$ is the surface area of the motive nozzle outlet, calculated from Eq. (4.12).

$$A_{mn,out} = \frac{\pi \cdot d_{mn,out}^2}{4} \tag{4.12}$$

The remaining parameters are calculated as in EJD.

In EJD, the diameter of the nozzle outlet $d_{mn,out}$ is calculated from Eq. (4.12), while the $A_{mn,out}$ is previously evaluated from Eq. (4.11). The length of the diverging part of the nozzle $l_{mn,th-out}$ is calculated using Eq. (4.13).

$$l_{mn,th-out} = \frac{d_{mn,out} - d_{mn,th}}{2 \cdot tg\left(\frac{\gamma_{mn}}{2}\right)} \tag{4.13}$$

Hypothetical throat cross-section

The hypothetical throat is the last cross-section, where the two fluid flows are considered separately. For EJA, the mixing chamber diameter d_{mix} is known from the input data, and in EJD, d_{mix} is the adjusted variable. For each guessed or known value of the diameter d_{mix}, the critical pressure is calculated, i.e., the pressure for which the refrigerant entrained into the suction chamber reaches the speed of sound in the considered cross-section of the ejector. The critical pressure $p_{sn,hyp,crit}$ is iteratively adjusted analogously to the motive nozzle throat cross-section using Eq. (4.14) to calculate specific enthalpy ($h_{shyp,is,crit}$) at the critical pressure and Eq. (4.15) to calculate speed of sound ($a_{shyp,is,crit}$) after isentropic expansion of the entrained refrigerant and comparing it with the velocity $w_{shyp,crit}$ calculated from Eq. (4.16), where the velocity at the suction nozzle inlet $w_{sn,in}$ is assumed 0.

$$h_{shyp,is,crit} = h\left(p_{sn,hyp,crit}, s_{sn,in}\right) \tag{4.14}$$

$$a_{shyp,is,crit} = h\left(p_{sn,hyp,crit}, s_{sn,in}\right) \tag{4.15}$$

$$w_{shyp,crit} = \sqrt{2 \cdot \left(h_{sn,in} - h_{shyp,is,crit}\right) + w_{sn,in}^2} \tag{4.16}$$

Then, in the hypothetical throat, the pressure $p_{hyp,th}$ is adjusted in the range between the critical pressure ($p_{sn,hyp,crit}$) and the suction inlet pressure ($p_{sn,in}$), to find the maximal value of the mass flow rate at the suction nozzle inlet ($\dot{m}_{sn}$). The diameter d_{mix} is changed until the value of $\dot{m}_{sn}$ reaches the assumed design value. This is the main change compared to the models used previously in the literature, which assumed a Mach number of 1 for the suction nozzle in that cross-section. For the assumed mixing chamber diameter d_{mix}, the mixing chamber area A_{mix} is calculated from Eq. (4.17).

$$A_{mix} = \frac{\pi \cdot d_{mix}^2}{4} \tag{4.17}$$

The specific enthalpy of the motive flow in the section under discussion h_{mhyp} is calculated as a quantity after isentropic expansion from the motive nozzle outlet $h_{mhyp,is}$ from Eq. (4.18).

$$h_{mhyp} = h_{mhyp,is} = h\left(p_{hyp,th}, s_{mn,out}\right) \tag{4.18}$$

The specific enthalpy of the suction fluid h_{shyp} is calculated from Eq. (4.19), assuming the isentropic efficiency of the suction nozzle η_{sn},

$$h_{shyp} = h_{sn} - \eta_{sn} \cdot \left(h_{sn} - h_{shyp,is}\right) \tag{4.19}$$

where $h_{shyp,is}$ is an isentropic enthalpy calculated as a value after isentropic expansion from the suction nozzle inlet from Eq. (4.20).

$$h_{shyp,is} = h\left(p_{hyp,th}, s_{sn,in}\right) \tag{4.20}$$

The other thermodynamic parameters such as temperature, density, specific entropy, and speed of sound for both streams are evaluated based on REFPROP libraries from Eqs (4.21), (4.22).

$$T_{mhyp}, \rho_{mhyp}, s_{mhyp}, a_{mhyp} = f\left(p_{hyp,th}, h_{mhyp}\right) \tag{4.21}$$

$$T_{shyp}, \rho_{shyp}, s_{shyp}, a_{shyp} = f\left(p_{hyp,th}, h_{shyp}\right) \tag{4.22}$$

The velocity of the motive fluid w_{mhyp} is calculated from Eq. (4.23).

$$w_{mhyp} = \sqrt{2 \cdot \left(h_{mn,out} - h_{mhyp}\right) + w_{mn,out}^2} \tag{4.23}$$

Similarly, the velocity of the suction fluid w_{shyp} is calculated, using Eq. (4.24),

$$w_{shyp} = \sqrt{2 \cdot \left(h_{sn,in} - h_{shyp}\right) + w_{sn,in}^2} \tag{4.24}$$

where suction inlet velocity $w_{sn,in}$ is assumed as 0.

The area occupied by the motive fluid in the hypothetical throat cross-section is calculated from the modified mass conservation equation in Eq. (4.25), where $\eta_{mn,out,hyp}$ describes the expansion efficiency of the motive fluid outside the motive nozzle.

$$A_{mhyp} = \frac{\eta_{mn,out,hyp} \cdot \dot{m}_{mn}}{\rho_{mhyp} \cdot w_{mhyp}} \tag{4.25}$$

The area of the annular cross-section occupied by the suction fluid A_{shyp} in the mixing chamber is calculated from Eq. (4.26).

$$A_{shyp} = A_{mix} - A_{mhyp} \tag{4.26}$$

Finally, the guess value of suction mass flow rate $\dot{m}_{sn,guess}$ predicted during the iteration is calculated from Eq. (4.27).

$$\dot{m}_{sn,guess} = A_{shyp} \cdot w_{shyp} \cdot \rho_{shyp} \tag{4.27}$$

In EJD, the calculations are finished when $\dot{m}_{sn,guess}$ is equal to the suction mass flow rate from the input data $\dot{m}_{sn}$. In the case of EJA, when the ejector is operating in critical mode, the hypothetical throat $p_{hyp,th}$ with the same limits is adjusted to obtain the maximal suction mass flow rate.

Mixing chamber inlet

The mixing chamber inlet is stated for the same cross-section as the hypothetical throat; however, the refrigerant fluxes are considered as being fully mixed. In EJD, the mixing chamber length is calculated, assuming the length/diameter ratio k_{mix}, from Eq. (4.28).

$$l_{mix} = k_{mix} \cdot d_{mix} \tag{4.28}$$

For both modes, the velocity in that cross-section w_{mix} is estimated from the momentum balance equation, with the assumption of the coefficient η_{mix} representing the frictional losses during mixing (Eq. (4.29)).

$$w_{mix,in} = \eta_{mix} \cdot \frac{\dot{m}_{mn} \cdot w_{mhyp} + \dot{m}_{sn} \cdot w_{shyp}}{\dot{m}_{mn} + \dot{m}_{sn}} \tag{4.29}$$

The specific enthalpy $h_{mix,in}$ is calculated from the energy balance equation (Eq. (4.30)).

$$h_{mix,in} = \frac{\dot{m}_{mn} \cdot \left(h_{mhyp} + \frac{w_{mhyp}^2}{2}\right) + \dot{m}_{sn} \cdot \left(h_{shyp} + \frac{w_{shyp}^2}{2}\right)}{\dot{m}_{mn} + \dot{m}_{sn}} - \frac{w_{mix,in}^2}{2} \tag{4.30}$$

The other required parameters, i.e., temperature $T_{mix,in}$, density $\rho_{mix,in}$, specific entropy $s_{mix,in}$, speed of sound $a_{mix,in}$, dynamic viscosity $\mu_{mix,in}$, isentropic expansion coefficient $\kappa_{mix,in}$ in this cross-section are estimated based on the specific enthalpy and absolute pressure $p_{mix,in}$ from Eq. (4.31),

$$T_{mix,in}, \rho_{mix,in}, s_{mix,in}, a_{mix,in}, \mu_{mix,in}, \kappa_{mix,in} = f\left(h_{mix,in}, p_{mix,in}\right) \tag{4.31}$$

where $p_{mix,in}$ is equals $p_{hyp,th}$. Reynolds number at mixing chamber inlet ($\mathrm{Re}_{mix,in}$) is calculated from Eq. (4.32).

$$\mathrm{Re}_{mix,in} = \frac{w_{mix,in} \cdot d_{mix} \cdot \rho_{mix,in}}{\mu_{mix,in}} \tag{4.32}$$

Mixing chamber outlet

The mixing chamber outlet cross-section represents the outlet of the mixing chamber before the velocity decreases below a Mach number of 1. The parameters are calculated by iterative adjustment of the specific enthalpy $h_{mix,out}$, absolute pressure $p_{mix,out}$, and the Mach number $Ma_{mix,out}$ at the mixing chamber outlet to converge the gas dynamic equations Eqs (4.33) and (4.34) and the Fanno flow equation Eq. (4.35) [83], in which the friction factor f_m is calculated from the Schlichting equation [84] (Eq. (4.36)).

$$\frac{1+\frac{\kappa_{mix,avg}-1}{2}\cdot Ma^2_{mix,in}}{1+\frac{\kappa_{mix,avg}-1}{2}\cdot Ma^2_{mix,out}}-\frac{T_{mix,out}}{T_{mix,in}}=0 \tag{4.33}$$

$$\frac{Ma_{mix,in}}{Ma_{mix,out}}\cdot\sqrt{\frac{1+\frac{\kappa_{mix,avg}-1}{2}\cdot Ma^2_{mix,in}}{1+\frac{\kappa_{mix,avg}-1}{2}\cdot Ma^2_{mix,out}}}-\frac{p_{mix,out}}{p_{mix,in}}=0 \tag{4.34}$$

$$\begin{aligned}\frac{\kappa_{mix,avg}+1}{2\cdot\kappa_{mix,avg}}\cdot ln\left(\frac{1+\frac{\kappa_{mix,avg}-1}{2}\cdot Ma^2_{mix,out}}{1+\frac{\kappa_{mix,avg}-1}{2}\cdot Ma^2_{mix,in}}\right)-\frac{1}{\kappa_{mix,avg}}\left(\frac{1}{Ma^2_{mix,out}}-\frac{1}{Ma^2_{mix,in}}\right)\\-\frac{\kappa_{mix,avg}+1}{2\cdot\kappa_{mix,avg}}\cdot ln\left(\frac{Ma^2_{mix,out}}{Ma^2_{mix,in}}\right)-\frac{f_m\cdot l_{mix}}{d_{mix}}=0\end{aligned} \tag{4.35}$$

$$1/\sqrt{f_m}=2\cdot log\left(Re_{mix,avg}\cdot\sqrt{f_m}\right)-0.8 \tag{4.36}$$

To calculate the above equations for each iteration of $h_{mix,out}$, $p_{mix,out}$ and $Ma_{mix,out}$ the following calculations need to be performed. The thermal properties for the mixing chamber outlet, i.e., temperature $T_{mix,out}$, density $\rho_{mix,out}$, specific entropy $s_{mix,out}$, speed of sound $a_{mix,out}$, dynamic viscosity $\mu_{mix,out}$, and isentropic expansion coefficient $\kappa_{mix,out}$ are calculated based on REFPROP libraries from Eq. (4.37).

$$T_{mix,out},\rho_{mix,out},s_{mix,out},a_{mix,out},\mu_{mix,out},\kappa_{mix,out}=f\left(h_{mix,out},p_{mix,out}\right) \tag{4.37}$$

The velocity at the mixing chamber outlet $w_{mix,out}$ is calculated from Mach number definition from Eq. (4.38).

$$w_{mix,out}=Ma_{mix,out}\cdot a_{mix,out} \tag{4.38}$$

Reynolds number at the mixing chamber outlet ($\mathrm{Re}_{mix,out}$) is calculated from Eq. (4.39).

$$\mathrm{Re}_{mix,out}=\frac{w_{mix,out}\cdot d_{mix}\cdot\rho_{mix,out}}{\mu_{mix,out}} \tag{4.39}$$

The average mixing chamber isentropic expansion coefficient $\kappa_{mix,avg}$ and average Reynolds number $\mathrm{Re}_{mix,avg}$ are estimated using the arithmetic average for the mixing chamber inlet and outlet from Eqs (4.40) and (4.41).

$$\kappa_{mix,avg} = \frac{\kappa_{mix,in} + \kappa_{mix,out}}{2} \tag{4.40}$$

$$\mathrm{Re}_{mix,avg} = \frac{\mathrm{Re}_{mix,in} + \mathrm{Re}_{mix,out}}{2} \tag{4.41}$$

Diffuser inlet

The diffuser inlet section is assumed to be in the same section as the mixing chamber outlet, assuming subsonic flow and the shockwave occurrence. The temperature $T_{dif,in}$, absolute pressure $p_{dif,in}$ at the diffuser inlet are calculated from Eqs (4.42) and (4.43), respectively.

$$\frac{T_{dif,in}}{T_{mix,out}} = \left(2 + Ma^2_{mix,out} \cdot \left(\kappa_{mix,avg} - 1\right)\right) \frac{2 \cdot \kappa_{mix,avg} \cdot Ma^2_{mix,out} - \left(\kappa_{mix,avg} - 1\right)}{Ma^2_{mix,out} \cdot \left(\kappa_{mix,avg} + 1\right)^2} \tag{4.42}$$

$$\frac{p_{dif,in}}{p_{mix,out}} = \frac{1}{\kappa_{mix,avg} + 1} \cdot \left(2 \cdot \kappa_{mix,avg} \cdot Ma^2_{mix,out} - \left(\kappa_{mix,avg} - 1\right)\right) \tag{4.43}$$

The specific enthalpy $h_{dif,in}$ is estimated based on absolute pressure and temperature from Eq. (4.44), and other properties i.e. density $\rho_{dif,in}$, specific entropy $s_{dif,in}$, speed of sound $a_{dif,in}$ and isentropic expansion coefficient $\kappa_{dif,in}$ at the diffuser inlet are estimated based on Eq. (4.45).

$$h_{dif,in} = f\left(p_{dif,in}, T_{dif,in}\right) \tag{4.44}$$

$$T_{mix,out}, \rho_{mix,out}, s_{mix,out}, a_{mix,out}, \mu_{mix,out}, \kappa_{mix,out} = f\left(h_{mix,out}, p_{mix,out}\right) \tag{4.45}$$

The Mach number at the diffuser inlet $Ma_{dif,in}$ is calculated from Eq. (4.46).

$$Ma_{dif,in} = \sqrt{\frac{\left(\kappa_{mix,dif,avg} - 1\right) \cdot Ma^2_{mix,out} + 2}{2 \cdot \kappa_{mix,avg} \cdot Ma^2_{mix,out} - \left(\kappa_{mix,dif,avg} - 1\right)}} \tag{4.46}$$

where the isentropic expansion coefficient $\kappa_{mix,dif,avg}$ is an arithmetic average of the above quantity at the mixing chamber outlet and diffuser inlet sections calculated from Eq. (4.47).

$$\kappa_{mix,dif,avg} = \frac{\kappa_{mix,out} + \kappa_{dif,in}}{2} \tag{4.47}$$

The velocity at the diffuser inlet $w_{dif,in}$ is calculated using the Mach number definition (Eq. (4.48)).

$$w_{dif,in} = Ma_{dif,in} \cot a_{dif,in} \tag{4.48}$$

Diffuser outlet

For EJD mode, the diffuser outlet diameter $d_{dif,out}$ is calculated from Eq. (4.49), assuming k_{dif} ratio.

$$d_{dif,out} = k_{dif} \cdot d_{mix} \tag{4.49}$$

The diffuser length $l_{dif,out}$ is calculated from Eq. (4.50), assuming the diverging angle of the diffuser γ_{dif}.

$$l_{dif,out} = \frac{d_{dif,out} - d_{mix}}{2 \cdot tg\left(\gamma_{dif}/2\right)} \tag{4.50}$$

For both calculating modes, the cross-sectional area of the diffuser outlet $A_{dif,out}$ is calculated from Eq. (4.51).

$$A_{dif,out} = \frac{\pi \cdot d_{dif,out}^2}{2} \tag{4.51}$$

Isentropic specific enthalpy $h_{dif,out,is}$ is calculated from an energy conservation equation assuming outlet velocity of 0 from Eq. (4.52).

$$h_{dif,out,is} = \frac{h_{dif,in} + w_{dif,in}^2}{2} \tag{4.52}$$

The specific enthalpy at the diffuser outlet is then estimated from Eq. (4.53), assuming isentropic efficiency η_{dif}.

$$h_{dif,out} = h_{dif,in} + \frac{h_{dif,out,is} - h_{dif,in}}{\eta_{dif}} \tag{4.53}$$

The diffuser outlet pressure $p_{dif,out}$ is iteratively estimated in range $p_{dif,out}$ to 1.5 $p_{dif,out}$. For each iterated value of $p_{dif,out}$ the thermal properties i.e. temperature $T_{dif,out}$, density $\rho_{dif,out}$, specific entropy $s_{dif,out}$, speed of sound $a_{dif,out}$ and isentropic expansion coefficient $\kappa_{dif,out}$ at the diffuser outlet are estimated based on Eq. (4.54).

$$T_{dif,out}, \rho_{dif,out}, s_{dif,out}, a_{dif,out}, \kappa_{dif,out} = f\left(h_{dif,out}, p_{dif,out}\right) \tag{4.54}$$

The velocity at the ejector outlet $w_{dif,out}$ is calculated from the mass conservation equation defined in Eq. (4.55) and Mach number $Ma_{dif,out}$ from its definition in Eq. (4.56).

$$w_{dif,out} = \frac{\dot{m}_{mn} + \dot{m}_{sn}}{A_{dif,out} \cdot \rho_{dif,out}} \tag{4.55}$$

$$Ma_{dif,out} = \frac{w_{dif,out}}{a_{dif,out}} \tag{4.56}$$

The pressure $p_{dif,out}$ is iterated as long as Eq. (4.57) is satisfied.

$$\frac{p_{dif,out}}{p_{dif,in}} - \eta_{dif} \cdot \left(1 + \frac{\kappa_{dif,avg} - 1}{2} \cdot Ma^2_{dif,in}\right)^{\frac{\kappa_{dif,avg}}{\kappa_{dif,avg}-1}} = 0 \tag{4.57}$$

where $\kappa_{dif,avg}$ is the aritmetic average of the isentropic expansion coefficients $\kappa_{dif,in}$ and $\kappa_{dif,out}$.

In EJA mode, the condition that the ejector outlet pressure should be greater than the condensation pressure $p_{dif,out} > p_{cond,sat}$ is checked to confirm whether the ejector operates under on-design conditions. Otherwise, the hypothetical throat pressure $p_{hyp,th}$ is adjusted to obtain an outlet pressure equal to the condensation pressure and predict the MER of the ejector under off-design conditions. In that case, the mixing chamber efficiency η_{mix} is recalculated using Eq. (4.58), which was introduced by Chen et al. [73].

$$\eta_{mix} = \eta_{mix,old} \cdot \left(1 - 1.3 \cdot \frac{p_{cond,sat} - p_{crit}}{p_{crit}}\right) \tag{4.58}$$

Except for the thermal properties, the velocities of the refrigerant in the ejector characteristic cross-sections and the ejector primary dimensions in EJD mode, also key parameters of the ejector, are estimated as the output values. MER is calculated from Eq. (4.59).

$$MER = \frac{\dot{m}_{sn}}{\dot{m}_{mn}} \tag{4.59}$$

The pressure ratio, describing the compression ability of the ejector, is calculated from Eq. (4.60).

$$p_{ratio} = \frac{p_{dif,out}}{p_{sn,in}} \tag{4.60}$$

Finally, the total ejector efficiency η_{ej} defined by Elbel and Hrnjak in [85] is used to describe the ejector performance. It is given in Eq. (4.61).

$$\eta_{ej} = MER \cdot \frac{h\left(p_{dif,out}, s_{sn,in}\right) - h_{sn,in}}{h_{mn,in} - h\left(p_{dif,out}, s_{mn,in}\right)} \tag{4.61}$$

where $h\left(p_{dif,out}, s_{sn,in}\right)$ is the specific enthalpy after isentropic compression of the suction fluid to the ejector outlet pressure, and $h\left(p_{dif,out}, s_{mn,in}\right)$ is the specific enthalpy of the fluid after isentropic expansion to the ejector outlet pressure.

The calculation flowchart of the model is shown in Fig. 4.2.

Calibrating the ejector component efficiencies for the specific working fluid and operating conditions is crucial for proper calculation. In the EJD mode, the values of the motive nozzle and diffuser divergence angles and mixing chamber length/diameter ratio are assumed as fixed input values; however, depending on the approach adopted, they can be easily optimized with the model.

The iterative loops adjusting bounded parameters for zeroing conditional equations were created by applying the least squares method with the trust region reflective algorithm [86]. Brent method [87] was used to minimize the equations with boundaries.

The model provides the following output values:

- for EJD:
  - the characteristic diameters of the ejector motive nozzle throat $d_{mn,th}$, motive nozzle outlet $d_{mn,out}$, mixing chamber d_{mix}, and diffuser outlet $d_{dif,out}$,
  - the characteristic lengths of motive nozzle divergence section $l_{mn,th-out}$, mixing chamber l_{mix}, and diffuser l_{dif},
- for EJA:
  - inlet motive and suction nozzle mass flow rates $\dot{m}_{mn}$, $\dot{m}_{sn}$,
  - information about critical, subcritical, or backflow operation of the ejector
- for both modes:
  - thermal properties: temperature, absolute pressure, density, specific enthalpy, specific entropy in ejector characteristic sections,
  - transport parameters: mass flow rates, velocities, Mach number in ejector characteristic sections,
  - ejector performance parameters: mass entrainment ratio - MER, pressure ratio - p_{ratio}, ejector efficiency - η_{ej}

All input and output quantities are saved using the Pandas library [88] into so-called Data Frames, from where the data is used by models of other components and is taken to build the final calculation report.

4.2 Heat exchangers

Two approaches were used in the calculations of heat exchangers. Simplified calculations using energy conservation equations were applied to adjust the saturation

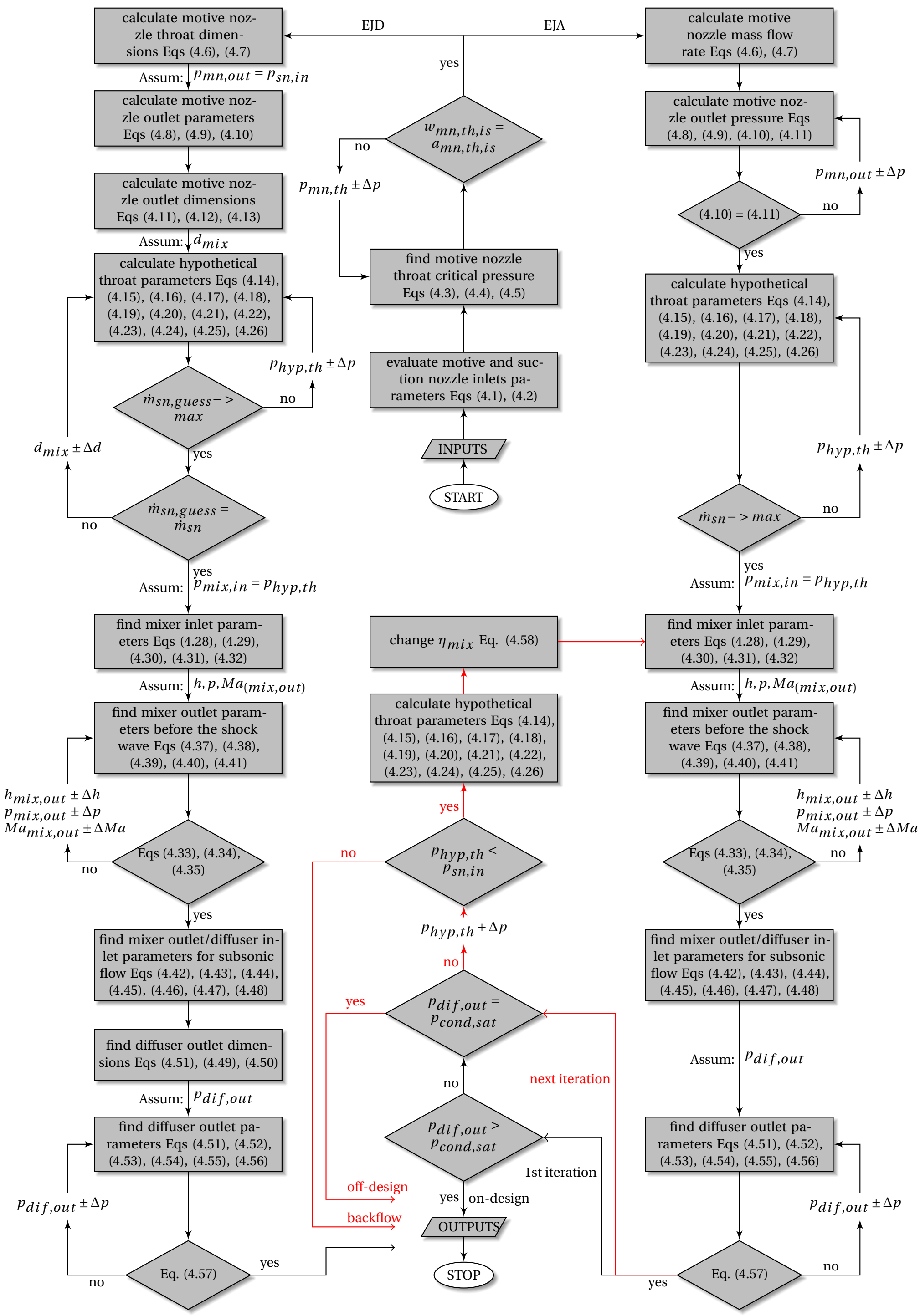

FIGURE 4.2: Ejector model calculation flowchart

pressure in the generator, evaporator, and condenser. Using a simplified model and the lack of need to calculate the plate heat exchanger model in each iteration simplified the iterative calculations, reducing their time.

The Logarithmic Mean Temperature Difference (LMTD) models for plate heat exchangers based on the work of Lee et al. [89] were used to calculate heat exchanger performance. They had the ability to be used in two modes: heat exchanger design (HXD) and heat exchanger analysis (HXA). In HXD, these models were used to predict the total heat transfer area, thus the number of heat exchanger plates, to select the appropriate heat exchanger for the required heat transfer rate. In the case of HXA, LMTD models were used to calculate the parameters at the heat exchanger outlets and estimate the pressure drops.

Simple model

In a simple model, the energy conservation equations are used to calculate the heat transfer rate for each section of the heat exchanger responsible for preheating, evaporation, and superheating of the refrigerant in the case of the vapor generator and the evaporator or for desuperheating, condensation, and subcooling the refrigerant in the condenser. Also, other quantities, such as specific enthalpy and temperatures at the ends of each section or mass flow rates of refrigerant or heat transfer fluids, are calculated using the mentioned equation depending on input data. The saturation pressure is modified until the value of the minimum temperature difference between the two heat-exchanging working fluids reaches the assumed pinch point temperature difference. The temperature distribution in the aforementioned heat exchangers is obtained. The simple models are described in detail for the generator, evaporator, and condenser in Chapters 4.2.1, 4.2.3, and 4.2.4, respectively.

LMTD model

The LMTD model of the heat exchanger requires the following input data:

- for HXD:
  - outlet temperature of the hot and cold fluids t_{out}^{hot}, t_{out}^{cold}
- for HXA:
  - number of plates of the heat exchanger N_t
- for both modes:
  - inlet temperature of the hot and cold fluids t_{in}^{hot}, t_{in}^{cold} or inlet specific enthalpy in case of fluids in two-phase state
  - mass flow rates of hot and cold fluids $\dot{m}^{hot}$, $\dot{m}^{cold}$

- hot and cold side medium
- hot and cold fluids inlet pressure p_{in}^{hot}, p_{in}^{cold}
- thermal conductivity of the wall k_w
- fouling factor R_f
- heat exchanger geometry, i.e.:
  * spacing between plates b,
  * chevron angle β,
  * wall width δ,
  * inlet ports diameters at hot and cold side D_p^{hot}, D_p^{cold}
  * horizontal distance between orifices L_h,
  * vertical distance between orifices L_v,
  * number of channels per pass N_p,
  * surface enlargement factor ϕ.

The geometric parameters of the plate heat exchanger are indicated in Fig. 4.3.

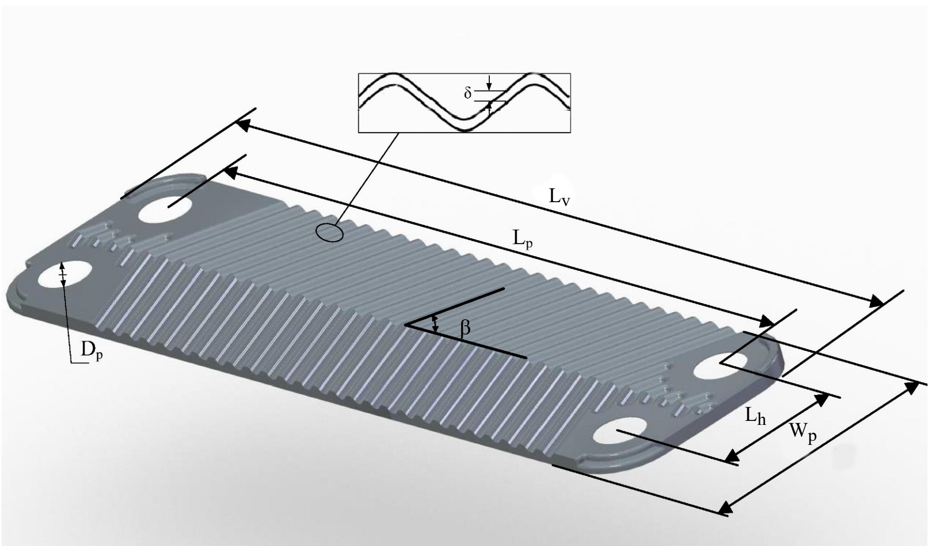

FIGURE 4.3: Geometric parameters of the plate heat exchanger: β - chevron angle, D_p - port diameter, δ - wall width, L_h - horizontal distance between orifices, L_p - plate length, L_v - vertical distance between orifices, W_p - plate width [90]

First, the geometric parameters of the heat exchanger are calculated. The heat exchanger plate width W_p is calculated from Eq. (4.62) and the plate length L_p from Eq. (4.63)

$$W_p = L_h + D_p \tag{4.62}$$

$$L_p = L_v - D_p \tag{4.63}$$

The effective heat transfer area of a single plate A_t is calculated from Eq. (4.64)

$$A_t = \phi \cdot W_p \cdot L_p \tag{4.64}$$

The single channel cross-section A_{ch} is defined by Eq. (4.65)

$$A_{ch} = W_p \cdot b \tag{4.65}$$

The hydraulic diameter D_h is calculated from Eq. (4.66)

$$D_h = \frac{2b}{\phi} \tag{4.66}$$

The specific enthalpies and temperatures are calculated and assigned to state points a, b, c, and d for the hot and cold side of the heat exchanger depending on the type of heat exchanger and on the inlet and outlet parameters taking into account the possible evaporation or condensation of the refrigerant, which is discussed in detail in Sections 4.2.1 to 4.2.5 for each type of heat exchanger. The sectional breakdown for the example heat exchanger is shown in Fig. 4.4.

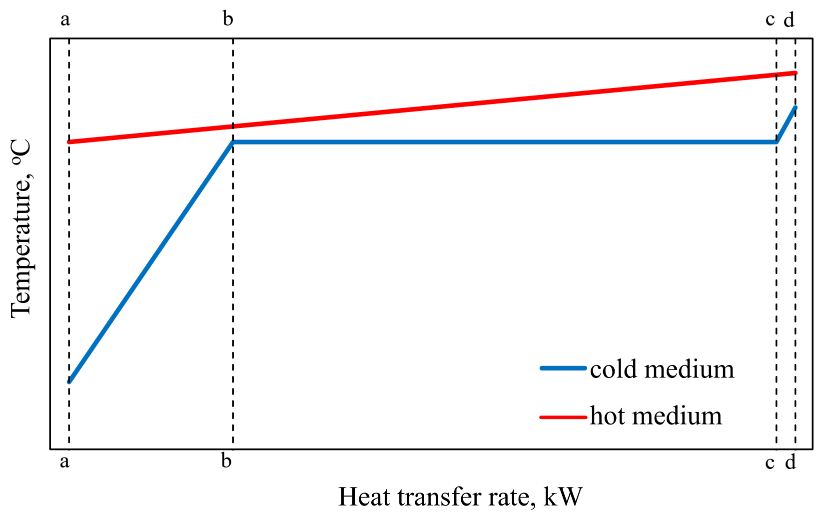

FIGURE 4.4: Temperature distribution of the example heat exchanger

The inlet and outlet density of the hot and cold fluids rho_{in}^{hot}, rho_{out}^{hot}, rho_{in}^{cold}, rho_{out}^{cold} are estimated using REFPROP libraries from Eq. (4.67), depending on the phase of the fluid in question.

$$\rho = f(p,t) = f(p,h) \tag{4.67}$$

The number of plates N_t in HXD is an iterated variable, while it is an input value in HXA. For the assumed or known value of N_t, the number of one-pass channels N_{cp} is calculated from Eq. (4.68).

$$N_{cp} = \frac{N_t - 1}{2 \cdot N_p} \tag{4.68}$$

The mass flux of cold and hot fluids are calculated from Eq. (4.69).

$$\dot{G} = 4 \cdot \frac{\dot{m}}{\pi D_p^2} \tag{4.69}$$

Then the mass flow rates in a single channel of the heat exchanger and the mass flux per channel of both fluids are defined by Eqs (4.70) and (4.71), respectively.

$$\dot{m}_{ch} = \frac{\dot{m}}{N_{cp}} \tag{4.70}$$

$$\dot{G}_{ch} = \frac{\dot{m}_{ch}}{A_{ch}} \tag{4.71}$$

The following calculations are performed for each heat exchanger section (a-b, b-c, c-d). The temperature differences at the hot and cold ends of a given heat exchanger section are calculated according to Eqs (4.72) and (4.73), where index 1 indicates the hot end and index 2 cold end of each section.

$$\Delta T_1 = t_1^{hot} - t_1^{cold} \tag{4.72}$$

$$\Delta T_2 = t_2^{hot} - t_2^{cold} \tag{4.73}$$

For each heat exchanger section, convective heat transfer coefficient α_i was calculated for cold and hot fluid from Eq. (4.74), where λ_f is a thermal conductivity of fluid determined for the average temperature of the fluid in each heat exchanger section.

$$\alpha_i = \frac{\mathrm{Nu}_i \cdot \lambda_f}{D_h} \tag{4.74}$$

The Nusselt number Nu is determined using the appropriate algorithm selected for each section of the individual heat exchanger of those described below.

- Nu-correlation-I - correlation for liquid refrigerant

The average temperature of the liquid in the section is calculated from Eq. (4.75), where t_{in} and t_{out} is the inlet and outlet liquid temperature in the heat exchanger section.

$$t_f = \frac{t_{in} + t_{out}}{2} \tag{4.75}$$

The refrigerant viscosity μ_f, Prandtl number Pr_f and thermal conductivity λ_f are calculated from REFPROP libraries based on temperature t_f and refrigerant pressure p^r. The refrigerant viscosity for wall temperature μ_w is assumed to be the same as μ_f. Then the Reynolds number is calculated from Eq. (4.76), where $\dot{G}_{ch}$ is the mass flux per channel defined in Eq. (4.71) and D_h is a hydraulic diameter defined in Eq. (4.66).

$$\mathrm{Re} = \frac{\dot{G}_{ch} \cdot D_h}{\mu_f} \tag{4.76}$$

The Nusselt number is determined according to the correlation of Wanniarachchi et al. [91] defined in Eq. (4.77).

$$\mathrm{Nu} = \left(\mathrm{Nu}_1^3 + \mathrm{Nu}_t^3\right)^{\frac{1}{3}} \cdot \mathrm{Pr}_f^{\frac{1}{3}} \cdot \left(\frac{\mu_f}{\mu_w}\right)^{0.17} \tag{4.77}$$

Nu_1 is defined in Eq. (4.78), where β is a chevron angle and ϕ is the surface enlargement factor of the heat exchanger. Nu_t is calculated from Eq. (4.79), where m is a coefficient calculated from Eq. (4.80).

$$\mathrm{Nu}_1 = 3.65 \cdot \beta^{-0.455} \cdot \phi^{0.661} \cdot \mathrm{Re}^{0.339} \tag{4.78}$$

$$\mathrm{Nu}_t = 12.6 \cdot \beta^{-1.142} \cdot \phi^{1-m} \cdot \mathrm{Re}^{m} \tag{4.79}$$

$$m = 0.646 + 0.0011 \cdot \beta \tag{4.80}$$

- Nu-correlation-II - correlation for refrigerant vapor

  The average temperature of the vapor in the heat exchanger section is calculated from Eq. (4.75). The refrigerant viscosity μ_f, Prandtl number Pr_f and thermal conductivity λ_f are calculated from REFPROP libraries based on temperature t_f and refrigerant pressure p^r. Then the Reynolds number is calculated from Eq. (4.76), where $\dot{G}_{ch}$ is the mass flux per channel defined in Eq. (4.71) and D_h is a hydraulic diameter defined in Eq. (4.66).

The Nusselt number is determined according to the correlation of Thonon et al. [92] defined in Eq. (4.81).

$$\mathrm{Nu} = 0.2267 \cdot \mathrm{Re}^{0.631} \cdot \mathrm{Pr}_f^{\frac{1}{3}} \tag{4.81}$$

- Nu-correlation-III - correlation for refrigerant evaporation

  The vapor quality q is calculated at the heat exchanger section inlet and outlet using REFPROP libraries based on refrigerant pressure p^r and inlet and outlet specific enthalpy h_{in} and h_{out}, respectively. The average vapor quality of the fluid in the section was calculated from Eq. (4.82).

$$q_m = \frac{q_{in} + q_{out}}{2} \tag{4.82}$$

  The refrigerant density ρ_l, viscosity μ_l, Prandtl number Pr_l and thermal conductivity λ_l in the liquid state are calculated from REFPROP libraries based on quality $q = 0$ and refrigerant pressure p^r and the refrigerant density ρ_g in the gas state based on quality $q = 1$ and refrigerant pressure p^r. The equivalent value of mass flux $\dot{G}_{eq}$ for two-phase flow is defined in Eq. (4.83), where $\dot{G}_{ch}$ is the mass flux per channel defined in Eq. (4.71).

$$\dot{G}_{eq} = \dot{G}_{ch} \cdot \left((1 - q_m) + q_m \cdot \left(\frac{\rho_l}{\rho_g} \right)^{\frac{1}{2}} \right) \tag{4.83}$$

  Then, the equivalent Reynolds number is calculated from Eq. (4.84).

$$\mathrm{Re}_{eq} = \frac{\dot{G}_{eq} \cdot D_h}{\mu_l} \tag{4.84}$$

  The Nusselt number is determined according to the correlation of Lee et al. [93] defined in Eq. (4.85).

$$\mathrm{Nu} = 0.9243 \cdot \mathrm{Re}_{eq}^{0.6151} \cdot \mathrm{Pr}_l^{0.33} \tag{4.85}$$

- Nu-correlation-IV - correlation for refrigerant condensation

  The vapor quality q is calculated at the heat exchanger section inlet and outlet using REFPROP libraries based on refrigerant pressure p^r and inlet and outlet specific enthalpy h_{in} and h_{out}, respectively. The average vapor of the liquid in the section was calculated from Eq. (4.82). The refrigerant density ρ_l, viscosity μ_l, Prandtl number Pr_l and thermal conductivity λ_l in the liquid state are calculated from REFPROP libraries based on quality $q = 0$ and refrigerant pressure p^r and the refrigerant density ρ_g in the gas state based on quality $q = 1$ and refrigerant pressure p^r. The equivalent value of mass flux $\dot{G}_{eq}$ for two-phase flow is defined in Eq. (4.83), where $\dot{G}_{ch}$ is the mass flux per channel defined in Eq. (4.71). Then, the equivalent Reynolds number is calculated from Eq. (4.84).

The Nusselt number is determined according to the correlation of Akers et al. [94] defined in Eq. (4.86).

$$\mathrm{Nu} = 5.03 \cdot \mathrm{Re}_{eq}^{\frac{1}{3}} \cdot \mathrm{Pr}_l^{\frac{1}{3}} \tag{4.86}$$

- Nu-correlation-V - correlation for water forced convection

  The average temperature of the liquid in the heat exchanger section is calculated from Eq. (4.75). The water viscosity μ_f, Prandtl number Pr_f, and thermal conductivity λ_f are calculated from REFPROP libraries based on temperature t_f and water pressure p. Then the Reynolds number is calculated from Eq. (4.76), where $\dot{G}_{ch}$ is the mass flux per channel defined in Eq. (4.71). The Nusselt number is determined according to the correlation of Kwon et al. [95] defined in Eq. (4.87).

$$\mathrm{Nu} = 0.086 \cdot \mathrm{Re}^{0.68} \cdot \mathrm{Pr}_f^{0.333} \tag{4.87}$$

- Nu-correlation-VI - correlation for water-glycol solution

  The average temperature of the liquid in the heat exchanger section is calculated from Eq. (4.75). The water-glycol solution viscosity μ_f, Prandtl number Pr_f and thermal conductivity λ_f are calculated from REFPROP libraries based on temperature t_f and water-glycol solution pressure p. The viscosity for wall temperature μ_w is assumed to be the same as μ_f. Then the Reynolds number is calculated from Eq. (4.76), where $\dot{G}_{ch}$ is the mass flux per channel defined in Eq. (4.71). The Nusselt number is determined according to the correlation of Yang et al. [96] defined in Eq. (4.88), where the coefficient γ is 0.571.

$$\mathrm{Nu} = 0.4139 \cdot \mathrm{Re}^{0.5345} \cdot \mathrm{Re}^{\frac{\phi}{30}} \cdot \mathrm{Re}^{\frac{\gamma}{30}} \cdot \mathrm{Pr}_f^{13} \cdot \left(\frac{\mu_f}{\mu_w}\right)^{0.14} \tag{4.88}$$

Also, the friction factor coefficient f_i was calculated for each heat exchanger section, using the appropriate algorithm selected for each section of the individual heat exchanger of those described below.

- f-correlation-I - correlation for single phase

  The average temperature of the fluid in the section is calculated from Eq. (4.75). The fluid viscosity μ_f is calculated from REFPROP libraries based on temperature t_f and fluid pressure p. Then the Reynolds number is calculated from Eq. (4.76), where $\dot{G}_{ch}$ is the mass flux per channel defined in Eq. (4.71). The friction factor f is determined according to the correlation of Martin et al. [97] defined in Eq.

(4.89), where f_0 and f_1 coefficients are defined in Eq. (4.90) for Re< 2000 and defined in Eq. (4.91) for Re>= 2000 and β is a chevron angle of the heat exchanger plate.

$$f = \left(\left(\frac{\cos\beta}{0.045\cdot\tan\beta + 0.09\cdot\sin\beta + \frac{f_0}{\cos\beta}}\right)^{\frac{1}{2}} + \frac{1-\cos\beta}{\sqrt{3.8\cdot f_1}}\right)^{-0.5} \tag{4.89}$$

if Re< 2000:

$$\begin{cases} f_0 &= \frac{16}{\mathrm{Re}} \\ f_1 &= \frac{149.25}{\mathrm{Re}} + 0.9625 \end{cases} \tag{4.90}$$

if Re>= 2000:

$$\begin{cases} f_0 &= (1.56\cdot\ln\mathrm{Re} - 3)^{-2} \\ f_1 &= \frac{9.75}{\mathrm{Re}^{0.289}} \end{cases} \tag{4.91}$$

- f-correlation-II - correlation for evaporating refrigerant

  The vapor quality q is calculated at the heat exchanger section inlet and outlet using REFPROP libraries based on refrigerant pressure p^r and inlet and outlet specific enthalpy h_{in} and h_{out}, respectively. The average vapor of the liquid in the section was calculated from Eq. (4.82). The refrigerant density ρ_l, viscosity μ_l, and Prandtl number Pr_l in the liquid state are calculated from REFPROP libraries based on quality $q = 0$ and refrigerant pressure p^r. The refrigerant density ρ_g in the gas state is calculated based on quality $q = 1$ and refrigerant pressure p^r. The equivalent value of mass flux $\dot{G}_{eq}$ for two-phase flow is defined in Eq. (4.83), where $\dot{G}_{ch}$ is the mass flux per channel defined in Eq. (4.71). Then the equivalent Reynolds number Re_{eq} is calculated from Eq. (4.84), where D_h is a hydraulic diameter defined in Eq. (4.66). The Reynolds number for liquid refrigerant in the saturated state Re_{l0} is calculated from Eq. (4.92).

$$\mathrm{Re}_{l0} = \frac{\dot{G}_{ch}\cdot D_h}{\mu_l} \tag{4.92}$$

  The friction factor f is determined according to the correlation of Lee et al. [93] defined in Eq. (4.93).

$$f = 6.25\cdot 10^{-4}\cdot \mathrm{Re}_{eq}^{1.427}\cdot \mathrm{Re}_{l0}^{-0.7098}\cdot \mathrm{Pr}_l^{0.4036} \tag{4.93}$$

- f-correlation-III - correlation for condensing refrigerant

  The vapor quality q is calculated at the heat exchanger section inlet and outlet using REFPROP libraries based on refrigerant pressure p^r and inlet and outlet specific enthalpy h_{in} and h_{out}, respectively. The average vapor of the liquid in the section was calculated from Eq. (4.82). The refrigerant density ρ_l, viscosity μ_l, and Prandtl number Pr_l in the liquid state are calculated from REFPROP libraries based on quality $q = 0$ and refrigerant pressure p^r. The refrigerant density ρ_g in the gas state is calculated based on quality $q = 1$ and refrigerant pressure p^r. The equivalent value of mass flux $\dot{G}_{eq}$ for two-phase flow is defined in Eq. (4.83), where $\dot{G}_{ch}$ is the mass flux per channel defined in Eq. (4.71). Then the equivalent Reynolds number Re_{eq} is calculated from Eq. (4.84), where D_h is a hydraulic diameter defined in Eq. (4.66). The Reynolds number for liquid refrigerant in the saturated state Re_{l0} is calculated from Eq. (4.92).

The friction factor f is determined according to the correlation of Kwon et al. [95] defined in Eq. (4.94), where Ge is a geometric parameter calculated from Eq. (4.95).

$$f = 2367.31 \cdot Re_{eq}^{-0.543} \cdot Re_{l0}^{-0.517} \cdot Ge^{0.177} \tag{4.94}$$

$$Ge = \frac{\beta}{180} \cdot \pi \tag{4.95}$$

Then, the overall heat transfer coefficient $OHTC_i$ was calculated for each heat exchanger section according to Eq. (4.96), where i indicates the heat exchanger Section a-b, b-c, or c-d.

$$OHTC_i = \frac{1}{\frac{1}{\alpha_i^{hot}} + \frac{\delta}{k_w} + \frac{1}{\alpha_i^{cold}} + R_f} \tag{4.96}$$

The logarithmic mean temperature difference $\Delta T_{lm,i}$ is calculated for each section of heat exchanger from Eq. (4.97).

$$\Delta T_{lm,i} = \frac{\Delta T_1 - \Delta T_2}{ln(\Delta T_1 / \Delta T_2)} \tag{4.97}$$

The heat transfer rate transferred by the hot fluid and absorbed by the cold fluid for each heat exchanger section i was calculated according to Eqs (4.98) and (4.99).

$$\dot{Q}_i^{hot} = \dot{m}^{hot} \cdot (h_1^{hot} - h_2^{hot}) \tag{4.98}$$

$$\dot{Q}_i^{cold} = \dot{m}^{cold} \cdot (h_2^{cold} - h_1^{cold}) \tag{4.99}$$

The heat transfer area of the heat exchanger section is calculated from Eq. (4.100), where $\dot{Q}_i$ is the greater of $\dot{Q}_i^{hot}$ or $\dot{Q}_i^{cold}$ calculated.

$$A_i = \frac{\dot{Q}_i}{OHTC_i \cdot \Delta T_{lm,i}} \tag{4.100}$$

Then, the frictional pressure drops on each heat exchanger section hot and cold sides are calculated from Eq. (4.101), where $\rho_{avg,i}$ is the arithmetic mean of the inlet and outlet values of the density of a given fluid to a given section of the heat exchanger.

$$\Delta P_{f,i} = \frac{2 \cdot f_i \cdot L_p}{D_h} \cdot \frac{\dot{G}_{ch}^2}{\rho_{avg,i}} \cdot N_p \tag{4.101}$$

The frictional pressure drop is then summed for the cold and hot sides of the whole heat exchanger ΔP_f^{cold}, ΔP_f^{hot} according to Eq. (4.102).

$$\Delta P_f = \Delta P_{f,a-b} + \Delta P_{f,b-c} + \Delta P_{f,c-d} \tag{4.102}$$

The pressure drop in heat exchanger ports for the cold and hot sides of the heat exchanger is calculated from Eq. (4.103).

$$\Delta P_{p,i} = \frac{1.5 \cdot N_p \cdot \dot{G}_i^2}{2 \cdot \rho_{avg,i}} \tag{4.103}$$

The total pressure drop in the heat exchanger on the cold and hot sides is calculated as the sum of the frictional pressure drop and the pressure drop at the heat exchanger stubs from Eq. (4.104).

$$\Delta P_i = \Delta P_{p,i} + \Delta P_{f,i} \tag{4.104}$$

The logarithmic mean temperature difference ΔT_{lm} for the whole heat exchanger is the heat transfer rate-weighted average defined in Eq. (4.105).

$$\Delta T_{lm} = \frac{\Delta T_{lm,a-b} \cdot \dot{Q}_{a-b} + \Delta T_{lm,b-c} \cdot \dot{Q}_{b-c} + \Delta T_{lm,c-d} \cdot \dot{Q}_{c-d}}{\dot{Q}_{a-b} + \dot{Q}_{b-c} + \dot{Q}_{c-d}} \tag{4.105}$$

The overall heat transfer coefficient $OHTC$ for the whole heat exchanger is the heat transfer area-weighted average calculated according to Eq.4.106.

$$OHTC = \frac{OHTC_{a-b} \cdot A_{a-b} + OHTC_{b-c} \cdot A_{b-c} + OHTC_{c-d} \cdot A_{c-d}}{A_{a-b} + A_{b-c} + A_{c-d}} \tag{4.106}$$

In HXD, the total heat transfer area is calculated in two ways. Firstly, the A' value is calculated from Eq. (4.107) as a sum of the heat transfer area of each heat exchanger section.

$$A' = A_{a-b} + A_{b-c} + A_{c-d} \tag{4.107}$$

Secondly, the total heat transfer area is calculated using logarithmic mean temperature difference from Eq. (4.108)

$$A" = \frac{\dot{Q}_{a-b} + \dot{Q}_{b-c} + \dot{Q}_{c-d}}{OHTC \cdot \Delta T_{lm}} \tag{4.108}$$

The final design heat transfer area A is the larger of the calculated areas A' and $A"$. This approach results from the HXD mode assumption that any oversizing of the heat exchanger surface area is safer than choosing a heat transfer area that is too small. The number of heat exchanger plates N_t is then calculated from Eq. (4.109).

$$N_t = \frac{A}{A_t} \tag{4.109}$$

In HXD mode, calculations are repeated as long as assumed N_t converges its calculated value.

In HXA, the total heat transfer area is an input value. The total heat transfer rate of the heat exchanger is calculated according to Eq. (4.110).

$$\dot{Q} = A \cdot OHTC \cdot \Delta T_{lm} \tag{4.110}$$

The heat transfer rates given off by the hot fluid and absorbed by the cold fluid are calculated according to Eqs (4.111) and (4.112).

$$\dot{Q}^{hot} = \dot{m}^{hot} \cdot (h_{in}^{hot} - h_{out}^{hot}) \tag{4.111}$$

$$\dot{Q}^{cold} = \dot{m}^{cold} \cdot (h_{out}^{cold} - h_{in}^{cold}) \tag{4.112}$$

In HXA, the outlet parameters (temperatures or specific enthalpies) of the hot and cold fluids are iterated until the conditions expressed by Eqs (4.113) and (4.114) are met.

$$\dot{Q} - \dot{Q}^{hot} \approx 0 \tag{4.113}$$

$$\dot{Q} - \dot{Q}^{cold} \approx 0 \tag{4.114}$$

Additionally, in HXA, after recalculating the area of each section of the heat exchanger A_i according to Eq. (4.100), a condition expressed by Eq. (4.115) is checked if the sum of the sections recalculated so far ($\sum_{i=1}^{n} A_i$) is less than or equal to the known area of the entire heat exchanger (A).

$$\sum_{i=1}^{n} A_i \le A \tag{4.115}$$

If the condition (4.115) is not fulfilled, then the following heat exchanger sections are excluded, and the last recalculated heat exchanger section A_{i+1} has a known area resulting from the remaining available heat exchanger area calculated according to Eq. (4.116).

$$A_{i+1} = A - \sum_{i=1}^{n} A_i \tag{4.116}$$

4.2.1 Generator

As mentioned, mathematical modeling of the generator to model the entire refrigeration system includes using a simple model for preliminary calculations and an LMTD model for detailed heat exchanger selection.

Simple model

In HXD, a simple generator model calculates the generator refrigerant pressure p^r_{gen} based on the assumptions made. The characteristic sections of the generator responsible for heating (a-b), evaporation (b-c), and superheating (c-d) of the refrigerant are indicated in Fig. 4.5, where the simplified temperature diagram in a function of heat transfer rate was presented. The model requires the following input values: refrigerant temperature at point a $t^r_{a,gen} = t_8$, hot water temperatures at the inlet and outlet of the heat exchanger $t^{hw}_{d,gen} = t_{hw1}$, $t^{hw}_{a,gen} = t_{hw2}$, hot water mass flow rate $\dot{m}^{hw}_{gen}$, hot water pressure p^{hw}_{gen}, assumed pinch point temperature difference $\Delta T^{hyp}_{pp,gen}$, assumed superheating of refrigerant $\Delta T_{sh,gen}$. The state points corresponding to the above parameters with the given subscripts 8, hw1, and hw2 can be seen in Fig. 4.1.

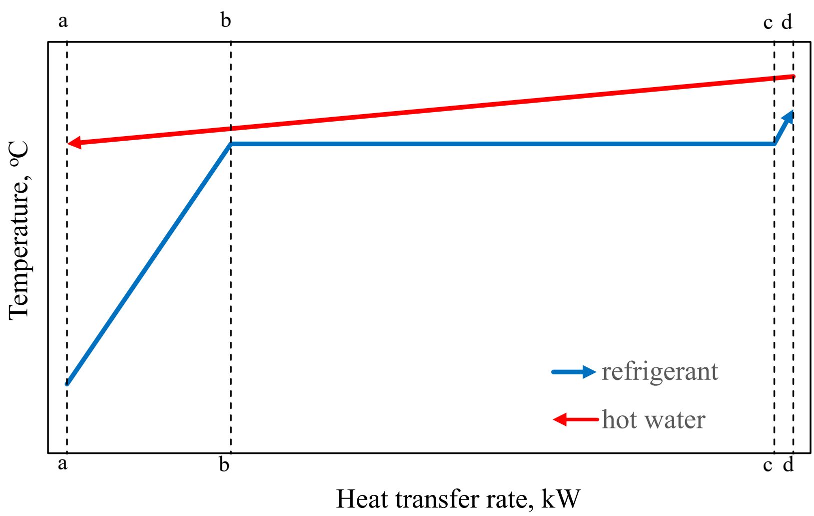

FIGURE 4.5: Generator temperature distribution

The saturation pressure in the generator is an iterated quantity in the interval determined by the inlet and outlet temperatures of the hot water to the generator as defined in Eq. (4.117)

$$p^r_{gen} \in \left(p^r_{sat}(t^{hw}_{d,gen}), p^r_{sat}(t^{hw}_{a,gen})\right) \tag{4.117}$$

The refrigerant temperature at point d is calculated from Eq. (4.118).

$$t^r_{d,gen} = t^r_{sat,gen} + \Delta T_{sh,gen} \tag{4.118}$$

where the $\Delta T_{sh,gen}$ is assumed superheating of refrigerant in the generator.

Using REFPROP libraries, the specific enthalpy of refrigerant is calculated for assumed saturation pressure at the ends of characteristic sections of the generator according to Eqs (4.119) to (4.122).

$$h^r_{a,gen} = h\left(t^r_{a,gen}, p^r_{gen}\right) \tag{4.119}$$

$$h^r_{b,gen} = h\left(q = 0, p^r_{gen}\right) \tag{4.120}$$

$$h^r_{c,gen} = h\left(q = 1, p^r_{gen}\right) \tag{4.121}$$

$$h^r_{d,gen} = h\left(t^r_{d,gen}, p^r_{gen}\right) \tag{4.122}$$

The specific enthalpy for the inlet and outlet on the hot water side ($h^{hw}_{d,gen}$ and $h^{hw}_{a,gen}$) is also read based on the temperature and pressure. The energy conservation equation on the hot water side of the generator is used to calculate the total heat transfer rate received from the waste heat source according to Eq. (4.123).

$$\dot{Q}^{hw}_{a-d,gen} = \dot{m}^{hw}_{gen} \cdot \left(h^{hw}_{d,gen} - h^{hw}_{a,gen}\right) \tag{4.123}$$

The refrigerant mass flow rate is calculated according to Eq. (4.124).

$$\dot{m}^r_{gen} = \frac{\dot{Q}^{hw}_{a-d,gen}}{\left(h^r_{d,gen} - h^r_{a,gen}\right)} \tag{4.124}$$

The energy conservation equations are used to calculate the heat transfer rate for each generator section on the refrigerant side, according to Eqs (4.125) to (4.127).

$$\dot{Q}^r_{a-b,gen} = \dot{m}^r_{gen} \cdot \left(h^r_{b,gen} - h^r_{a,gen}\right) \tag{4.125}$$

$$\dot{Q}^r_{b-c,gen} = \dot{m}^r_{gen} \cdot \left(h^r_{c,gen} - h^r_{b,gen}\right) \tag{4.126}$$

$$\dot{Q}^r_{c-d,gen} = \dot{m}^r_{gen} \cdot \left(h^r_{d,gen} - h^r_{c,gen}\right) \tag{4.127}$$

The above equations are covered by logical conditions that allow the heat transfer rate in individual sections of the heat exchanger to be reset in case of insufficient waste heat transfer rate. The specific enthalpy of the hot water at points b and c are estimated using the following energy conservation equations (Eqs (4.128) and (4.129)).

$$h^{hw}_{b,gen} = h^{hw}_{a,gen} + \frac{\dot{Q}^r_{a-b,gen}}{\dot{m}^{hw}_{gen}} \tag{4.128}$$

$$h^{hw}_{c,gen} = h^{hw}_{d,gen} - \frac{\dot{Q}^r_{c-d,gen}}{\dot{m}^{hw}_{gen}} \tag{4.129}$$

The temperature of hot water at points b and c $t^{hw}_{b,gen}$, $t^{hw}_{c,gen}$ of the generator is read from the REFPROP libraries based on calculated specific enthalpies and hot water pressure. Finally, the pinch point temperature difference is calculated from Eq. (4.130).

$$\Delta T_{pp,gen} = t^{hw}_{b,gen} - t^r_{b,gen} \tag{4.130}$$

The saturation pressure of the refrigerant in the generator p^r_{gen} is iterated until the calculated value of the pinch point temperature difference $\Delta T_{pp,gen}$ reaches the assumed value $\Delta T^{hyp}_{pp,gen}$ with 1e-8 tolerance for calculation termination.

LMTD model

In the LMTD model described earlier for the general case of a heat exchanger, the parameters at state points a, b, c, and d must be assigned for further calculations. In the case of a generator, there are several options to consider. All of them are shown in Fig. 4.6. In HXD, there are two alternatives: Option I, where there is a single heat exchanger to receive waste heat, where the refrigerant is to be preheated (a-b), evaporated (b-c), and superheated (c-d), and Option IV, where there is a separate preheater, and the generator is only to evaporate (b-c) and superheat (c-d) the refrigerant. In the HXA, three additional options result from insufficient heat exchange surface. Option II and III are alternatives to Option I, a single heat exchanger receiving waste heat. In Option II, the heat exchanger surface area is insufficient to completely vaporize and superheat the refrigerant. In Option III, the surface area is insufficient to heat the refrigerant to saturation parameters. Option V is an alternative to Option IV, where the refrigerant at the inlet to the heat exchanger is a saturated liquid. Still, the generator area is too small for complete evaporation and superheating.

For the various options considered, the temperature and specific enthalpy were respectively assigned to each state point (a, b, c, d) as follows:

- Option I:

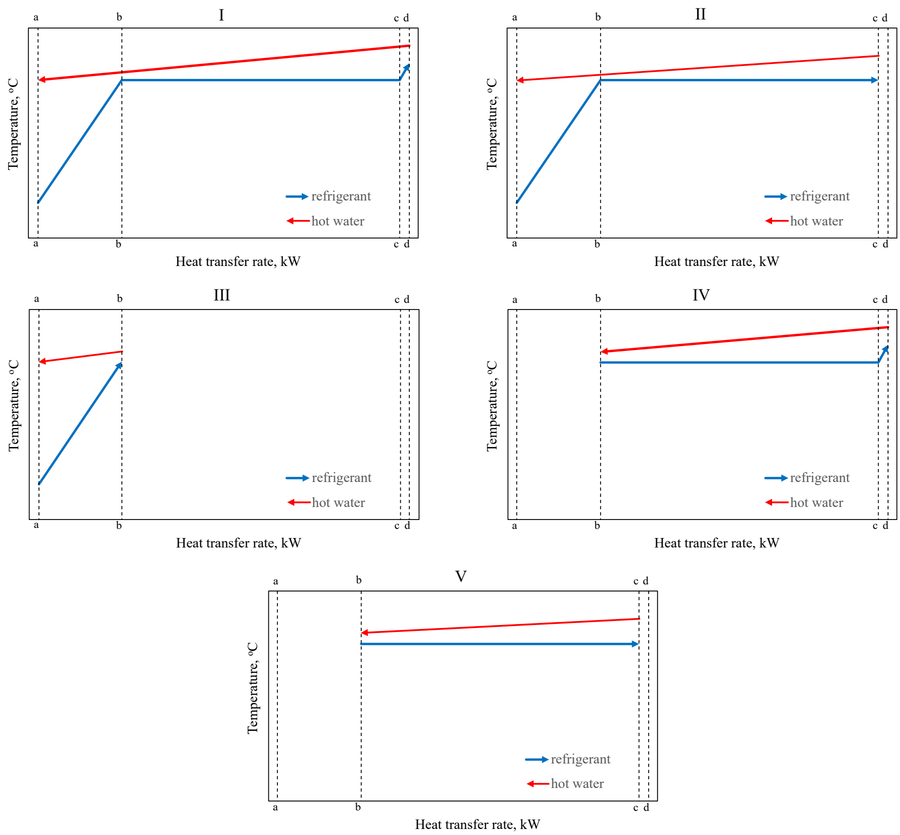

FIGURE 4.6: Generator temperature distributions in options: I - preheating, evaporation, and superheating of the refrigerant, II - preheating and incomplete evaporation of the refrigerant, III - preheating without reaching a saturated state of the refrigerant, IV - evaporation and superheating of the refrigerant, V - incomplete evaporation of the refrigerant

- t_a^{hot}, t_d^{cold} - assumed outlet variables
- t_d^{hot}, t_a^{cold} - input variables
- t_b^{cold}, t_c^{cold} - saturation temperature $(t_{sat}(p_{gen}^r))$
- t_b^{hot}, t_c^{hot} - $t = f(p_{gen}^{hw}, h_i^{hot})$ calculated based on p and h
- h_a^{cold}, h_d^{cold} - $h = f(p_{gen}^r, t_i^{cold})$ calculated based on p and t
- h_b^{cold}, h_c^{cold} - $h = f(p_{gen}^r, q)$ calculated based on p and $q = 0$ or $q = 1$, at point b and c, respectively
- h_a^{hot}, h_d^{hot} - $h = f(p_{gen}^{hw}, t_i^{hot})$ calculated based on p and t

- h_b^{hot}, h_c^{hot} - calculated based on energy conservation equations (Eqs (4.131) and (4.132))

$$h_b^{hot} = h_a^{hot} + \dot{m}_{gen}^{cold} \cdot \frac{h_b^{cold} - h_a^{cold}}{\dot{m}_{gen}^{hot}} \tag{4.131}$$

$$h_c^{hot} = h_b^{hot} + \dot{m}_{gen}^{cold} \cdot \frac{h_c^{cold} - h_b^{cold}}{\dot{m}_{gen}^{hot}} \tag{4.132}$$

- Option II:
  - t_a^{hot}, h_c^{cold} - assumed outlet variables
  - t_c^{hot}, t_a^{cold} - input variables
  - t_b^{cold}, t_c^{cold} - saturation temperature ($t_{sat}(p_{gen}^r)$)
  - t_b^{hot} - $t = f(p_{gen}^{hw}, h_b^{hot})$ calculated based on p and h
  - h_a^{cold} - $h = f(p_{gen}^r, t_a^{cold})$ calculated based on p and t
  - h_b^{cold}, - $h_b^{cold} = f(p_{gen}^r, q = 0)$ calculated based on p and $q = 0$
  - h_a^{hot}, h_c^{hot} - $h = f(p_{gen}^{hw}, t_i^{hot})$ calculated based on p and t
  - h_b^{hot} - calculated based on energy conservation equations (Eq. (4.131))
- Option III:
  - t_a^{hot}, t_b^{cold} - assumed outlet variables
  - t_b^{hot}, t_a^{cold} - input variables
  - h_a^{cold}, h_b^{cold} - $h = f(p_{gen}^r, t_i^{cold})$ calculated based on p and t
  - h_a^{hot}, h_b^{hot} - $h = f(p_{gen}^{hw}, t_i^{hot})$ calculated based on p and t
- Option IV:
  - t_b^{hot}, t_d^{cold} - assumed outlet variables
  - t_d^{hot}, h_b^{cold} - input variables
  - t_b^{cold}, t_c^{cold} - saturation temperature ($t_{sat}(p_{gen}^r)$)
  - t_c^{hot} - $t = f(p_{gen}^{hw}, h_c^{hot})$ calculated based on p and h
  - h_d^{cold} - $h = f(p_{gen}^r, t_d^{cold})$ calculated based on p and t
  - h_c^{cold} - $h = f(p_{gen}^r, q = 1)$ calculated based on p and $q = 1$
  - h_b^{hot}, h_d^{hot} - $h = f(p_{gen}^{hw}, t_i^{hot})$ calculated based on p and t
  - h_c^{hot} - calculated based on energy conservation equation (Eq. (4.132))

- Option V:
  - t_b^{hot}, h_c^{cold} - assumed outlet variables
  - t_c^{hot}, h_b^{cold} - input variables
  - t_b^{cold}, t_c^{cold} - saturation temperature ($t_{sat}(p^r_{gen})$)
  - h_b^{hot}, h_c^{hot} - $h = f(p^{hw}_{gen}, t_i^{hot})$ calculated based on p and t

As mentioned earlier, the convective heat transfer coefficient α and friction factor f were determined in the LMTD model to calculate the total heat transfer coefficient and pressure loss for each heat exchanger section. The following algorithms, described in Section 4.2, were used to calculate the Nusselt number and friction factor in each section:

- Section a-b

  To calculate the Nusselt number for cold fluid Nu^{cold}_{a-b}, i.e., the refrigerant in a liquid phase, the Nu-correlation-I described by Eq. (4.77) was used. In the case of hot fluid, i.e., hot water, the Nu-correlation-V, described by Eq. (4.87), was used to calculate Nu^{hot}_{a-b}. For both fluids, the friction factor f_{a-b} was computed using the f-correlation-I, described by Eq. (4.89).

- Section b-c

  For Section b-c, where refrigerant evaporation takes place, the values of Nusselt Number Nu^{hot}_{b-c} and friction factor f^{hot}_{b-c} for hot water were calculated according to the same algorithms as for Section a-b. For the evaporating cold fluid, that is, for the refrigerant, the Nu-correlation-III described by Eq. (4.85) was used to calculate the Nusselt number Nu^{cold}_{b-c}. The f-correlation-II described by Eq. (4.93) was used to calculate the friction factor f^{cold}_{b-c}.

- Section c-d

  Finally, for sections c-d, where superheating of the refrigerant vapor occurs, the same correlations for hot water as in earlier sections of the generator were again used to calculate Nu^{hot}_{c-d} and f^{hot}_{c-d}. For the refrigerant vapor on the cold side of the generator, the Nu-correlation-II described by Eq. (4.81) was used to calculate the Nusselt number Nu^{cold}_{c-d} and similarly as in Section a-b f-correlation-I, described by Eq. (4.89) to calculate the friction factor f^{cold}_{c-d}.

The final result of the generator calculation using the LMTD model is primarily the temperature distribution in the heat exchanger. In HXD, the information about the number of generator plates $N_{t,gen}$ and about the pressure drops on both sides of the heat exchanger ΔP^r_{gen} and ΔP^{hw}_{gen} is received. In HXA, the outlet temperatures from the generator t_1, t_{hw2} and the pressure drops are the output values, so it is possible to assess the correctness of the heat exchanger selection or compare heat exchangers with different geometries.

4.2.2 Preheater

Since it is unnecessary to calculate the pressure in the preheater due to the assumption of the same pressure level as in the generator p^r_{gen}, the preheater does not have a simplified calculation model. In addition, the simplified generator model assumes a single heat exchanger for preheating, evaporation, and superheating of the refrigerant. Thus, the calculations for the potential preheater are included in the simple generator model. The preheater model is needed only to analyze the validity of the separation of heat exchangers receiving waste heat.

LMTD model

The preheater LMTD model covers only one considered case of a heat exchanger. The temperature distribution in the heat exchanger is shown in Fig. 4.7. The preheater has only one section, where the target is to heat the refrigerant to saturation temperature and cool the hot water.

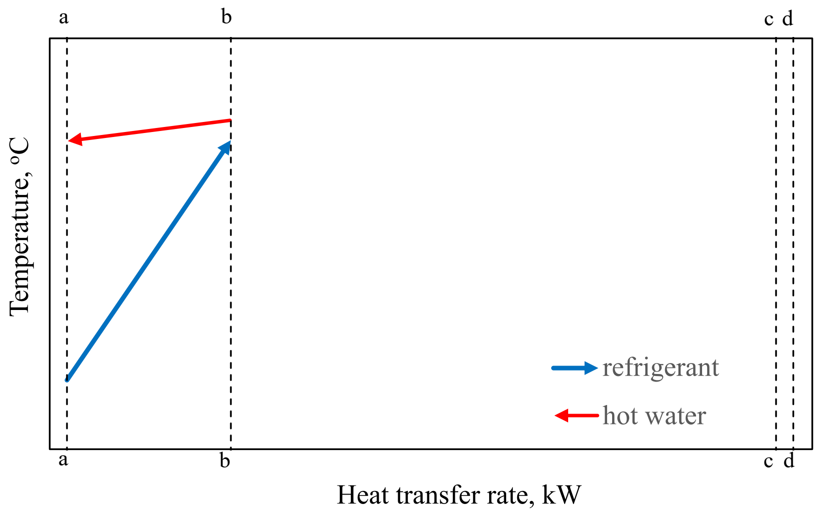

FIGURE 4.7: Preheater temperature distribution

To calculate the heat exchanger in the LMTD model, parameters, i.e., temperatures and specific enthalpy in a and b, must be assigned before calculating the overall heat transfer coefficient and pressure drop. In this case, it is implemented as follows:

- t_a^{hot}, h_b^{cold} - assumed outlet variables
- t_b^{hot}, t_a^{cold} - input variables
- h_a^{cold}, h_b^{cold} - $h = f(p^r_{gen}, t_i^{cold})$ calculated based on p and t

- h_a^{hot}, h_b^{hot} - $h = f(p_{gen}^{hw}, t_i^{hot})$ calculated based on p and t

The following algorithms, described in Chapter 4.2, were used to calculate the Nusselt number and friction factor in preheater:

- Section a-b

  To calculate the Nusselt number for cold fluid Nu_{a-b}^{cold}, i.e., the refrigerant in a liquid phase, the Nu-correlation-I described by Eq. (4.77) was used. In the case of hot fluid, i.e., hot water, the Nu-correlation-V, described by Eq. (4.87), was used to calculate Nu_{a-b}^{hot}. For both fluids, the friction factor f_{a-b} was computed using the f-correlation-I, described by Eq. (4.89).

The final result of the preheater calculation using the LMTD model depends on the calculation mode. In HXD, the information about the number of preheater plates $N_{t,preh}$ and about the pressure drops on both sides of the heat exchanger ΔP_{preh}^{cold} and ΔP_{preh}^{hot} is obtained. In HXA, the preheater outlet temperatures $t_{out,preh}^{hot}$, $t_{out,preh}^{cold}$, and the pressure drops are calculated.

4.2.3 Evaporator

The mathematical modeling of the evaporator involves using a simple model for preliminary calculations and an LMTD model for detailed heat exchanger selection.

Simple model

In HXD, a simple evaporator model calculates the refrigerant saturation pressure p_{evap}^r based on the assumptions made. The characteristic sections of the evaporator responsible for evaporation (b-c) and superheating (c-d) of the refrigerant are indicated in Fig. 4.8, where the simplified temperature diagram in a function of heat transfer rate was presented along the heat exchanger. The model necessitates the following input parameters: refrigerant specific enthalpy at point b $h_{b,evap}^r$, glycol-water solution temperature at the outlet of the heat exchanger $t_{b,evap}^{gl}$, glycol-water solution temperature at the inlet of the heat exchanger $t_{d,evap}^{gl}$, hot water mass flow rate - $\dot{m}_{gen}^{hw}$, glycol-water solution pressure - p_{evap}^{gl}, assumed pinch point temperature difference - $\Delta T_{pp,evap}^{hyp}$, assumed superheating of refrigerant - $\Delta T_{sh,evap}$ and the refrigerant mass flow rate $\dot{m}_{evap}^r$, which is equal to $\dot{m}_{sn}$, calculated in ejector model.

The evaporator saturation pressure p_{evap}^r is an iterated quantity in the interval determined by the inlet and reduced outlet temperatures of the glycol-water solution as defined in Eq. (4.133)

$$p_{evap}^r \in \left(p_{sat}^r(t_{d,evap}^{gl}), p_{sat}^r(t_{b,evap}^{gl} - 10\mathrm{K})\right) \tag{4.133}$$

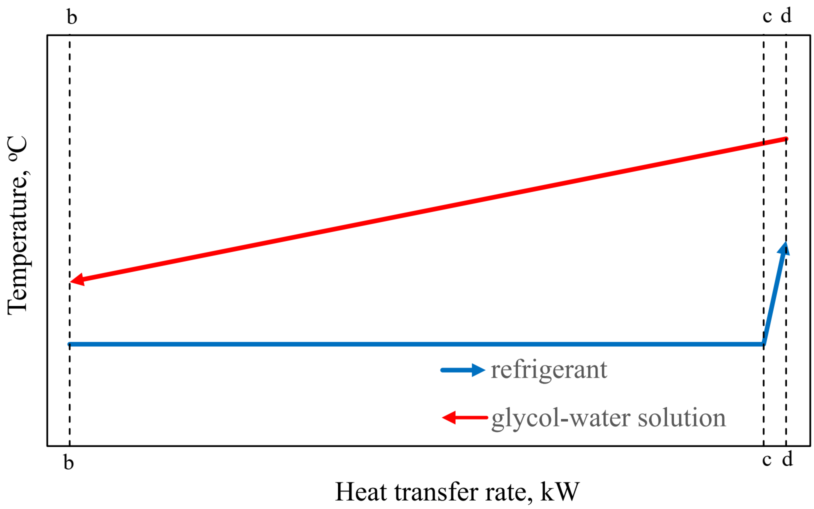

FIGURE 4.8: Evaporator temperature distribution

The refrigerant saturation temperature $t^r_{sat,evap}$, thus the temperature at state points b and c ($t^r_{b,evap}$ and $t^r_{c,evap}$) is determined using REFPROP libraries based on p^r_{evap}. The refrigerant temperature at point d is calculated from Eq. (4.134).

$$t^r_{d,evap} = t^r_{sat,evap} + \Delta T_{sh,evap} \tag{4.134}$$

where $\Delta T_{sh,evap}$ is assumed superheating of refrigerant at the evaporator outlet.

The specific enthalpy of the refrigerant at points c and d and of glycol-water solution at points b and d is read from REFPROP libraries, according to Eqs (4.135) to (4.138).

$$h^r_{c,evap} = h\left(q = 1, p^r_{evap}\right) \tag{4.135}$$

$$h^r_{d,evap} = h\left(t^r_{d,evap}, p^r_{evap}\right) \tag{4.136}$$

$$h^{gl}_{b,evap} = h\left(t^{gl}_{b,evap}, p^{gl}_{evap}\right) \tag{4.137}$$

$$h^{gl}_{d,evap} = h\left(t^{gl}_{d,evap}, p^{gl}_{evap}\right) \tag{4.138}$$

The energy conservation equation is used to calculate the heat transfer rate absorbed by the refrigerant during evaporation $\dot{Q}^r_{b-c,evap}$ and vapor superheating $\dot{Q}^r_{c-d,evap}$ according to Eqs (4.139) and (4.140).

$$\dot{Q}^r_{b-c,evap} = \dot{m}^r_{evap} \cdot \left(h^r_{c,evap} - h^r_{b,evap}\right) \tag{4.139}$$

$$\dot{Q}^{r}_{c-d,evap} = \dot{m}^{r}_{evap} \cdot \left(h^{r}_{d,evap} - h^{r}_{c,evap} \right) \tag{4.140}$$

The total heat transfer rate absorbed by refrigerant $\dot{Q}^{r}_{evap}$ is a sum of $\dot{Q}^{r}_{b-c,evap}$ and $\dot{Q}^{r}_{c-d,evap}$. It is assumed that the same heat transfer rate is collected from the glycol-water solution, thus $\dot{Q}^{gl}_{evap} = \dot{Q}^{r}_{evap}$. The mass flow rate of the glycol-water solution $\dot{m}^{gl}_{evap}$, which is possible to cool down to the assumed outlet temperature, is calculated from Eq. (4.141).

$$\dot{m}^{gl}_{evap} = \frac{\dot{Q}^{gl}_{evap}}{h^{gl}_{d,evap} - h^{gl}_{b,evap}} \tag{4.141}$$

The specific enthalpy of the glycol-water solution at point c $h^{gl}_{c,evap}$ is estimated using the following energy conservation equation (Eq. (4.142))

$$h^{gl}_{c,evap} = h^{gl}_{b,evap} + \frac{\dot{Q}^{r}_{b-c,evap}}{\dot{m}^{gl}_{evap}} \tag{4.142}$$

The temperature of the glycol-water solution at point c $t^{gl}_{c,evap}$ is read from the REFPROP libraries based on calculated specific enthalpy and the glycol-water solution pressure. The pinch point temperature difference is calculated from Eq. (4.143).

$$\Delta T_{pp,evap} = t^{gl}_{b,evap} - t^{r}_{b,evap} \tag{4.143}$$

The saturation pressure of the refrigerant in the evaporator p^{r}_{evap} is iterated until the calculated value of the pinch point temperature difference $\Delta T_{pp,evap}$ reaches the assumed value $\Delta T^{hyp}_{pp,evap}$, with 1e-8 tolerance for calculation termination.

LMTD model

The specific enthalpies and temperatures at evaporator state points a, b, and c are assigned to calculate the heat exchanger key parameters. In the case of the evaporator, there are two options to consider, which are shown in Fig. 4.9, where two temperature distribution lines are presented. In HXD, only Option I is considered, where the refrigerant enters the heat exchanger in a two-phase state, evaporates (b-c), and is superheated (c-d), which causes cooling of the glycol-water solution. In HXA, apart from considering Option I, Option II is also considered. In Option II, the heat exchanger is too small to fully evaporate and superheat the refrigerant. Thus, only section (b-c) is calculated.

For the two options considered, the temperature and specific enthalpy were respectively assigned to each state point (b, c, d) as follows:

- Option I:

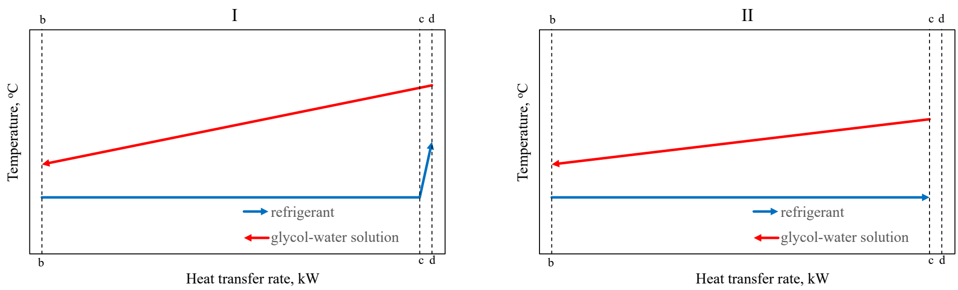

FIGURE 4.9: Evaporator temperature distribution in options: I - evaporation and superheating of the refrigerant, II - incomplete evaporation of the refrigerant

- t_b^{hot}, t_d^{cold} - assumed outlet variables
- t_d^{hot}, h_b^{cold} - input variables
- t_b^{cold}, t_c^{cold} - saturation temperature ($t_{sat}(p_{evap}^r)$)
- t_c^{hot} - $t = f(p_{evap}^{gl}, h_c^{hot})$ calculated based on p and h
- h_d^{cold} - $h = f(p_{evap}^r, t_d^{cold})$ calculated based on p and t
- h_c^{cold} - $h = f(p_{evap}^r, q = 1)$ calculated based on p and $q = 1$
- h_b^{hot}, h_d^{hot} - $h = f(p_{evap}^{gl}, t_i^{hot})$ calculated based on p and t
- h_c^{hot} - calculated based on energy conservation equation (Eq. (4.144))

$$h_c^{hot} = h_b^{hot} + \dot{m}_{evap}^{cold} \cdot \frac{h_c^{cold} - h_b^{cold}}{\dot{m}_{evap}^{hot}} \tag{4.144}$$

- Option II:
  - t_b^{hot}, h_c^{cold} - assumed outlet variables
  - t_c^{hot}, h_b^{cold} - input variables
  - t_b^{cold}, t_c^{cold} - saturation temperature ($t_{sat}(p_{evap}^r)$)
  - h_b^{hot}, h_c^{hot} - $h = f(p_{evap}^{gl}, t_i^{hot})$ calculated based on p and t

The convective heat transfer coefficient (α) and friction factor (f) were identified using the LMTD model to compute the overall heat transfer coefficient and pressure drop for each heat exchanger segment. The algorithms outlined in Section 4.2 were employed to determine the Nusselt number and friction factor for each segment.

- Section b-c

  For Section b-c, where refrigerant evaporation takes place, the Nu-correlation-III described by Eq. (4.85) was used to calculate the Nusselt number Nu_{b-c}^{cold}. The f-correlation-II described by Eq. (4.93) was used to calculate the friction factor f_{b-c}^{cold}. On the hot side of the heat exchanger, the value of Nusselt Number Nu_{b-c}^{hot} was calculated using the correlation for glycol-water solution (Nu-correlation-VI) described by Eq. (4.88). The friction on that side f_{b-c}^{hot} was estimated according to the f-correlation-I described by Eq. (4.89).

- Section c-d

  For Section c-d, where superheating of the refrigerant vapor takes place, the same correlations for glycol-water as in the previous section were again used to calculate Nu_{c-d}^{hot} and f_{c-d}^{hot}. On the refrigerant side of the evaporator, the Nu-correlation-II algorithm described by Eq. (4.81) was used to calculate the Nusselt number Nu_{c-d}^{cold} and the f-correlation-I, described by Eq. (4.89) to calculate the friction factor f_{c-d}^{cold}.

The outcome of the evaporator calculation utilizing the LMTD model is the temperature distribution within the heat exchanger. Depending on the calculation mode employed, in HXD, one obtains information regarding the number of evaporator plates ($N_{t,evap}$) and the pressure drops on both sides of the heat exchanger (ΔP_{evap}^{cold} and ΔP_{evap}^{hot}). In the HXA, the outlet temperatures from the evaporator ($t_{out,evap}^{hot}$ and $t_{out,evap}^{cold}$), as well as the pressure drops, are determined. This enables the assessment of the appropriateness of the heat exchanger selection or the comparison of heat exchangers with varying geometries.

4.2.4 Condenser

As mentioned, mathematical modeling of the generator to model the entire refrigeration system includes using a simple model for preliminary calculations and an LMTD model for detailed heat exchanger selection.

Simple model

In HXD, a simple condenser model determines the refrigerant pressure p_{cond}^{r}. The condenser key sections responsible for desuperheating (c-d), condensation (b-c), and subcooling (a-b) of the refrigerant are shown in Fig. 4.10, which presents a simplified temperature diagram as a function of heat transfer rate. The model requires the following input values: the refrigerant specific enthalpy at point d ($h_{d,cond}^{r}$), cold water temperatures at the heat exchanger inlet and outlet ($t_{a,cond}^{cw}$ and $t_{d,cond}^{cw}$), refrigerant mass flow rate ($\dot{m}_{cond}^{r}$), cold water pressure (p_{cond}^{cw}), assumed pinch point temperature difference ($\Delta T_{pp,cond}^{hyp}$), and the assumed refrigerant subcooling ($\Delta T_{sc,cond}$).

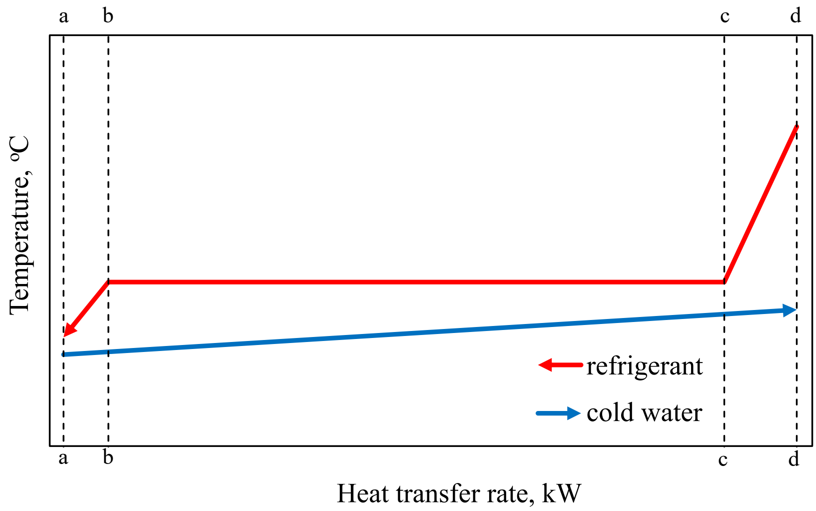

FIGURE 4.10: Condenser temperature distribution

The saturation pressure in the condenser is an iterated quantity in the interval determined by the saturation pressure in the evaporator and the generator as defined in Eq. (4.145)

$$p^r_{cond} \in \left(p^r_{evap}, p^r_{gen}\right) \tag{4.145}$$

The saturation temperature in the condenser $t^r_{sat,cond}$ is calculated based on REFPROP libraries from Eq. (4.146) and refrigerant inlet temperature $t^r_{d,cond}$ based on pressure and specific enthalpy according to Eq. (4.147).

$$t^r_{sat,cond} = t_{sat}\left(p^r_{cond}\right) \tag{4.146}$$

$$t^r_{d,cond} = h\left(p^r_{cond}, h^r_{d,cond}\right) \tag{4.147}$$

The refrigerant temperature at point a is calculated from Eq. (4.148).

$$t^r_{a,cond} = t^r_{sat,cond} - \Delta T_{sc,cond} \tag{4.148}$$

Using REFPROP libraries, the specific enthalpy of refrigerant is calculated for assumed saturation pressure at the ends of characteristic sections of the condenser according to Eqs (4.149) to (4.151).

$$h^r_{a,cond} = h\left(t^r_{a,cond}, p^r_{sat,cond}\right) \tag{4.149}$$

$$h^r_{b,cond} = h\left(q = 0, p^r_{sat,cond}\right) \tag{4.150}$$

$$h^r_{c,cond} = h\left(q = 1, p^r_{sat,cond}\right) \tag{4.151}$$

The specific enthalpy for the inlet and outlet on the cold water side ($h^d_{cw,cond}$ and $h^a_{cw,cond}$) is also read based on the temperature and pressure. The energy conservation equations calculate the heat transfer rates rejected from the refrigerant side for each heat exchanger section according to Eqs (4.152) to (4.154).

$$\dot{Q}^r_{c-d,cond} = \dot{m}^r_{cond} \cdot \left(h^r_{d,cond} - h^r_{c,cond}\right) \tag{4.152}$$

$$\dot{Q}^r_{b-c,cond} = \dot{m}^r_{cond} \cdot \left(h^r_{c,cond} - h^r_{b,cond}\right) \tag{4.153}$$

$$\dot{Q}^r_{a-b,cond} = \dot{m}^r_{cond} \cdot \left(h^r_{b,cond} - h^r_{a,cond}\right) \tag{4.154}$$

The total heat transfer rate exchanged in the condenser $\dot{Q}^r_{a-d,cond}$ is calculated as a sum of heat transfer rates from each section of the heat exchanger and assumed that the heat transfer rate equals the heat absorbed by the cold water $\dot{Q}^{cw}_{a-d,cond}$. The cold water mass flow rate is calculated using Eq. (4.155).

$$\dot{m}^{cw}_{cond} = \frac{\dot{Q}^{cw}_{a-d}}{\left(h^{cw}_{d,cond} - h^{cw}_{a,cond}\right)} \tag{4.155}$$

The specific enthalpy of the cold water at points b and c ($h^{cw}_{b,cond}$ and $h^{cw}_{c,cond}$) are estimated using Eqs (4.156) and (4.157), respectively.

$$h^{cw}_{b,cond} = h^{cw}_{a,cond} + \frac{\dot{Q}^r_{a-b}}{\dot{m}^{cw}_{cond}} \tag{4.156}$$

$$h^{cw}_{c,cond} = h^{cw}_{d,cond} - \frac{\dot{Q}^r_{c-d}}{\dot{m}^{cw}_{cond}} \tag{4.157}$$

The temperature of cold water at points b and c $t^{cw}_{b,cond}$, $t^{cw}_{c,cond}$ of the condenser is read from the REFPROP libraries based on calculated specific enthalpies and cold water pressure. Finally, the pinch point temperature difference is calculated from Eq. (4.158).

$$\Delta T_{pp,cond} = t^r_{c,cond} - t^{cw}_{c,cond} \tag{4.158}$$

The saturation pressure of the refrigerant in the condenser p^r_{cond} is iterated until the calculated value of the pinch point temperature difference $\Delta T_{pp,cond}$ reaches the assumed value $\Delta T^{hyp}_{pp,cond}$, with 1e-8 tolerance for calculation termination.

LMTD model

In the condenser case, the parameters at state point a, b, c, and d are assigned for further calculations, with several options to consider. All of them are shown in Fig. 4.11. In HXD, there are two alternatives. Option I, where the refrigerant entering the condenser is in a superheated vapor state. Then, it is to be desuperheated (c-d), condensed (b-c), and subcooled (a-b). The second possibility for HXD is Option IV, most feasible with an oversized recuperator, where the refrigerant has already started condensing in the recuperator outlet and has a two-phase state at the inlet of the condenser. Then, the condenser is only used to completely condense (b-c) and subcool (c-d) the refrigerant. In the HXA, three additional options result from insufficient heat exchange surface. Options II and III are alternatives to Option I. In Option II, the heat exchanger surface area is inadequate to condense and subcool the refrigerant fully. In Option III, the surface area is insufficient to desuperheat the refrigerant to saturation parameters. Option V is an alternative to Option IV, where the condenser surface area is too small for complete condensation and subcooling of the refrigerant.

For each of the options evaluated, the temperature and specific enthalpy were allocated to each state point (a, b, c, d) as follows:

- Option I:
  - t_a^{hot}, t_d^{cold} - assumed outlet variables
  - t_d^{hot}, t_a^{cold} - input variables
  - t_b^{hot}, t_c^{hot} - saturation temperature ($t_{sat}(p_{cond}^r)$)
  - t_b^{cold}, t_c^{cold} - $t = f(p_{cond}^{cw}, h_i^{cold})$ calculated based on p and h
  - h_a^{hot}, h_d^{hot} - $h = f(p_{cond}^r, t_i^{hot})$ calculated based on p and t
  - h_b^{hot}, h_c^{hot} - $h = f(p_{cond}^r, q)$ calculated based on p and $q = 0$ or $q = 1$, at point b and c, respectively
  - h_a^{cold}, h_d^{cold} - $h = f(p_{cond}^{cw}, t_i^{cold})$ calculated based on p and t
  - h_b^{cold}, h_c^{cold} - calculated based on energy conservation equations (Eqs (4.159) and (4.160))

$$h_b^{cold} = h_c^{cold} - \dot{m}_{cond}^{hot} \cdot \frac{h_c^{hot} - h_b^{hot}}{\dot{m}_{cond}^{cold}} \tag{4.159}$$

$$h_c^{cold} = h_d^{cold} - \dot{m}_{cond}^{hot} \cdot \frac{h_d^{hot} - h_c^{hot}}{\dot{m}_{cond}^{cold}} \tag{4.160}$$

- Option II:
  - h_b^{hot}, t_d^{cold} - assumed outlet variables

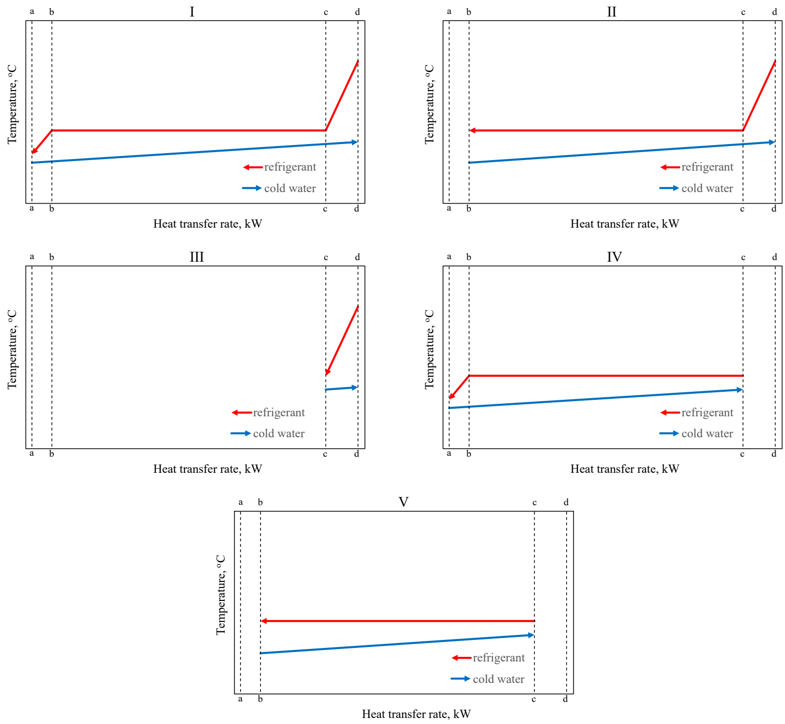

FIGURE 4.11: Condenser temperature distribution in options: I - desuperheating, condensation, and subcooling of the refrigerant, II - desuperheating and incomplete condensation of the refrigerant, III - desuperheating without reaching a saturated state of the refrigerant, IV - condensation and subcooling of the refrigerant, V - incomplete condensation of the refrigerant

- t_d^{hot}, t_b^{cold} - input variables
- t_b^{hot}, t_c^{hot} - saturation temperature $(t_{sat}(p^r_{cond}))$
- t_c^{cold} - $t = f(p^{cw}_{cond}, h_c^{cold})$ calculated based on p and h
- h_d^{hot} - $h = f(p^r_{cond}, t_d^{hot})$ calculated based on p and t
- h_c^{hot}, - $h_c^{hot} = f(p^r_{cond}, q = 1)$ calculated based on p and $q = 1$
- h_b^{cold}, h_d^{cold} - $h = f(p^{cw}_{cond}, t_i^{cold})$ calculated based on p and t
- h_c^{cold} - calculated based on energy conservation equation (Eq. (4.160))

• Option III:

- t_c^{hot}, t_d^{cold} - assumed outlet variables
- t_d^{hot}, t_c^{cold} - input variables

- h_a^{cold}, h_b^{cold} - $h = f(p_{cond}^{cw}, t_i^{cold})$ calculated based on p and t
- h_a^{hot}, h_b^{hot} - $h = f(p_{cond}^{rw}, t_i^{hot})$ calculated based on p and t

- Option IV:
  - t_a^{hot}, t_c^{cold} - assumed outlet variables
  - h_c^{hot}, t_a^{cold} - input variables
  - t_b^{hot}, t_c^{hot} - saturation temperature ($t_{sat}(p_{cond}^r)$)
  - t_b^{cold} - $t = f(p_{cond}^{cw}, h_b^{cold})$ calculated based on p and h
  - h_a^{hot} - $h = f(p_{cond}^r, t_a^{hot})$ calculated based on p and t
  - h_b^{hot} - $h = f(p_{cond}^r, q = 0)$ calculated based on p and $q = 0$
  - h_a^{cold}, h_c^{cold} - $h = f(p_{cond}^{cw}, t_i^{cold})$ calculated based on p and t
  - h_b^{cold} - calculated based on energy conservation equation (Eq. (4.159))

- Option V:
  - h_b^{hot}, t_c^{cold} - assumed outlet variables
  - h_c^{hot}, t_b^{cold} - input variables
  - t_b^{hot}, t_c^{hot} - saturation temperature ($t_{sat}(p_{cond}^r)$)
  - h_b^{cold}, h_c^{cold} - $h = f(p_{cond}^{cw}, t_i^{cold})$ calculated based on p and t

As previously noted, the convective heat transfer coefficient (α) and friction factor (f) were established using the LMTD model to compute the overall heat transfer coefficient and pressure drop for each heat exchanger section. The following algorithms, described in Section 4.2, were used to calculate the Nusselt number and friction factor in each section of the condenser:

- Section a-b

  To calculate the Nusselt number for hot fluid Nu_{a-b}^{hot}, i.e., the refrigerant in a liquid phase, the Nu-correlation-I described by Eq. (4.77) was used. In the case of cold fluid, i.e., cold water, the Nu-correlation-V, described by Eq. (4.87), was used to calculate Nu_{a-b}^{hot}. For both fluids, the friction factor f_{a-b} was computed using the f-correlation-I, described by Eq. (4.89).

- Section b-c

  For Section b-c, where refrigerant condensation takes place, the values of Nusselt number Nu_{b-c}^{cold} and friction factor f_{b-c}^{cold} for cold water were calculated according to the same algorithms as for Section a-b. For the condensing hot fluid, that is, for the refrigerant, the Nu-correlation-IV described by Eq. (4.86) was used to calculate the Nusselt number Nu_{b-c}^{hot}. The f-correlation-III described by Eq. (4.94) was used to calculate the friction factor f_{b-c}^{hot}.

- Section c-d

  Finally, for Section c-d, where desuperheating of the refrigerant vapor occurs, the same correlations for cold water as in earlier sections of the condenser were again used to calculate Nu_{c-d}^{cold} and f_{c-d}^{cold}. For the refrigerant vapor on the hot side of the condenser, the Nu-correlation-II described by Eq. (4.81) was used to calculate the Nusselt number Nu_{c-d}^{hot} and similarly as in Section a-b f-correlation-I, described by Eq. (4.89) to calculate the friction factor f_{c-d}^{hot}.

The primary outcome of the condenser calculation using the LMTD model is the temperature distribution within the heat exchanger. Depending on the calculation mode, in HXD, the details about the number of condenser plates $N_{t,cond}$ and the pressure drops on both sides of the heat exchanger ΔP_{gen}^{cold} and ΔP_{gen}^{hot}, are obtained. In HXA, the outlet temperatures from the condenser $t_{out,cond}^{hot}$, $t_{out,cond}^{cold}$, along with the pressure drops, are determined.

4.2.5 Recuperator

Since there is no need to iteratively calculate the internal pressures on the cold and hot sides of the recuperator, and they are derived from the computed saturation pressure in the condenser and generator, respectively, there is no need to build a simple model of the recuperator. The only model used in this case is the LMTD model.

LMTD model

The recuperator LMTD model covers only one considered case of a heat exchanger. The temperature distribution in the heat exchanger is shown in Fig. 4.12. The recuperator has only one section, where the target is to preheat the liquid high-pressure refrigerant before the generator or preheater on the cold side and cool down the vapor refrigerant before entering the condenser on the hot side. That improves the COP of the system.

To calculate the heat exchanger in the LMTD model, parameters, i.e., temperatures and specific enthalpy at points c and d, must be assigned before calculating the overall heat transfer coefficient and pressure drop. In this case, it is implemented as follows:

- t_c^{hot}, h_d^{cold} - assumed outlet variables
- t_d^{hot}, t_c^{cold} - input variables
- h_c^{cold}, h_d^{cold} - $h = f(p_{gen}^r, t_i^{cold})$ calculated based on p and t
- h_c^{hot}, h_d^{hot} - $h = f(p_{cond}^r, t_i^{hot})$ calculated based on p and t

The following algorithms, described in Section 4.2, were used to calculate the Nusselt number and the friction factor in the recuperator:

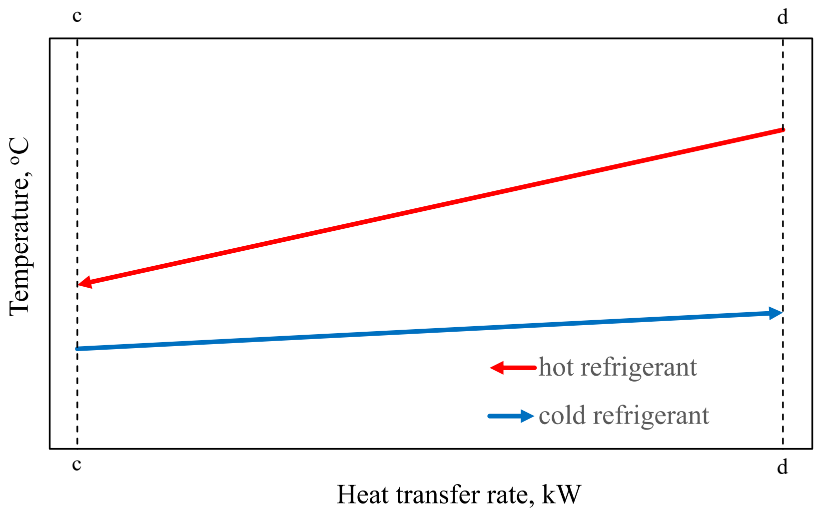

FIGURE 4.12: Recuperator temperature distribution

- Section b-c

  To calculate the Nusselt number for cold fluid Nu_{c-d}^{cold}, i.e., the refrigerant in a liquid phase, the Nu-correlation-I described by Eq. (4.77) was used. In the case of hot fluid, i.e., the refrigerant in a vapor phase, the Nu-correlation-II, described by Eq. (4.81), was used to calculate Nu_{c-d}^{hot}. For both fluids, the friction factor f_{c-d} was computed using the f-correlation-I, described by Eq. (4.89).

The final result of the recuperator calculation using the LMTD model depends on the calculation mode. In HXD, the information about the number of recuperator plates $N_{t,recup}$ and the pressure drops on both sides of the heat exchanger ΔP_{recup}^{cold} and ΔP_{recup}^{hot} is obtained. In HXA, the recuperator outlet temperatures $t_{out,recup}^{hot}$ and $t_{out,recup}^{cold}$, and the pressure drops are calculated.

4.3 Pump

The simple pump model calculates the circulation pump outlet parameters and performance. In HXD, the required head of the pump Δp_{pump} at the first iteration is calculated from Eq. (4.161), where it is the difference between the generator and condenser saturation pressure.

$$\Delta p_{pump} = p_{gen}^{r} - p_{cond}^{r} \tag{4.161}$$

Then also, the pressure drops in the heat exchangers are included, and Δp_{pump} is estimated using Eq. (4.162), where $\sum \Delta P_{suc}$ the sum of pressure drops at the suction side of the pump including the pressure drops in the condenser and $\sum \Delta P_{dis}$ is the sum of pressure drops at the discharge of the pump including the pressure drops in generator and optionally in the recuperator and preheater.

$$\Delta p_{pump} = p^r_{gen} + \sum \Delta P_{dis} - \left(p^r_{cond} - \sum \Delta P_{suc}\right) \tag{4.162}$$

Based on the head of the pump Δp_{pump} and the required pump capacity expressed by the mass flow rate of the refrigerant in the condenser $\dot{m}^r_{cond}$, the pump operating point is determined from pump characteristics. The isentropic efficiency $\eta_{is,pump}$ and pump power demand $P_{el,pump}$ is read from the characteristics. Without the availability of pump characteristics or consideration of the general case, $\eta_{is,pump}$ of 0.35 is assumed. The specific enthalpy of the refrigerant at the pump outlet is calculated from Eq. (4.163).

$$h_{pump,out} = h_{pump,in} + \frac{h_{is,pump,out} - h_{pump,in}}{\eta_{is,pump}} \tag{4.163}$$

Other pump outlet parameters are estimated based on absolute pressure and specific enthalpy from the REFPROP library. The pump nominal power is calculated from Eq. (4.164).

$$P_{nom,pump} = \dot{m}_{ref} \cdot \left(h_{pump,out} - h_{pump,in}\right) \tag{4.164}$$

In case of lack of information about the pump, the electric power demand is calculated from Eq. (4.165), assuming a mechanical-electrical efficiency of the pump $\eta_{me,pump}$. The values of $\eta_{is,pump}$ and $\eta_{me,pump}$ can be modified and adapted to the designer requirements or the characteristics of the particular pump under consideration. Instead of a single value, a characteristic of efficiency as a function of pump capacity or discharge pressure can also be used.

$$P_{el,pump} = \frac{P_{nom,pump}}{\eta_{me,pump}} \tag{4.165}$$

4.4 Expansion valve

The simple expansion valve model uses the assumption of isenthalpic expansion of the refrigerant, according to Eq. (4.166).

$$h^r_{exp,out} = h^r_{exp,in} \tag{4.166}$$

The refrigerant parameters at the outlet of the expansion valve are calculated based on the calculated specific enthalpy and saturation pressure in the evaporator p^r_{evap}.

4.5 Refrigeration system model solution strategy

The algorithm was written in a Python environment, using object-oriented programming, which separates all single components of the refrigeration system and allows the possibility of quickly modifying each single component model in the future. The real gas thermodynamic properties of the refrigerant and heat transfer fluids were calculated using the REFPROP 10.0 library [82]. Other Python packages, such as SciPy [98], NumPy [99], Matplotlib [100], and Pandas [88], were adopted for the iterative solution of systems of equations, creating the array variables, graphic presentation of the results, and loading and saving data in Microsoft Excel files, respectively.

The simplified model layout of the most complex variant of system configuration V4 is presented in Fig. 4.13. The input data entered into the model include information about the waste heat source, such as the waste heat available to recover, its medium, temperature, pressure level, mass/volume flow rate, etc. Information about the demand for cooling capacity with the required temperature levels is also considered in relation to ambient conditions or condenser cooling water parameters for the designing point.

Several initial assumptions are necessary for the generator, evaporator, and condenser to start the calculations, such as the assumed minimal temperature (pinch point), outlet superheating or subcooling temperature difference, and thermal efficiency. Based on these assumptions, the heat exchangers are initially calculated using simplified models to obtain the temperature distribution and heat transfer rates inside the heat exchanger. Iterative adjustment of the saturation pressure of the refrigerant is performed to obtain the assumed level of pinch point temperature difference, using the least squares method with the trust region reflective algorithm [86].

In the first iteration, the generator inlet parameters at the refrigerant side are assumed for the generator calculation. The saturation pressure of the refrigerant is calculated to avoid crossing the temperature distributions of the refrigerant and heat transfer fluid.

Next, the parameters at the expansion valve outlet are calculated using the simple model. Afterward, the maximal mass entrainment ratio of the ejector is iteratively determined with limited boundaries in the range of 0.0 to 0.6, using the Brent method [87]. The objective function f_{MER} described by Eq. (4.167) is formulated to achieve critical operation of the ejector, where the ejector outlet pressure is greater than the condensation saturation pressure of the refrigerant. In the objective function, the pressure difference between the ejector outlet pressure and the saturation pressure in the condenser is purposely divided by its module to avoid the influence of the magnitude of the pressure difference on the result of MER maximizing.

$$f_{MER} = -MER \cdot \frac{p_{ej,out} - p_{cond,sat}}{\left|p_{ej,out} - p_{cond,sat}\right|} -> min \tag{4.167}$$

The previously calibrated supersonic ejector 0-D model predicts the ejector geometry and estimates the parameters at the ejector outlet. Next, the plate heat exchanger

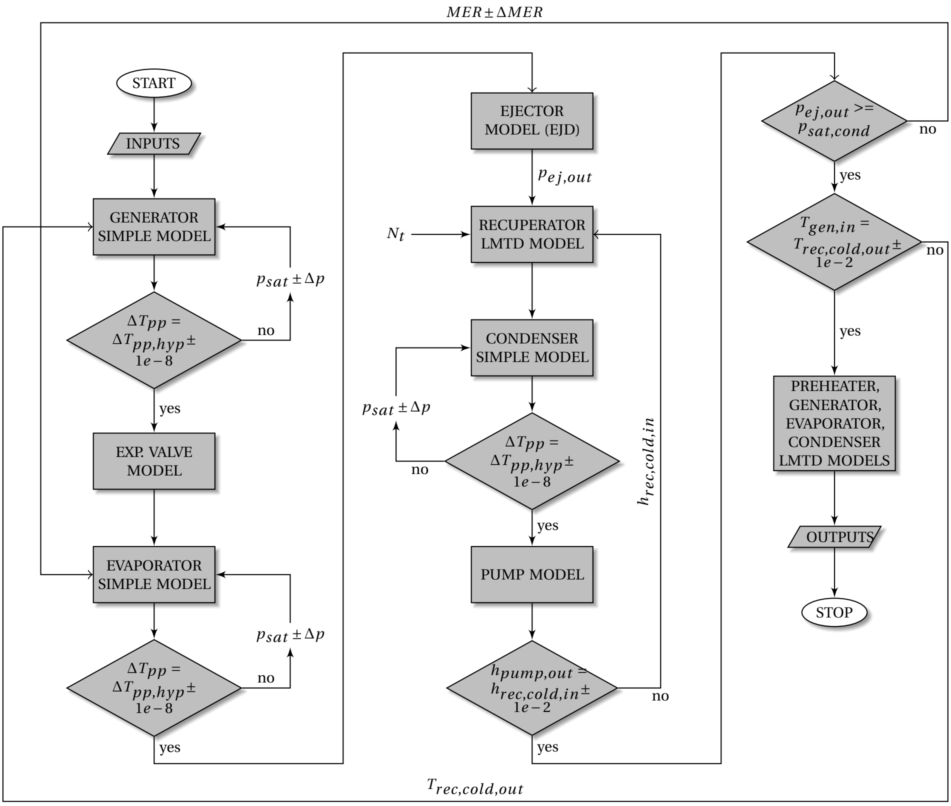

FIGURE 4.13: Refrigeration system model scheme for system variant V4 with recuperator and with preheater

model is used to find the heat transfer rate exchanged in the recuperator and the outlet parameters at its hot and cold ends. The inlet parameters at the cold side of the recuperator must be iteratively adjusted.

Afterward, the simple condenser model is used to find the refrigerant condensation pressure, and the pump model is used to calculate the parameters at the discharge nozzle, corresponding to the parameters at the recuperator cold inlet. The iteration loop ends when the generator inlet parameters are converged.

Then, the plate heat exchanger LMTD models are applied to find the total heat transfer area and the number of plates for the generator, evaporator, condenser, and preheater.

The COP of the system is calculated from Eq. (4.168).

$$COP = \frac{\dot{Q}_0}{\dot{Q}_{gen} + P_{el,pump}} \tag{4.168}$$

where $\dot{Q}_0$ and $\dot{Q}_{gen}$ are the refrigeration capacity and generator thermal power, respectively.

All output data is transferred to a post-processing script to present results as a PDF report containing tables with information on the parameters of individual components, including input data, assumptions made and parameters calculated, and graphs with temperature distribution in individual plate heat exchangers. The above-detailed calculation procedure of the ejector refrigeration system will be useful for the analysis of the rational components selection strategy. Therefore, it will be possible to analyze various variants of the heat transfer components selection that affect various available COP levels, resulting in various investment costs for the entire system. The above opens a more advanced analysis of the optimum composition as well as the configuration of the ejector refrigeration system driven by industrial waste heat.

Chapter 5

Results and discussion

5.1 Ejector results

5.1.1 Verification of the ejector model

Verification of ejector model under on-design operation mode for R141b used as refrigerant

Before conducting experimental tests on prototype refrigeration systems, the 0-D model of the ejector was verified against existing literature data for HFC refrigerants. Initially, it was compared with experimental data from Huang et al. [68], which described the performance of several R141b gas ejectors under design conditions for various motive and suction nozzle inlet temperatures (t_{mn}, t_{sn}). The ejector efficiencies were adjusted to achieve a relative error below 10% for all operating points, resulting in the following values: $\eta_{mn} = 0.97$, $\eta_{mn,out,hyp} = 0.85$, $\eta_{sn} = 0.8$, $\eta_{mix} = 0.93$, $\eta_{dif} = 1$. Compared to the work of Chen et al. [73], the efficiencies for expansion in the ejector motive nozzle were increased, and the suction nozzle isentropic efficiency was decreased to improve the accuracy of MER results. The η_{mix} was slightly adjusted, mainly affecting the critical pressure estimation. The results, shown in Table 5.1, indicated that the MER relative estimation error δ_{MER} ranged from -7.5% to +7.5%, with an average of 3.4%. The relative error for the ejector critical pressure $\delta_{p_{crit}}$ ranged from -10.1% to 1.9%, with an average of 4.5%. The comparison between the 0-D model results and the experimental data from Huang et al. [68] demonstrated that a well-calibrated 0-D model can accurately simulate gas ejector performance under on-design conditions and reproduce key parameters across a wide range of operating conditions.

Validation of ejector model under on-design and off-design operation modes using R134a as refrigerant

The ejector model was also initially verified with the results for R134a refrigerant taken from the work of Garcia del Valle et al. [101], who presented the results of gas ejector working under on-design and off-design operating conditions. They presented detailed

TABLE 5.1: Comparison of model results with experimental data from Huang et al. [68]

No.	$d_{mn,th}$ mm	$d_{mn,out}$ mm	d_{mix} mm	t_{mn} °C	t_{sn} °C	MER -	p_{crit} bar	δ_{MER} -	$\delta_{p_{crit}}$ -
1	2.64	4.50	6.70	95	8	0.19	1.42	-7.5%	0.4%
2	2.64	4.50	6.70	90	8	0.23	1.28	-4.8%	-1.1%
3	2.64	4.50	6.70	84	8	0.29	1.14	-4.8%	-1.3%
4	2.64	4.50	6.70	78	8	0.33	1.03	6.8%	0.1%
5	2.64	4.50	6.70	95	12	0.24	1.44	-0.9%	-2.0%
6	2.64	4.50	6.70	90	12	0.30	1.31	-3.7%	-2.7%
7	2.64	4.50	6.70	84	12	0.34	1.16	4.9%	-3.3%
8	2.64	4.50	6.98	90	8	0.27	1.22	-7.4%	-1.1%
9	2.64	4.50	6.98	84	8	0.31	1.07	2.2%	-3.2%
10	2.64	4.50	6.98	78	8	0.39	0.93	2.0%	-6.2%
11	2.64	4.50	7.34	95	8	0.26	1.27	-1.8%	-0.8%
12	2.64	4.50	7.34	90	8	0.30	1.19	-0.2%	1.9%
13	2.64	4.50	7.34	84	8	0.39	1.02	-2.4%	-2.0%
14	2.64	4.50	7.34	78	8	0.44	0.91	7.0%	-1.8%
15	2.64	4.50	7.34	95	12	0.35	1.27	-6.6%	-4.2%
16	2.64	4.50	7.34	90	12	0.40	1.16	-3.2%	-4.2%
17	2.64	4.50	7.34	84	12	0.48	1.03	0.3%	-5.6%
18	2.64	4.50	7.34	78	12	0.61	0.92	-3.9%	-5.7%
19	2.64	4.50	7.60	95	8	0.28	1.17	1.4%	-4.6%
20	2.64	4.50	7.60	90	8	0.35	1.08	-1.7%	-4.1%
21	2.64	4.50	7.60	84	8	0.42	0.96	0.1%	-4.5%
23	2.64	4.50	8.10	95	8	0.35	1.07	3.1%	-6.6%
24	2.64	4.50	8.10	90	8	0.45	0.99	-4.9%	-4.8%
25	2.64	4.50	8.10	84	8	0.54	0.88	-3.9%	-6.4%
26	2.64	4.50	8.10	78	8	0.62	0.77	1.5%	-8.5%
27	2.64	4.50	8.10	95	12	0.45	1.10	-0.2%	-7.3%
28	2.64	4.50	8.10	90	12	0.54	1.01	-1.8%	-7.1%
29	2.64	4.50	8.10	84	12	0.64	0.91	1.6%	-7.4%
30	2.64	4.50	8.10	78	12	0.74	0.81	5.3%	-8.3%
31	2.82	5.10	7.34	95	8	0.20	1.37	-6.0%	-0.3%
32	2.82	5.10	7.60	95	8	0.23	1.28	-2.4%	-3.7%
33	2.82	5.10	7.60	95	12	0.30	1.30	-3.7%	-5.8%
34	2.82	5.10	8.10	95	8	0.29	1.21	-2.4%	-2.1%
35	2.82	5.10	8.54	95	8	0.35	1.09	-2.7%	-6.0%
36	2.82	5.10	8.54	95	12	0.40	1.09	7.5%	-10.1%
37	2.82	5.10	8.84	95	8	0.39	1.05	-2.8%	-6.2%
38	2.82	5.10	8.84	95	12	0.50	1.05	-2.9%	-9.9%
39	2.82	5.10	9.20	95	8	0.44	0.98	-0.6%	-8.3%

information about the ejector geometry, giving the possibility of using different calculation approaches, including CFD. In all the cases, the experimental data for “A” geometry was used to compare the results. The boundary conditions for the considered operating points under the ejector on-design mode are presented in Table 5.2.

The calculations using the ejector model were performed with three different sets of ejector efficiencies. Initially, the efficiencies were assumed to be 1. Next, they were determined using a numerical approach. Finally, the calculations were repeated after adjusting η_{sn} and η_{mix}. The results for ejector operation under on-design conditions are illustrated in Fig. 5.1, where the calculated MER and pressure ratio are compared with experimental results from Garcia del Valle et al. [101]. The three variants are

TABLE 5.2: Experimental data of ejector under on-design conditions from Garcia del Valle et al. [101]

No.	t_{mn} °C	p_{mn} bar	t_{sn} °C	p_{sn} bar	MER -	p_{ratio} -
1	89.4	25.98	17.0	3.75	0.422	1.995
2	89.4	25.98	20.0	4.15	0.494	1.826
3	94.4	28.89	17.0	3.75	0.342	2.157
4	94.4	28.89	20.0	4.15	0.398	1.994
5	99.2	31.88	15.0	3.50	0.273	2.333
6	99.2	31.88	17.0	3.75	0.297	2.310
7	99.2	31.88	20.0	4.15	0.339	2.164

labeled as "component efficiencies = 1," "component efficiencies based on CFD," and "corrected component efficiencies," respectively.

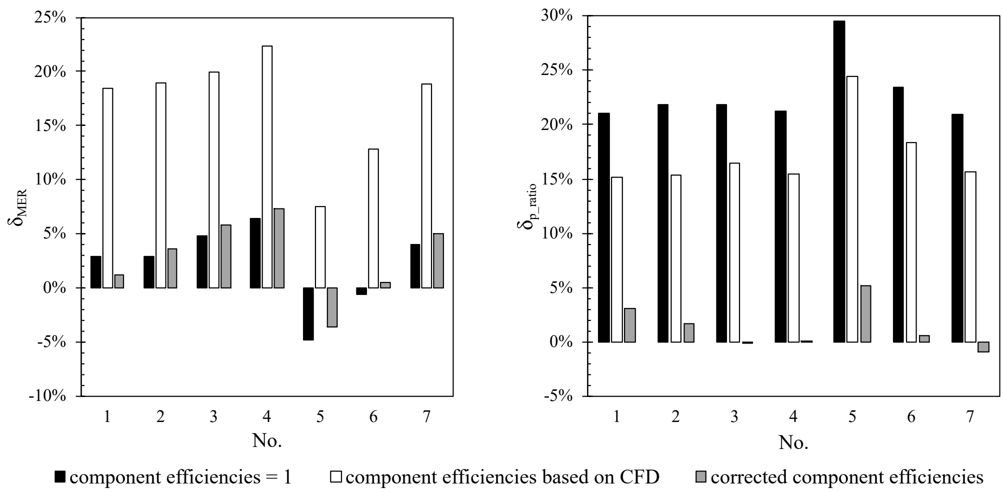

FIGURE 5.1: Relative discrepancies between calculated MER (left) and pressure ratio (right) and experimental data from Garcia del Valle et al. [101] for three sets of efficiencies of 0-D ejector model.

The initial calculations using the ejector model were conducted without calibrating the ejector component efficiencies, with all values assumed to be 1. As shown in Fig. 5.1, the uncalibrated model provided good accuracy in estimating MER values, with errors under 7% for all cases. However, the accuracy of the ejector outlet pressure and the resulting ejector pressure ratio p_{ratio} was significantly overestimated, indicating the necessity for the model calibration.

A numerical approach was used as a reference to calibrate the ejector efficiencies. The well-validated EjectorPL software, described by Smolka et al. [102], was employed for seven operating points presented by Garcia del Valle et al. [101] This software, based on Ansys Fluent, allows for quick estimation of ejector flow parameters for various refrigerants under a wide range of operating conditions. This study assumed the Homogeneous Equilibrium Model and the $k-\epsilon$ Realizable turbulence model was set. A 2-D axisymmetric mesh was constructed based on the geometry of ejector "A" from Garcia del Valle et al. [101]. Due to the lack of information about the distance between the motive nozzle outlet and the mixer inlet for each specified operating condition, a value of 5.58 mm was assumed based on the information from the paper above. The missing motive nozzle convergence angle was considered 20°, and the motive nozzle outlet side wall convergence angle was assumed to be 30°, equal to the pre-mixing chamber convergence angle. A mesh sensitivity analysis was then performed. The relative discrepancies in MER estimation between the CFD model results and the experimental data from Garcia del Valle et al. [101] were averagely at the level of 3.8%, with a maximum error of 7.7%.

Based on the CFD results, the ejector efficiencies were determined. The necessary thermodynamic properties of the refrigerant were obtained from the characteristic cross-sections of the ejector, such as the motive nozzle inlet, throat, and outlet, as well as the mixer inlet, diffuser inlet, and outlet. These properties were averaged over the surface area. The areas for the motive nozzle flow and the suction nozzle flow at the mixer inlet were adjusted for each operating condition by modifying the diameter of the motive flow part and the thickness of the annular suction fluid to match their inlet values.

The ejector component efficiencies were calculated by transforming the equations used in the 0-D model (Eqs (4.8), (4.19), (4.25), (4.29), (4.57)) and inserting the relevant thermodynamic parameters from the CFD results. The calculated ejector efficiencies were then averaged across all operating points, resulting in the following values: η_{mn} = 1, $\eta_{mn,out,hyp}$ = 0.99, η_{sn} = 1.3, η_{mix} = 0.79, and η_{dif} = 1. It was noted that the isentropic efficiency of the suction nozzle exceeded 1, which is inconsistent with its thermodynamic definition. This discrepancy was attributed to the 2-D axisymmetric simplification of the ejector geometry, inaccuracies in determining the cross-section of the entrained fluid, and the calculation of thermodynamic parameters as area-weighted averages on the annular surface, where they varied significantly along the ejector radius.

Despite this, the calculated efficiencies were applied to the model, and the results were compared with experimental data. Fig. 5.1 shows that the relative discrepancies in the MER values estimation increased significantly compared to the model using component efficiencies of 1. The error ranged from +7.6% for operating point no. 5 to +22.4% for no. 4, with an average of 17.0%. This was mainly due to the high underestimation of the suction nozzle mass flow influenced by η_{mix}. For the value used in the calculations, the ejector critical pressure was below the condenser pressure, reducing the entrained vapor mass flow despite the falsely high suction nozzle isentropic efficiency. It was also noted that predicting a credible value for η_{mix} was challenging due to its high sensitivity to changes in the assumed theoretical dimensions of the cross-sections of the two streams and the method of averaging the thermodynamic parameters along the ejector radius. Moreover, η_{mix} simplifies the flow processes in the ejector mixer, and its accurate determination based on detailed field results may not be feasible.

Under the circumstances presented above, it was concluded that the evaluated values of η_{sn} and η_{mix} based on the CFD results were unreliable and corrected only based on the experimental data. After the sensitivity analysis, the corrected value of η_{mix} was 0.9. In the case of η_{sn}, the previously used value of 1 was assumed. The δ_{MER} ranged from -3.7% for operating point no. 5 to +7.3% for no. 4 with an absolute average of 3.9%. Simultaneously, the $\delta_{p_{ratio}}$ significantly decreased ranged from -0.9% for no. 7 to +5.2% for no. 5 with an absolute average of 1.6%. The estimation accuracy of ejector key parameters was considered satisfactory.

Finally, the ejector off-design mode was tested based on the experimental data from Garcia del Valle et al. [101]. The MER results as a condenser temperature function were compared in Fig. 5.2. The results for three previously used sets of parameters of the 0-D ejector model were shown. It was noticed that the results obtained from the model with the corrected ejector component efficiencies provided satisfying results under on-design and off-design conditions. In contrast, the others led to a significant discrepancy with experimental data.

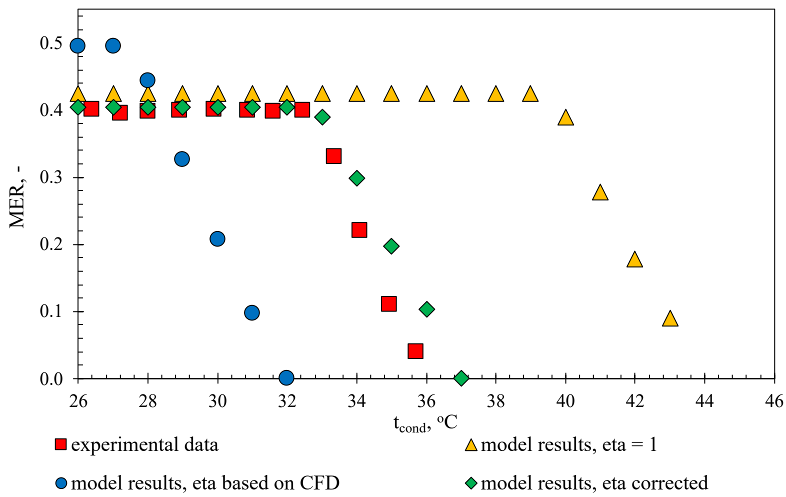

FIGURE 5.2: Results of the ejector MER in a function of the condensation temperature in comparison with experimental data from Garcia del Valle et al. [101]

5.1.2 Validation of the ejector model based on own experimental results

Experimental operating conditions of the ejector in the prototype refrigeration systems

To validate the model of the supersonic ejector under on-design and off-design conditions, the results of the calculations were compared with the results of an experiment carried out on prototype cooling units powered by the waste heat transfer rate of 200 kW (MARANI CHILLER 200) and 600 kW (MARANI CHILLER 600). As mentioned in Chapter 3.2, five independent measurement campaigns, MC-1 to MC-5, were performed. The boundary conditions for motive and suction nozzle inlets and outlet of the studied ejectors in each measurement campaign are shown in the $p-h$ diagrams in Fig. 5.3, where operating points from tests of the MARANI CHILLER 200 prototype are presented and Fig. 5.4, which shows the operating parameters from experimental campaigns of MARANI CHILLER 600.

The MC-1 test campaign consisted of two measurement series performed on the ejector refrigeration system nominally driven by waste heat of 200 kW. The series of 150 kW covered ultra-low parameters at the inlet of the motive nozzle. The average motive pressure was 2.81 bar(a), and the temperature was 59°C, corresponding to around 11 K of vapor superheating. The ejector did not operate under nominal conditions, driven by waste heat of 150 kW. The parameters at the suction nozzle inlet corresponded to those of high-temperature cooling. The average pressure was 0.76 bar(a), and the temperature was 18.8°C, corresponding to a vapor superheat of 8 K. In this series of measurements, the refrigeration system was tested for condensation temperature, contributing to a range of pressures measured at the ejector outlet from 1.19 ± 0.02 to 1.27 ± 0.02 bar(a). The average refrigerant temperature was 52.2°C, corresponding to superheat of about 29 K. Twelve operating points were registered in the first series.

The test bench obtained a higher waste heat transfer rate in the 170 kW series. Moreover, eliminating the faulty check valve allowed it to reduce pressure losses downstream of the refrigerant pump, resulting in higher pressure on the ejector motive nozzle, around 3.20 bar(a). The temperature was average 53.6°C, which gave a superheating of only 0.7 K. From the point of view of the superheating of the motive fluid, this series differed significantly from the other measurements, which should be considered when evaluating the results. Similar parameters at the suction nozzle inlet have been maintained. The average pressure for the entire series of measurements was 0.80 bar(a), and the temperature was 18.8°C, resulting in a superheat of about 6.7 K. Seven operating points were registered in that series for various condensation temperatures. This resulted in an outlet pressure range of 1.27 ± 0.02 to 1.39 ± 0.02 bar(a) and the average temperature of about 46.9°C, corresponding to the refrigerant vapor superheating range of 17 to 24 K.

After changing the geometry of the mixing chamber and the ejector diffuser and modifying the waste heat system, as described in Chapter 3.4, the MC-2 measurement campaign was carried out under rated operating conditions of the refrigeration system.

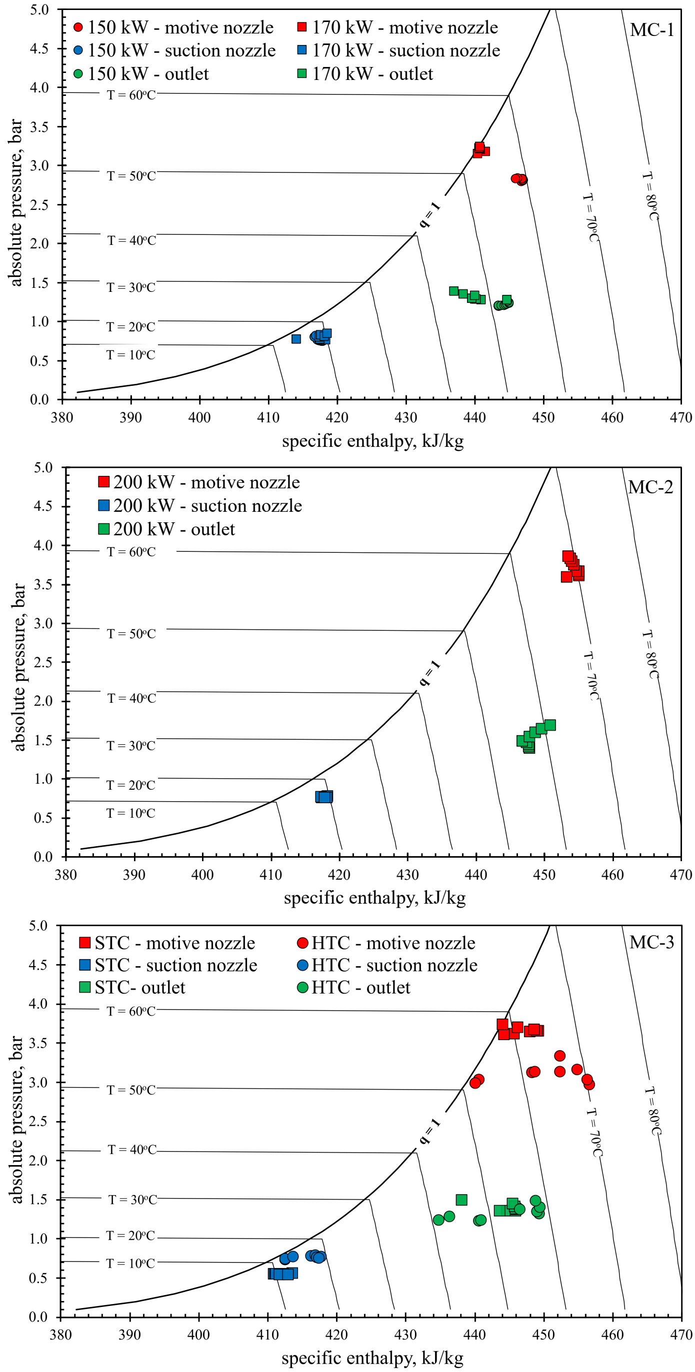

FIGURE 5.3: Boundary conditions of ejector operating in MARANI CHILLER 200 prototype in measurement campaigns MC-1 to MC-3

This series provided the motive nozzle inlet operating points with an average pressure of 3.72 bar(a) and temperature of 69.6°C with a superheat of 11 K. Again, it was possible to realize a measurement campaign only for high-temperature cooling parameters. For ten measurement points recorded, the average pressure of the refrigerant at the suction nozzle inlet was 0.77 bar(a). The temperature was 19.3°C, corresponding to an average superheat of about 8 K. As in the previous measurement series, the performance of the ejector was examined for varying values of condensation pressure, which determined the variation of pressure at the outlet of the ejector. It ranged from 1.40 ± 0.02 to 1.72 ± 0.02 bar(a) with an average temperature of about 58.1°C. The average superheat of the refrigerant vapor at the outlet of the ejector was 28.3 K.

Another test of the 200 kW waste heat-driven cooling system was carried out after further pressure drop limitations, this time by eliminating the recuperator in the MC-3 measurement campaign. The pressure drop limitations made it possible to carry out two measurement series for high-temperature cooling (HTC) and standard cooling (STC). In the first of these measurement series, the parameters at the ejector motive nozzle corresponded to an average pressure of 3.12 bar(a). Due to the unstable operation of the heat source, which was the air compressors, the temperature at the motive nozzle was quite unstable. It fluctuated between 52.2 ± 0.2°C and 70.5 ± 0.2°C, corresponding to the range of 1.8 ± 0.2 K and 20.1 ± 0.2 K of the vapor superheat. The average pressure at the inlet to the suction nozzle of the ejector was 0.76 bar(a), and the temperature was in the range of 12.4 ± 0.1°C and 19.1 ± 0.1°C, corresponding to vapor superheat of 2.4 ± 0.1K and 7.9 ± 0.1 K. As in the previous measurement campaigns, the operating characteristics of the ejector were determined for varying condensation temperature, which corresponded to a variation of pressure at the outlet of the ejector in the range of 1.23 ± 0.02 bar(a) and 1.48 ± 0.02 bar(a), with an outlet temperature in the range of 48.0 ± 0.1°C and 58.6 ± 0.02°C. The average superheat of the outlet vapor was 26.7 K.

In the STC series, similar conditions were maintained at the ejector motive nozzle, where the average pressure was 3.66 bar(a). More stable operating conditions were obtained, and the temperature ranged from 58.5 ± 0.2°C to 64.0 ± 0.2°C, and the superheat of the motive vapor ranged from 0.2 ± 0.2 K to 6.4 ± 0.2 K. The average pressure at the suction nozzle of the ejector was 0.55 bar(a), and the temperature ranged from 9.8 ± 0.1°C to 13.1 ± 0.1°C, corresponding to a vapor superheat in the range of 6.6 ± 0.1 and 9.7 ± 0.1 K. The pressure at the outlet of the ejector was in the range of 1.35 ± 0.02 and 1.50 ± 0.02 bar(a), and the temperature was from 45.8 ± 0.2°C to 54.7 ± 0.2°C, which corresponded to average vapor superheat of 25.8 K.

In the MC-4 test campaign, a set of 3 ejectors was tested in the 600 kW waste heat-driven refrigeration system. In this system configuration, the steam heating system was much less stable than the air compressor heat recovery, affecting the results accuracy and the lower number of individual readings for the recorded measurement points. In addition, due to the use of water steam, the vapor superheating at the ejector motive nozzle was much higher than assumed in the design of the devices. The motive nozzle pressure ranged from 3.25 ± 0.04 to 4.45 ± 0.03 bar(a), and the temperature from

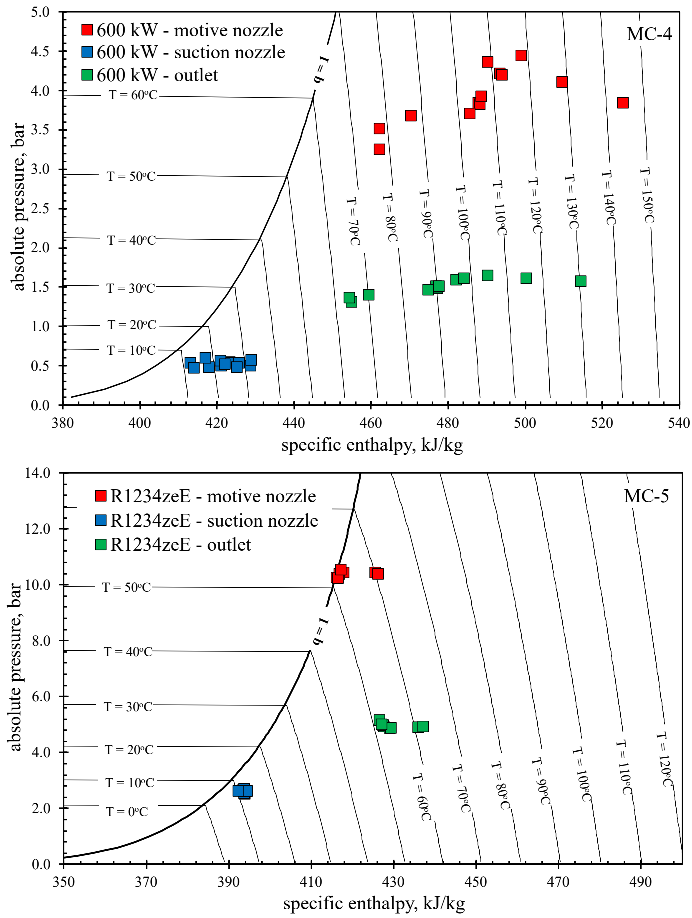

FIGURE 5.4: Boundary conditions of ejector operating in MARANI CHILLER 600 prototype in measurement campaigns MC-4 and MC-5

77.3 ± 0.2°C to 144.6 ± 0.5°C, corresponding to a vapor superheat of 21.6 ± 0.2 K to 85.3 ± 0.5 K. At the suction nozzle, a stable pressure was obtained at an average level of 0.52 bar(a) and a temperature range of 12.6 ± 0.1°C to 32.3 ± 0.1°C, corresponding to superheating of the refrigerant vapor from 8.4 ± 0.1 K to 30.5 ± 0.1 K. The pressure at the ejector outlet was in the range of 1.30 ± 0.02 to 1.65 ± 0.02 bar(a), and the temperature was in the range of 64.3 ± 0.2°C to 130.5 ± 0.4°C, reaching the superheating of even 100 K.

In the last test campaign, MC-5, it was decided to change the refrigerant to R1234zd(E) and modify the heating system to reduce refrigerant superheating at the ejector motive nozzle. Six test points were obtained, four of them with the limited vapor superheating of the ejector motive nozzle. The average pressure at the ejector motive nozzle was 10.56 bar(a). The temperature for the four mentioned operating points was between 57.7 ± 0.4°C and 68.9 ± 0.2°C, which corresponded to a superheating of 7.2 ± 0.4 K to

15.7 ± 0.2 K. For the other two points, the temperature was about 102°C, which corresponded to a superheating around 51 K. The pressure at the ejector suction nozzle averaged 2.50 bar(a), corresponding to standard chilled water parameters. The temperature at the suction nozzle for the four low-temperature points mentioned was 8.6 ± 0.1°C to 12.7 ± 0.1°C, resulting in superheating of 5.7 ± 0.1 K to 8.9 ± 0.1 K. For the other two points, the average temperature of 15.5°C, corresponding to superheating of 10.5 K, was obtained. The average pressure at the ejector outlet was 5 bar(a). The temperature ranged from 42.6 ± 0.3°C to 87.3 ± 0.2°C depending on the case, resulting in a vapor superheat range between 19.6 ± 0.2 K and 62.2 ± 0.4 K.

Calibration and validation of the ejector model based on experimental results

To calibrate the ejector component efficiencies, the differential evolution method [103] was used. The sets of calibrated ejector component efficiencies are presented in Table 5.3. First, the η_{mn} was calibrated to obtain the minimal relative error in $\dot{m}_{mn}$ estimation. This was achieved to get a high accuracy reaching $\delta_{\dot{m}_{mn}}$ up to ±5%, with a few exceptions for measurements recorded in the MC-4 campaign when the relative error was maximally 13.4%. However, the above measuring campaign was the most demanding in achieving stable refrigeration system operation. Then the $\eta_{mn,hyp}$, η_{sn}, η_{mix}, and η_{dif} component efficiencies were optimized collectively, minimizing the relative error of $\delta_{\dot{m}_{mn}}$ estimation. All five of these above component efficiencies were calibrated for each series of measurements, where the parameters at the inlets of the ejector were close to each other. For measurement campaigns MC-1 and MC-2, the series of measurements were combined and used to jointly calibrate the model to test the sensitivity of the calculations to the assumptions made and the feasibility of using a single set of parameters over the most expansive possible area of ejector operation. The obtained ejector component efficiencies for this set of experimental measurements are denoted in Table 5.3 as MC-1 + MC-2.

In the cases MC-1, MC-2, and MC-3, surprisingly low values of η_{sn} in the range between 0.45 and 0.57 were obtained. This efficiency significantly differed from the values from the ejector mathematical models described in the literature [68], [69], [73], [75], [104], where η_{sn} of 0.85 was assumed. Moreover, in the publications above, $\eta_{mn,hyp}$ was in the range from 0.80 to 0.88, which also differed from the results obtained, especially for the component efficiency estimated for MC-1 150 kW series, MC-3 HTC series and case MC-1 + MC-2. The other component efficiencies η_{mn}, η_{mix}, and η_{dif} were within the range of the values previously selected in the ejector models found in the literature [68], [69], [73], [75], [104], which were 0.85 to 0.95, 0.80 to 0.95, and 0.85 to 1.00, respectively.

It is worth mentioning that according to the (4.19) suction nozzle efficiency η_{sn} describes the expansion of the refrigerant from the suction nozzle inlet to the hypothetical throat of the ejector. According to model assumptions, that hypothetical cross-section is placed inside the ejector mixing chamber. Consequently, the calculated low η_{sn}

efficiencies indicate losses mainly in the inlet section of the mixing chamber, where, due to the phenomena occurring there, including dilution-compaction waves, there are areas of most significant losses.

TABLE 5.3: Optimized ejector component efficiencies

Case	**Component efficiency**				
	η_{mn}	$\eta_{mn,hyp}$	η_{sn}	η_{mix}	η_{dif}
MC-1 150 kW	0.97	0.99	0.45	0.90	0.97
MC-1 170 kW	0.97	0.92	0.57	0.95	0.91
MC-2 200 kW	0.97	0.93	0.45	0.94	0.93
MC-1 + MC-2	0.97	0.99	0.45	0.95	0.91
MC-3 STC	0.95	0.90	0.57	0.92	0.99
MC-3 HTC	0.97	0.94	0.45	0.94	0.91
MC-4	0.95	0.99	0.99	0.97	0.92
MC-5	0.95	0.99	0.99	0.98	0.90

The values of the ejector component efficiencies optimized for MC-1 170 kW series showed the most significant difference from those optimized for case MC-1 + MC-2. However, in contrast to the other measurement series, in the case of the MC-1 170 kW series, vapor superheating at the motive nozzle inlet was very low.

Another interesting observation is the difference between η_{sn} for two measurement series from the MC-3 campaign differing in parameters at the suction nozzle inlet. For the STC series, the lower evaporator pressure, 0.55 bar, was necessary to achieve the 6°C/12°C standard chilled water parameters, resulting in lower pressure at the inlet of the ejector suction nozzle. Then η_{sn} was of 0.57. For high-temperature cooling (HTC), where the pressure at the inlet of the suction nozzle was slightly higher, around 0.75 bar, the calculated efficiency was 0.45. This revealed a strong influence of the boundary conditions and the isentropic efficiency of the suction nozzle η_{sn}.

The component efficiencies calculated for the MC-4 and MC-5 test series measurements show much higher values for the isentropic efficiency of the suction nozzle η_{sn}. However, both cases are significantly different from the conditions of the measurements in the previous test campaigns. In series MC-4, a wide range of ejector motive inlet temperatures was recorded for R1233zd(E) as a refrigerant. The large vapor superheating of refrigerant was obtained at both ejector inlets. In the case of the MC-5 measurement series case, the refrigerant used was R1234ze(E), which is a proven refrigerant in ejector refrigeration systems and shows high application utility under the propulsion conditions studied.

The calculated characteristic operating parameters of the supersonic ejector were compared with experimental results for each series of measurements. The measurement results and the computational model allowed the component efficiency map to be applied as a function of the operating parameters of the ejector or the entire system. However, in this work, fixed values for the ejector component efficiencies were used to demonstrate sufficient versatility of the model for design purposes.

Effect of condensation temperature on mass entrainment ratio

In Fig. 5.5, MER resulting from the model was compared with the experimental data for the MC-1, MC-2, and MC-3 test campaigns of the ejector refrigeration system driven by the waste heat of 200 kW.

The results in the MC-1 measurement campaign were obtained for the non-nominal load of the refrigeration system and the high-temperature cooling 16°C/19°C. For the 150 kW measurement series, the MER value of 0.12 ± 0.001 was obtained under on-design conditions. The critical point was at a condensation temperature value around 20°C. A very steep operating characteristic was observed under subcritical operating conditions. After increasing the driving heat of the ejector system to 170 kW, the performance of the ejector improved, reaching the MER value of 0.16 ± 0.001 under on-design conditions. A wider operating range of the ejector was achieved, which reached the critical point at the condensation temperature of 22°C.

After the changes in the geometry of the ejector and the modification of the heating system to approach the nominal driving heat of 200 kW, the MC-2 measurement campaign was carried out. Under nominal conditions, the ejector operated with the MER value of 0.24 ± 0.001, and the curve inflection point fell at a condensation temperature of about 25°C. The ejector stopped working for a temperature of 31°C. In the MC-2 measurement campaign, testing the ejector under standard cooling conditions was impossible due to the reverse flow in the ejector.

Then, another cooling system modification described in Chapter 3.4 was performed. A recuperator was withdrawn from the refrigeration system, reducing the pressure loss downstream of the ejector and limiting the required ejector compression ratio. As a result, in the MC-3 measurement campaign for high-temperature cooling (HTC), the MER was improved to 0.28 ± 0.001 under critical operating conditions. The critical point was again at a temperature of about 25°C. Tests were also successfully conducted under standard cooling conditions (STC). Under on-design operating conditions, a MER of 0.15 ± 0.001 was obtained, lower than the value expected in the research work. The on-design operation point was at the temperature of about 27.5°C, close to the expected value.

As can be seen in Fig. 5.5 for most of the results obtained through experimental measurements, it was possible to achieve high convergence in the computational model results. The exceptions are the measurement points received for the 150 kW series in the measurement campaign MC-1, where the ejector model no longer predicted its operation in the subcritical region, and the last points in the 170 kW series and the 200 kW series in the measurement campaign MC-2, where the computational model also already indicated backflow in the ejector. In those cases, the model predicted the extinction of the ejector earlier than it occurred in the tests. However, during the tests, the value of MER for those points was already negligible and insignificant from the perspective of the cooling capacities achieved.

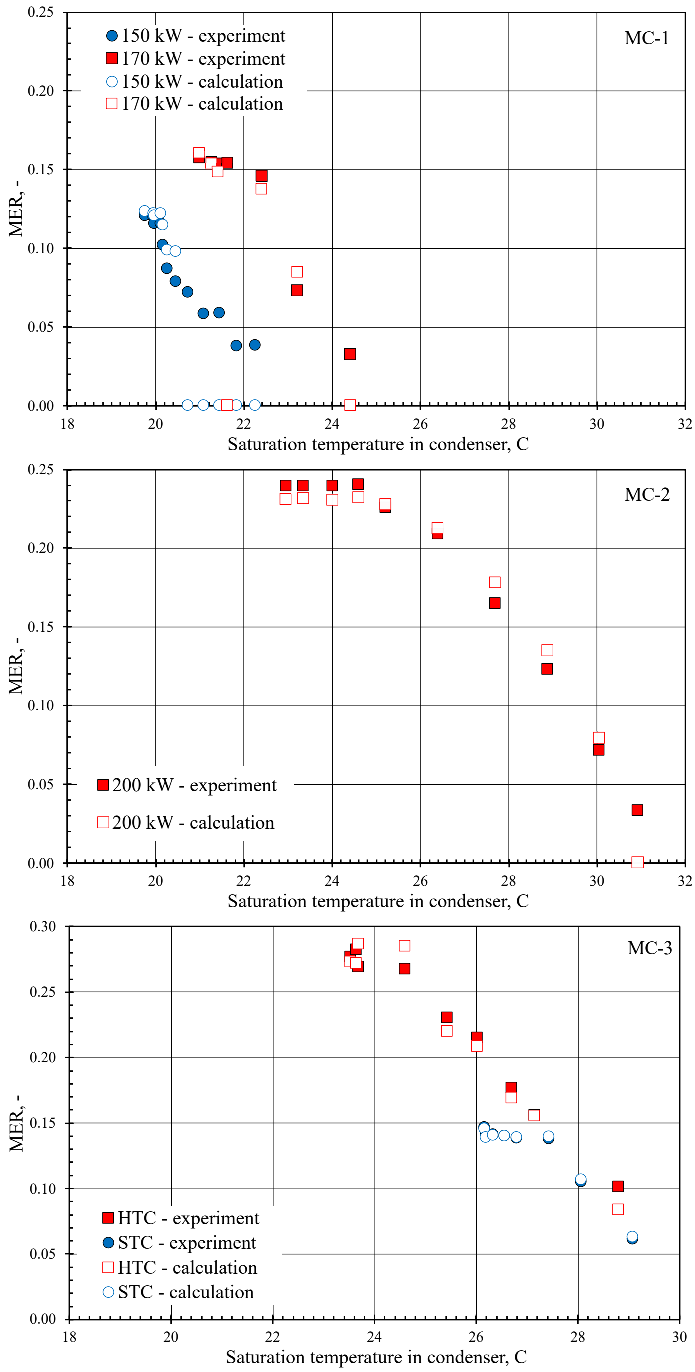

FIGURE 5.5: MER of the ejector in a function of the condensation temperature for MC-1 to MC-3 test campaigns of experimental tests (experiment) compared with the model results (calculation)

In Fig. 5.6, the relative discrepancies in the estimation of MER are presented for the MC-1 and MC-2 test campaigns for two approaches of the component efficiencies estimation. The first one, where the component efficiencies were estimated separately for each series of measurements, i.e., 150 kW series, 170 kW series, and 200 kW series. It is presented as white poles in the figure. In the second approach, the ejector component efficiencies indicated in Table 5.3 as MC-1 + MC-2 were used for calculations. It is presented as black poles in the figure.

For 150 kW series and the component efficiencies MC-1 + MC-2, the relevant discrepancy was obtained for the first four operating points, where the ejector was operating under on-design or close to the on-design conditions, and the resulting δ_{MER} ranged from 3.3% to 5.9%. After that, the model overestimated three operating points at off-design conditions, which corresponded to a condensation temperature of 20.2°C, 20.3°C, and 20.5°C, where δ_{MER} was 13.6%, 15.9%, and 26.7%. For the five final operating points, the model showed the backflow mode of the ejector, whereas, in the performed tests, the system was still operating at low capacity.

The results slightly improved in the second approach, where ejector component efficiencies were explicitly optimized for 150 kW series. The estimated MER was again slightly overestimated for the first four operating conditions, where δ_{MER} ranged from 1.7% to 5.4%. The accuracy in the first three points of the subcritical region was marginally upgraded, and the relative error ranged from 12.45% to 24.4%.

170 kW series had the largest discrepancy between the model and the test results. The model overestimated MER for the first four operating conditions, simultaneously predicting the off-designed operation mode of the ejector while the on-design conditions actually occurred. The δ_{MER} for those points ranged between 14.2% and 26.1%. According to the computational model, refrigerant was no longer entrained through the ejector suction nozzle for the final three operating points. In the performed tests, the ejector characteristic had a smoother slope. A notable change occurred in the case of calculations with component efficiencies optimized specifically for the series, where the model calculations were more adjusted to the experimental results. Even though the model still predicted the off-design operation of the ejector before reaching critical pressure during experimental tests. In that range, δ_{MER} was between −3.0% and 1.7%, except a point corresponding to the temperature 21.6°C, where the model showed no suction of the ejector. MER estimation for points 6 and 7 was more accurate, and δ_{MER} was between −5.6% and 16.1%, respectively. In the last case of this series, the model prematurely showed the backflow mode of the ejector.

The apparent mismatch in results obtained by the model with component efficiencies MC-1 + MC-2 may have had a cause in the ejector motive nozzle inlet parameters. The measurement points recorded at the motive nozzle inlet were close to the saturation line, while pronounced vapor superheating was observed for the 150 kW and 200 kW series. Due to the higher number of measurements made in the series of 150 kW and 200 kW, the combined MC-1 + MC-2 ejector component efficiencies were optimized mainly considering the accuracy of MER estimation for the 150 kW and 200 kW

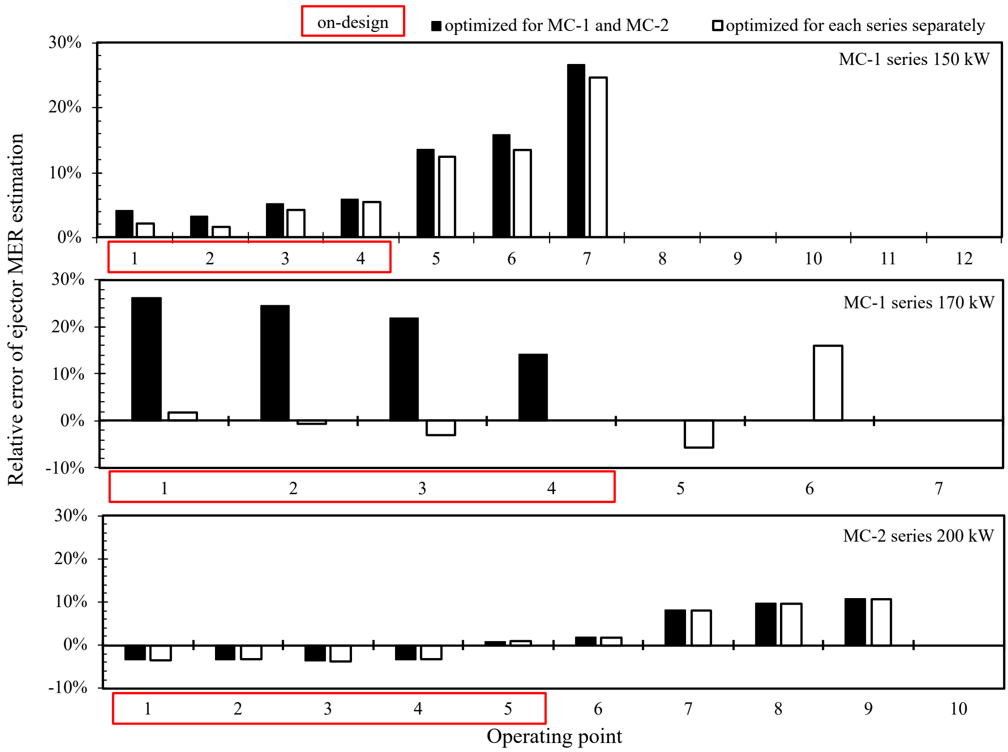

FIGURE 5.6: Relative discrepancy in the MER estimation for the MC-1 and MC-2 test campaigns for two sets of ejector component efficiencies

series. Thus, the accuracy of MER estimation for the 170 kW series was visibly lower. This demonstrates the need to optimize the component efficiencies for similar ejector operating conditions.

For the MC-2 200 kW series, the best accuracy of the model was achieved when the operating conditions corresponded to the nominal parameters of the ejector system. In the on-design operating mode of the ejector, thus for the condensation temperatures up to 25°C, the MER value was underestimated from around 0.24 to the level of around 0.22, which corresponded to δ_{MER} ranging from −9.7% to −10.1%. After crossing the critical pressure under off-design operating conditions, the MER was calculated with high accuracy, which corresponded to δ_{MER} ranging from −5.4% to 3.1%, except for the last operating point at condensation temperature 31°C, where in the performed tests low suction was still generated by the ejector and the backflow mode was indicated by the model. After using ejector component efficiencies optimized specifically for MC-2 200 kW series, an improvement was reached for the on-design operation mode of the ejector, where the MER was slightly underestimated and δ_{MER} fluctuated between −3.7% and −3.3%. Also, a satisfying improvement was achieved in the subcritical region where the relative discrepancy ranged from 0.9% to 10.8%, except for the last point, where δ_{MER} was 20.2%. In this case, however, the result can also be considered sufficiently accurate due to the very small MER of the ejector measured just before the entrainment was extinguished, amounting to just 0.03.

The results above suggest that it is possible to achieve sufficient model accuracy with constant ejector component efficiencies. However, experimental results with similar operating parameters, particularly superheating at the inlets of the ejector, should be selected to estimate the component efficiencies.

In Fig. 5.7, the relative error of MER estimation for measurements from the MC-3 test campaign is presented. For the STC series, the estimation error of the MER using the computational model ranged from -0.7% to 3.0% and was the highest for the last point measured in the off-design operation area. For high-temperature cooling conditions, the average error in the MER estimation was 5.3%, ranging from -4.6% to 6.5%. A significant MER estimation error -17.2% was registered for the last operating point measured in the off-design operation area just before the backflow appeared. This was already an insignificant operating point considering the efficient performance of the refrigeration system. The model results obtained for the MC-3 measurement campaign confirmed the usefulness of the developed ejector model.

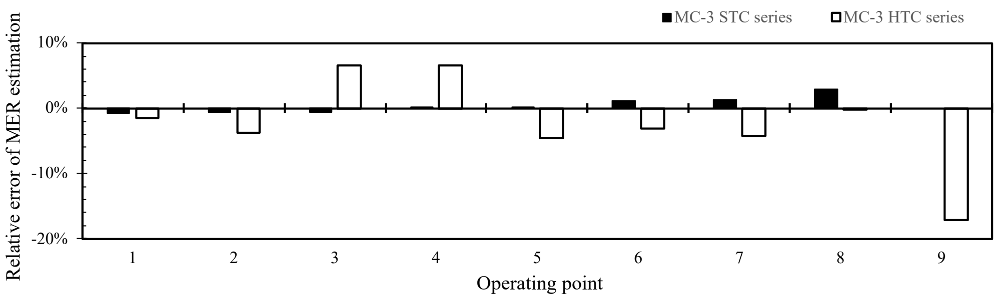

FIGURE 5.7: Relative discrepancy in the MER estimation for the MC-3 test campaign with two series of experiments

The ejector MER in the cooling system driven by waste heat 600 kW

Two measurement campaigns, MC-4 and MC-5, were carried out for the 600 kW waste heat-driven ejector refrigeration system, in which two working fluids, R1233zd(E) and R1234ze(E), were tested. As mentioned in Chapter 3.4 in the tests of the larger prototype, due to the unstable operation of the waste heat source, it was impossible to obtain complete operating characteristics of the ejector unit in campaign MC-4 and the single ejector in campaign MC-5. In both cases, several measurement points with boundary parameters were recorded at the ejector inlets and outlet.

The results of the measurements in the MC-4 test campaign showed a maximal MER of 0.32 ± 0.001 obtained for the operating point, where the driving waste heat was of 493.6 ± 2.1 kW, p_{mn} of 3.70 ± 0.04 bar(a), $\Delta T_{sh,mn}$ of 45.0 ± 0.5 K, p_{sn} of 0.60 ± 0.01 bar(a), $\Delta T_{sh,sn}$ of 11.4 ± 0.2 K and p_{out} of 1.46 ± 0.02 bar(a). For these parameters, the condensation temperature of 23.4 ± 0.1°C was reached. This showed that for high-temperature waste heat, the ejector with R1233zd(E) as a working medium achieves high performance.

The resulting δ_{MER} obtained from the model calculations was marked on the $p-h$ diagram in Fig. 5.8, where the operating points on the motive nozzle of the ejector set are marked. The figure shows significantly higher MER estimation errors than those obtained in the previous measurement series, which ranged from −39.1% to 104.3%. This is due to the large spread of the ejector operating parameters and the inability to adjust the ejector component efficiencies for all the operating parameters studied. In addition, the highest errors in the model calculations correspond to the lowest experimentally measured MER values, indicating that the ejector was most likely at the end of the subcritical operating area. For the four operating points where the measured MER exceeded 0.2, the error in estimating this parameter using the computational model was about 20%. The model inaccuracy was also influenced by the measurements made under unstable operating conditions of the waste heat source. In addition, it should also be taken into account that the mass flow rates on the motive and suction nozzle of the ejectors were measured collectively for a set of 3 compressing devices. Inaccuracies in their design, or in the design of the cooling installation itself, may have also contributed to the uneven distribution of these mass flow rates across the individual ejector. These results indicate that the model should be calibrated for a smaller operating area corresponding to similar parameters at the ejector inlets.

After the changes were applied to the heating system and the refrigerant was changed to R1234ze(E), it was possible to stabilize the refrigeration system and record six measurement points for standard cooling conditions in the evaporator. The MER values ranging from 0.14 ± 0.001 to 0.25 ± 0.001 was obtained. The highest value was obtained for the following supply conditions: waste heat transferred in the generator 570.6 ± 1.9 kW, superheat at the motive nozzle equal to 7.2 ± 0.4 K, and superheat at the suction nozzle equal to 5.7 ± 0.1 K, which was not surprising given the design of the ejector for a slight superheat of vapor at the inlet to the nozzles. It is worth noting that this operating point corresponded most closely to the rated operating conditions of the refrigeration system. Before the refrigerant change to high-pressure R1234ze(E), the MER value was two times lower for the ejector operating under similar operating conditions with R1233zd(E) as the working fluid. It can be observed in Fig. 5.5, where the results were presented for MARANI CHILLER 200 operating in the MC-3 test campaign in STC measuring series, where the MER values of about 0.15 were obtained.

Calculations were again performed using the 0-D supersonic ejector model for the recorded measurement points. The relative errors between the calculated and experimentally measured values are again shown in the $p-h$ diagram in Fig. 5.9, where the parameters on the ejector motive nozzle are marked. A very high accuracy of MER estimation was obtained for all tested operating points, for which the discrepancy

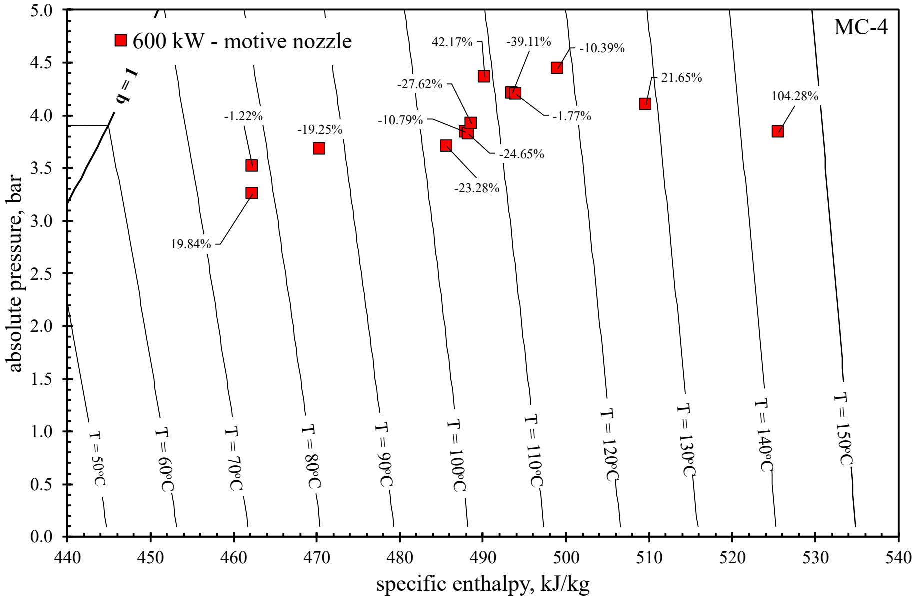

FIGURE 5.8: Relative discrepancy in the MER estimation for the MC-4 test campaign marked on ejector motive nozzle inlet parameters on the $p-h$ diagram

was estimated in the range from -8.2% to 2.4%. Therefore, it can be concluded that for R1234ze(E), which is a high-pressure medium, optimization of the component efficiencies of the ejector model is possible for a wide range of operating parameters. In addition, in this case, small fluctuations in the measured pressure do not significantly affect the accuracy of the measurements, and therefore, the computational results are more reliable. Moreover, it can be noted that with a stable heating system and, consequently, stable operation of the refrigeration system, it is possible to accurately calibrate the ejector model.

Effect of condensation temperature on ejector pressure ratio

In Fig. 5.10, the p_{ratio} of the ejector as a function of the condensation temperature is presented for measurement campaigns MC-1 to MC-3. In this figure, the model results are compared with the test results. The experimental results obtained for the 150 kW series in the MC-1 test campaign indicated a value of ejector p_{ratio} of about 1.6 for all tested points, which resulted from the narrowing of the tested operating area. In the case of the 170 kW series in the MC-1 test campaign, the ejector pressure ratio was 1.61 ± 0.04 and 1.68 ± 0.04. After modifying the geometry of the mixing chamber and the diffuser of the ejector and ensuring nominal waste heat parameters in 200 kW series in the MC-2 test campaign, the ejector was tested over a broader range of condensation pressures, which corresponded to p_{ratio} values ranging from 1.83 ± 0.04

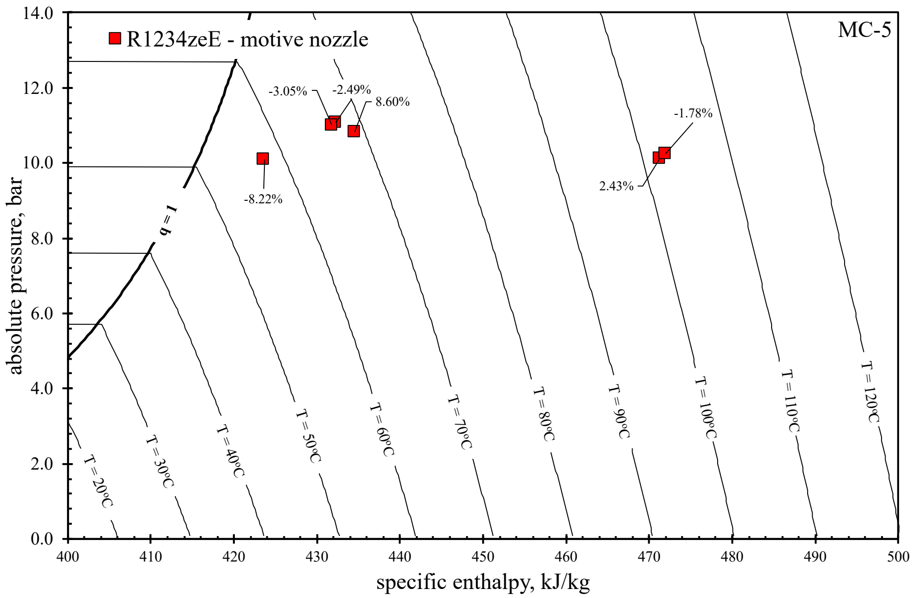

FIGURE 5.9: Relative discrepancy in the MER estimation for the MC-5 test campaign marked on ejector motive nozzle inlet parameters on the $p-h$ diagram

to 2.23 ± 0.05. The elimination of pressure drops at the ejector outlet allowed the ejector to achieve sufficient compression ratio values to operate under standard chilled water temperatures in the STC series of the MC-3 test campaign and compress the refrigerant from the evaporation pressure of about 0.55 bar(a) to saturation pressure in the condenser for a condensation temperature range of 26.2 ± 0.1°C and 29 ± 0.1°C. This corresponded to the pressure ratio range between 2.42 ± 0.07 and 2.74 ± 0.08. In that case, the parameters at the ejector motive nozzle were stable, resulting in a good representation of the compression characteristics as a function of the condensation temperature.

In the MC-3 measurement campaign for high-temperature cooling (HTC), pressure ratio values in the range of 1.66 ± 0.04 and 1.96 ± 0.05 were achieved. The results did not form an ascending characteristic due to fluctuations in temperature and pressure at the ejector motive nozzle resulting from the instability of the waste heat source operation in the series of measurements in question.

As shown in Fig. 5.10, the computational model of the ejector allowed for the correct representation of the ejector pressure ratio in key operation areas for all test campaigns. The exceptions were, again, the off-design region of the 150 kW series in the MC-1 campaign, where the model already showed the decay of the ejector operation, and the last measurement points in the 170 kW series and 200 kW.

In Fig. 5.11, the relative discrepancies in the estimation of p_{ratio} are presented

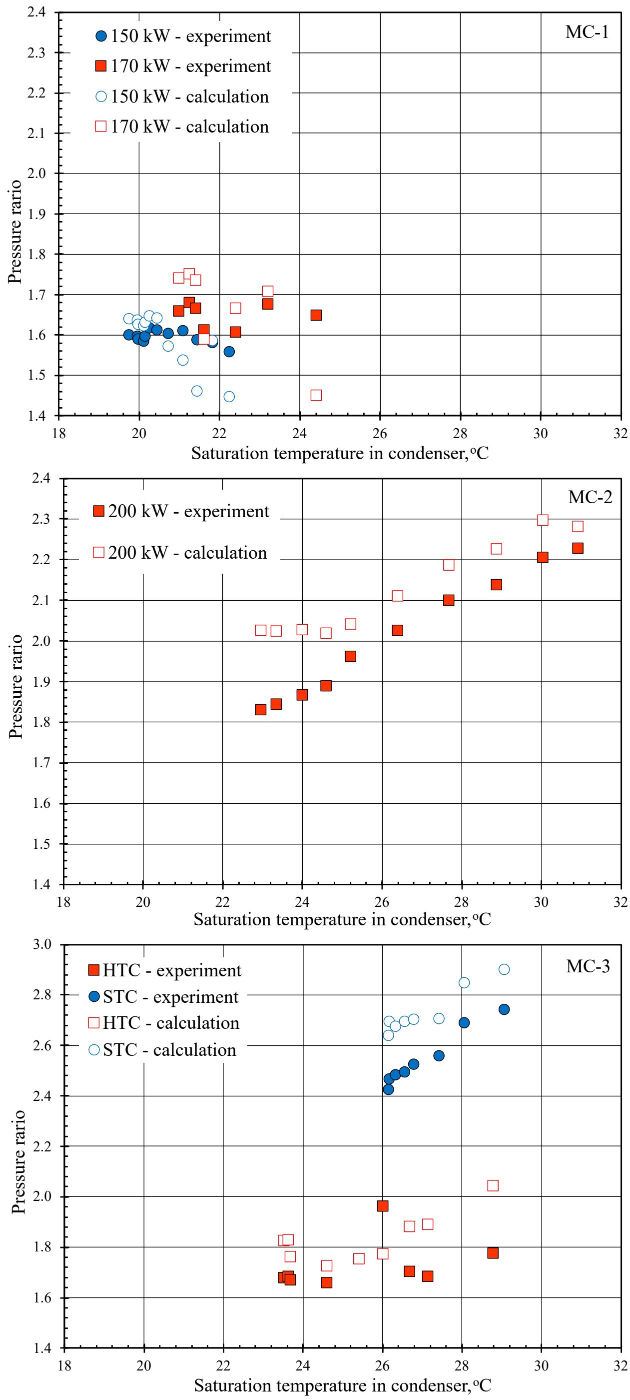

FIGURE 5.10: Pressure ratio of the ejector in a function of the condensation temperature for the MC-1 to MC-3 test campaigns of (experiment) compared with the model results (calculation)

for the MC-1 and MC-2 test campaigns for two approaches of the ejector component efficiencies estimation. The first one, where the component efficiencies were estimated separately for each series of measurements, i.e., 150 kW series, 170 kW series, and 200 kW series. It is presented as a white poles in the figure. The second approach assumed the same ejector component efficiencies for all operating points from the MC-1 and MC-2 test campaigns. It is presented as black poles in the figure. The model accuracy for the p_{ratio} estimation was satisfactory, considering an average relative error of 4.4% for component efficiencies MC-1 + MC-2 and 4.5% for the second approach.

For the results obtained for the 150 kW series, p_{ratio} was slightly overestimated in the area of the ejector on-design operation and close to the critical pressure. However, the δ_{p_ratio} did not exceed 2.6%. It corresponded to the points where MER was predicted with acceptable accuracy. In the subcritical region, the p_{ratio} was underestimated up to −9.2% except for the penultimate operating point, where the result covered the measured value. The results confirmed that the ejector outlet pressure was underestimated, which may have been the reason for the premature prediction of backflow in the suction nozzle. The results were almost the same in the case of the second approach of the calculated ejector component efficiencies. They were insignificantly improved, but the trend remained the same.

For the 170 kW series, the calculated pressure ratio was again overestimated for operating points before the critical pressure for both sets of ejector efficiencies. The δ_{p_ratio} was 4.9%, 4.2%, and 4.2%, respectively, for the points that occurred in this section of ejector characteristics. In the ejector off-design operation area, the accuracy of the p_{ratio} calculation differed for the two sets of ejector component efficiencies. In the case of the ejector component efficiencies optimized collectively for all operating conditions from the MC-1 and MC-2 test campaigns, δ_{p_ratio} was decreasing in the range from 4.0% to −4.6% with increasing condensation temperature. When using component efficiencies explicitly optimized for the 170 kW series, a more accurate estimation was reached for the operating points no. 4 and no. 6, whereas for points no. 5 and no. 7, the relative error was higher than in the first approach.

For the 200 kW series, p_{ratio} was estimated almost uniformly for both sets of ejector component efficiencies. In the ejector on-design operation area, the constant value of the ejector compression ratio was predicted, while in the performed tests, the ratio was trending upward. For that reason, δ_{p_ratio} was decreasing in this area from 11.0% to 7.2% for the component efficiencies optimized for all the operating conditions and from 10.7% to 6.9% for the component efficiencies dedicated to 200 kW series. The subcritical work area had a constant p_{ratio} estimation relative error of 4.1%. An exception was for the last point in the case of the component efficiencies estimated for all operating points when the model underestimated the ejector outlet pressure and, consequently, the backflow mode was indicated.

In Fig. 5.12, the relative error of p_{ratio} estimation for measurements from the MC-3 test campaign is presented.

For the STC series, the calculated p_{ratio} was overestimated for all measurements

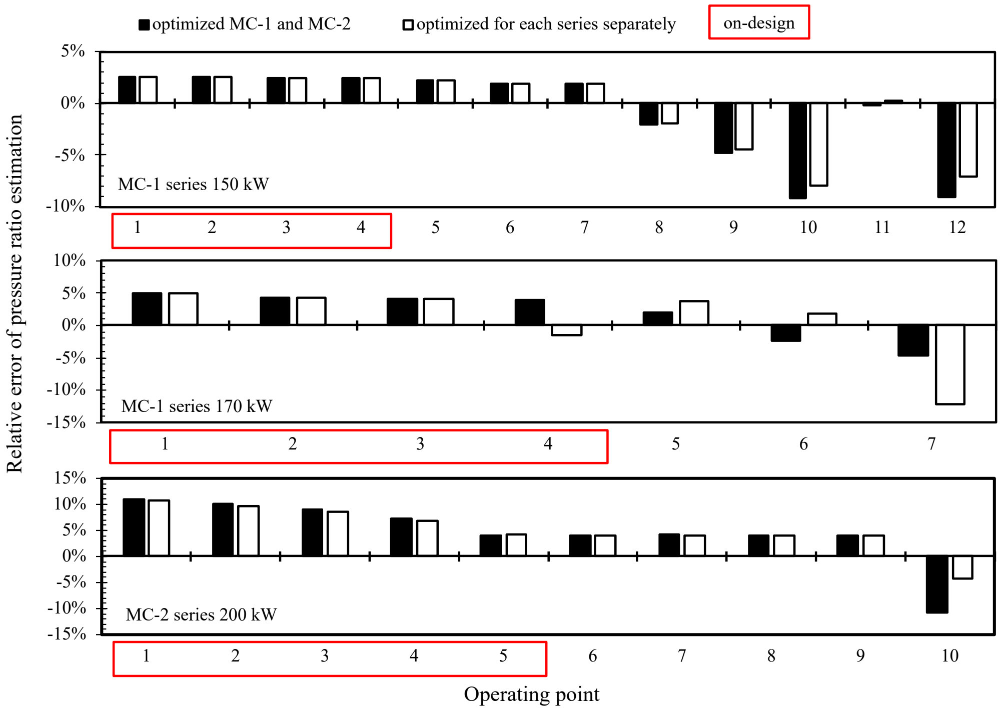

FIGURE 5.11: Relative discrepancy in the p_{ratio} estimation for the MC-1 and MC-2 test campaigns for two sets of ejector component efficiencies

with an average estimation error of 7.3%, not exceeding 10% for any operating point. For high-temperature cooling conditions, the average error in p_{ratio} estimation was 8.3% ranging from -9.7% to 15.1%. Significant p_{ratio} estimation errors of 12.2% and 15.1% were registered for the last two operating points measured in the subcritical area just before the backflow appeared. However, these were already insignificant operating points considering the efficient performance of the refrigeration system. Summarizing the model accuracy in estimating this working parameter for measurements performed in MC-3, it can be concluded that the accuracy in estimating the pressure ratio is satisfactory. This is important because the model was calibrated to minimize the MER relative error.

The ejector pressure ratio in the cooling system driven by waste heat 600 kW

As for the ejector mass entrainment ratio, the calculated pressure ratio was also compared with the experimental results for the MC-4 and MC-5 measurement campaigns carried out on a refrigeration system driven by the 600 kW waste heat.

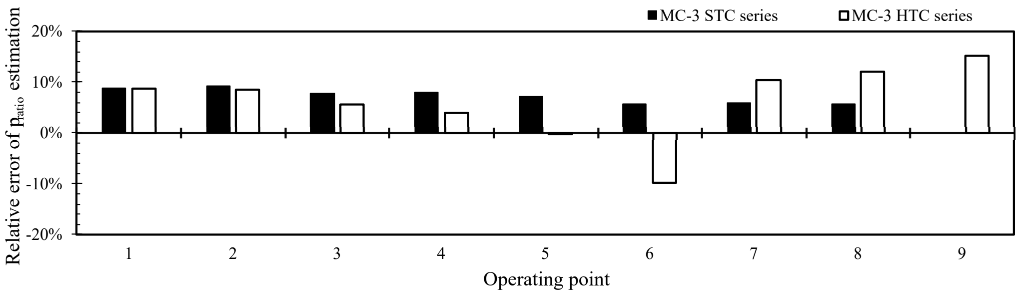

FIGURE 5.12: Relative discrepancy in the p_{ratio} estimation for the MC-3 test campaign with two series of experiments

In the MC-4 campaign, due to registering measurement points with a large span of superheat on the ejectors motive nozzles, a large span of measured pressure ratio was also registered, ranging from 2.33 ± 0.06 to 3.35 ± 0.10. For the measurement point with the highest efficiency of the ejectors, corresponding to the MER value of 0.32, the pressure ratio was 2.33 ± 0.06. The maximum pressure ratio was obtained for points where the three ejectors were no longer operating with the high MER values. Likely. the ejector operated under off-design conditions at the above points.

The $\delta_{p_{ratio}}$ values obtained from the model calculations are presented on the $p-h$ diagram in Fig. 5.13, where the operating points at the motive nozzle inlet of the ejector set are marked. Despite significant MER estimation discrepancies discussed above, the indicated errors in the estimation of p_{ratio} show a good representation of this parameter by the computational model. The relative error was, on average, 1%, not exceeding the relative error of 7.2%.

Six measurement points were obtained for standard chilled water parameters after changing the refrigerant to R1234zd(E) in the MC-5 measurement campaign. The measured ejector pressure ratio ranged from 1.95 ± 0.01 to 2.05 ± 0.01, showing this refrigerant superiority over R1233zd(E) for ejector applications. Its thermodynamic parameters result in the fact that, despite higher pressures corresponding to the same saturation temperatures in the evaporator and condenser, the ratio of these pressures in the case of R1234ze(E) is lower, which means that the ejector has less compressing work to do, thus increasing its efficiency under similar operating parameters. Calculations of the p_{ratio} by the 0-D ejector model showed perfect accuracy with an average relative error close to 0%.

Effect of condensation temperature on ejector efficiency

The ejector efficiency was the last of the parameters compared to determine the model accuracy. In Fig. 5.14, the efficiency of ejector η_{ej} is presented as a function of the condensation temperature for experimental measurements along with the model calculations.

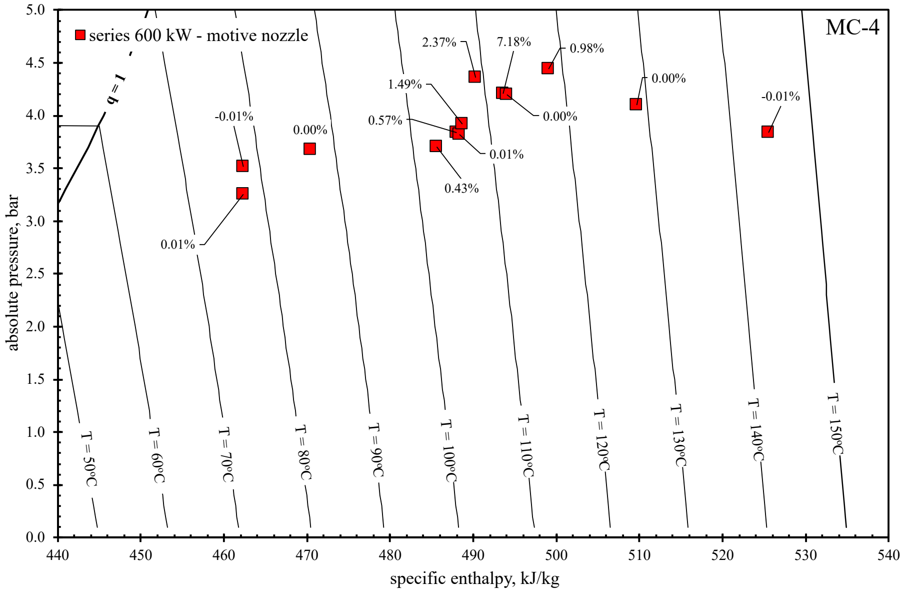

FIGURE 5.13: Relative discrepancy in the p_{ratio} estimation for the MC-4 test campaign marked on ejector motive nozzle inlet parameters on the $p-h$ diagram

For the 150 kW series in MC-1, the on-design operating area of the refrigeration system corresponded to the area of constant efficiency of the ejector. However, the ejector operated at conditions deviating from the nominal values, reaching the ejector efficiency of 0.06 ± 0.01, which decreased when the off-design operating area was entered. For the 170 kW series in MC-1, the ejector efficiency was of 0.09 ± 0.01 in the on-design operation area. After changing the geometry of the ejector and achieving the nominal operating parameters for high-temperature cooling in the MC-2 measurement series, the ejector achieved the highest efficiency for the first operating point in the off-design operating area, which was 0.16 ± 0.01. Similar values of the HTC series in the MC-3 test campaign. For this case, it was impossible to adequately represent the efficiency as a function of saturation temperature in the condenser due to the variation of parameters on the ejector motive nozzle inlet. For the standard cooling variant (STC series), the maximum efficiency of the ejector was obtained at 0.13 ± 0.01.

In Fig. 5.15, the relative discrepancies in the estimation of η_{ej} are presented for the MC-1 and MC-2 test campaigns for two approaches of component efficiencies estimation. The first one, where the component efficiencies were estimated separately for each series of measurements, i.e., 150 kW series, 170 kW series, and 200 kW series. The second approach assumed the same ejector component efficiencies for all the calculations from the MC-1 and MC-2 test campaigns.

The consistency of the model with the experimental results was the same as for the

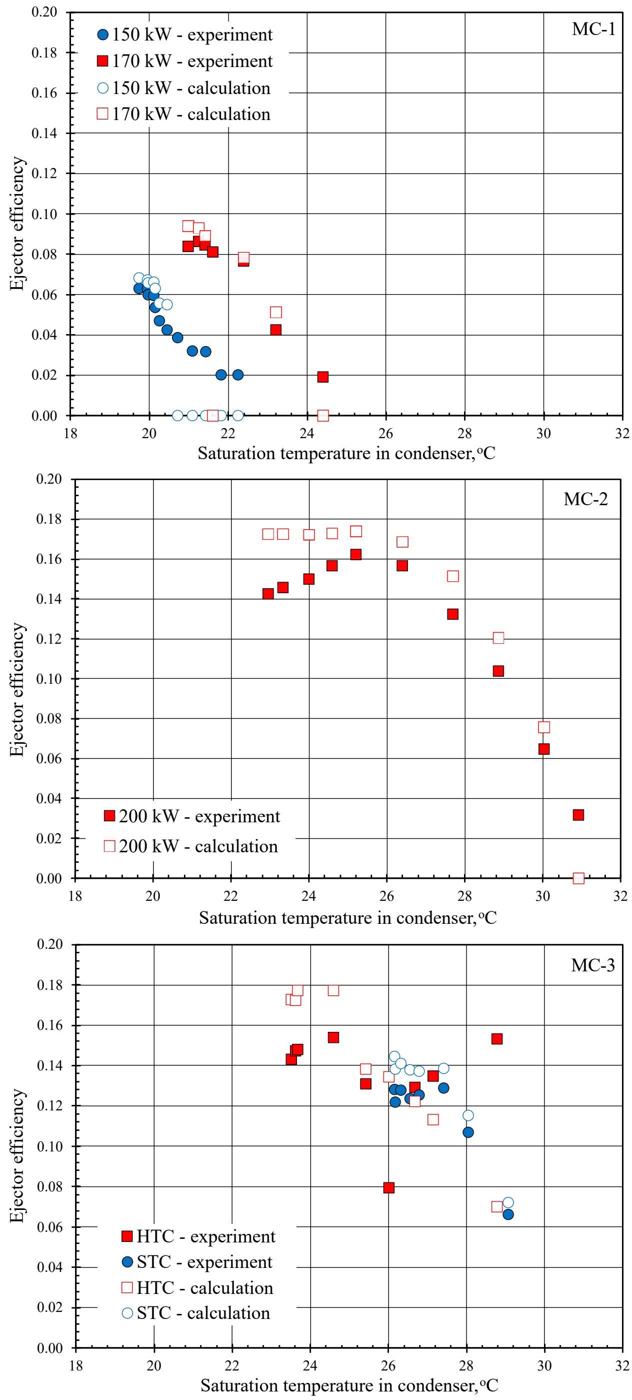

FIGURE 5.14: Efficiency of the ejector in a function of the condensation temperature for the MC-1 to MC-3 test campaigns of experimental tests (experiment) compared with the model results (calculation)

accuracy of the MER determination due to its use in calculating η_{ej}. For 150 kW series in MC-1, η_{ej} was evaluated with high accuracy for points that occurred in the ejector critical area and close after crossing the critical pressure. It corresponded to points 1 to 4 of the considered series. The values were overestimated from 7.5% to 11.7% of δ_{η_ej} with insignificant improvement after optimizing the ejector efficiency for the selected series. With the decreasing suction flow rate of the ejector, the estimation accuracy fell to δ_{η_ej} in the range 17.9% to 31.7%. The η_{ej} was finally zeroed out for the last five points according to the backflow mode prediction.

The η_{ej} was highly overestimated in the on-design operation area for 170 kW series in MC-1 calculated with the ejector component efficiencies optimized collectively for MC-1 and MC-2, and the relative error was up to 38.5%. The efficiency was not calculated for the last three points due to the extinguishing of the ejector operation. The dedicated component efficiencies improved model prediction and were below 12% in the on-design operation region. Moreover, η_{ej} was predicted for a condensation temperature of 22.4°C and 23.2°C with a relative error of 1.9% and 20.4%, respectively.

Similar to p_{ratio}, η_{ej} was estimated with a constant trend in the ejector on-design operation area for 200 kW series in MC-2, while the increasing trend occurred in the performed tests. The δ_{η_ej} was in the range from 3.9% to 13.8% for the component efficiencies optimized collectively in case MC-1 + MC-2 and from 10.4% to 21.0% the component efficiencies optimized for 200 kW series. The downward trend of η_{ej} was maintained in the subcritical region. However, values of this quantity were still overestimated. The relative error of ejector efficiency δ_{η_ej} was in the range from 0.5% to 7.1% for the component efficiencies optimized for all the operating cases from MC-1 and MC-2 and 7.3% to 26.5% for the component efficiencies optimized for 200 kW series. The decrease in the accuracy of the ejector efficiency estimation after optimizing the efficiency component efficiencies with respect to the MER value showed that the characteristics of MER and η_{ej} were not the same. Thus, adjusting the component efficiencies to MER increased the mismatch to the estimated ejector efficiency.

In Fig. 5.16, the relative discrepancies in the estimation of η_{ej} are presented for two measurement series conducted in the MC-3 test campaign. The variant for standard-temperature cooling (STC) yielded an average relative error of 10.2% in the ejector efficiency estimation. The obtained results were overestimated for all measured points, reaching a relative error of 7.5% to 13.5%. The highest error was observed in the on-design operation area, where the MER of the ejector was mapped with the highest accuracy. Nevertheless, the above results may be considered satisfactory. In the case of estimating the η_{ej} for the HTC series, estimation errors reached a high value, especially for points no. 6 and no. 9, where the discrepancies exceeded 50%. However, for points no. 6, no. 7, no. 8, and no. 9, it is apparent that the downward trend in the graph of the efficiency of the ejector was not preserved with the extinction of its operation, which was the case in the other measurement series. This can be observed in Fig. 5.14. This also suggests errors in the measurements for the above points or indeterminacy of the work parameters, which may be the reason for receiving such high calculation errors.

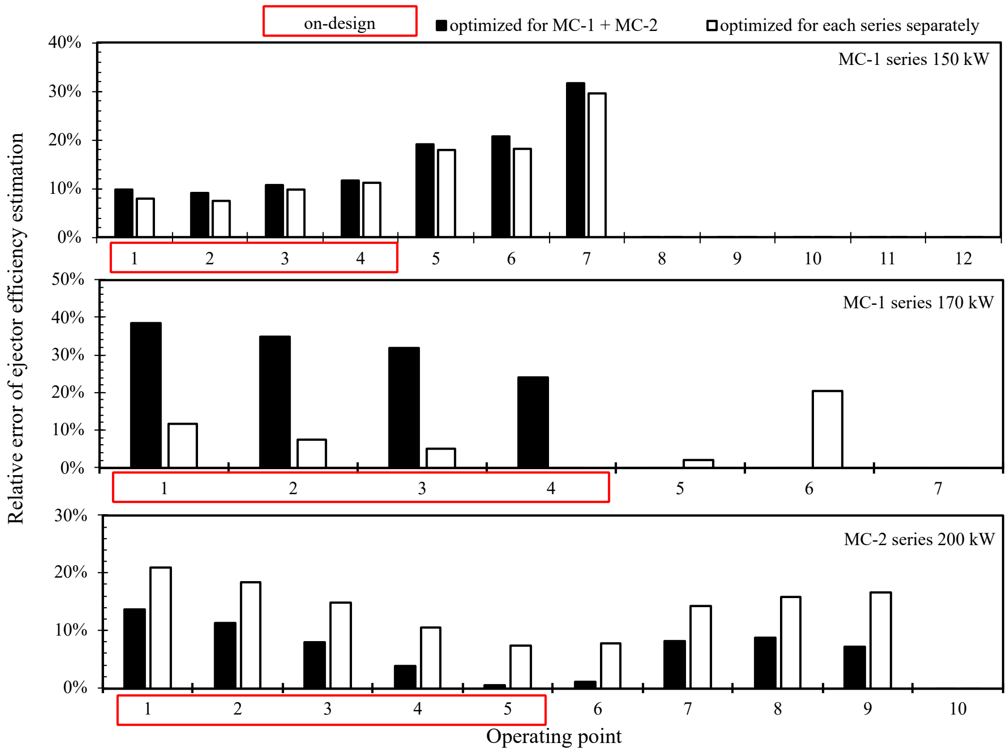

FIGURE 5.15: Relative discrepancy in the η_{ej} estimation for the MC-1 and MC-2 test campaigns for two sets of ejector component efficiencies

The ejector efficiency in the cooling system driven by waste heat 600 kW

Similarly to the previously considered ejector key parameters, the ejector efficiency was also calculated and compared with the experimental results from the MARANI CHILLER 600, within the MC-4 and MC-5 test campaigns.

In the MC-4 campaign, various measuring points were registered, and the ejector efficiency ranged from 0.05 ± 0.01 to 0.24 ± 0.01. The relative error in ejector efficiency estimation $\delta_{\eta_{ej}}$ obtained from the model calculations were presented on the $p-h$ diagram in Fig. 5.17, where the operating points at the motive nozzle of the ejector set are presented. As in the MER calculation, the model did not score well over such a wide range of operating parameters, influenced by the instability of the unit operation due to the heat source used. The relative error of ejector efficiency estimation was comparably high with the mistake of MER calculations. This resulted from the ejector efficiency definition presented in Eq. (4.61), which involves the MER value.

The efficiency of the ejector was also measured indirectly for tests in the MC-5 measurement campaign, where R1234ze(E) refrigerant was used. It was confirmed that the ejector operated efficiently under the tested conditions, achieving an efficiency of 0.12 ± 0.01 and 0.22 ± 0.01. It also confirmed the high accuracy of the calibrated

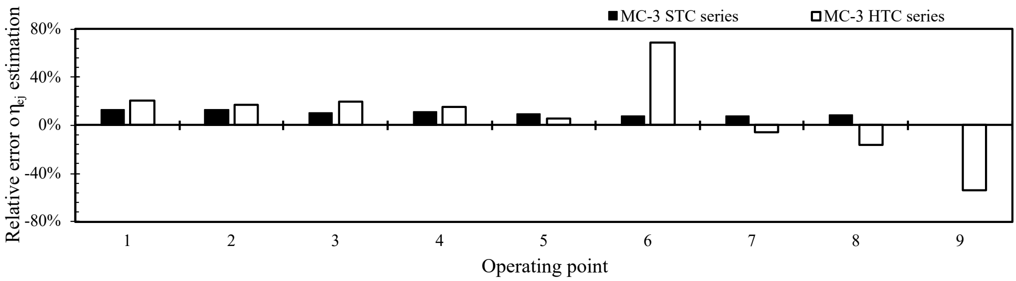

FIGURE 5.16: Relative discrepancy in the η_{ej} estimation for the MC-3 test campaign with two series of measurements

computational model in estimating the discussed parameter of the ejector operation. The results of the relative error in calculating the η_{ej} under the given operating conditions are shown in Fig. 5.18, where the $p-h$ plot shows the measurement points at the motive nozzle inlet of the ejector. As can be seen, the error range was between -6.4% and 9.9%, which is considered a satisfactory value.

A comparison of the crucial parameters of the ejector operation determined by experimental measurements with the results obtained with the 0-D model confirmed a satisfactory representation of the gas ejector operation. However, high sensitivity of the mathematical mode to the adopted ejector component efficiencies was observed. It was especially visible in the case of the R1233zd(E) refrigerant. Nevertheless, the model allows very fast recalculations of the ejector under well-recognized waste-heat parameters. Thus, it will enable MARANI Ltd. to accurately calculate repeatable and comparable waste heat sources such as air compressor plants.

5.2 Heat exchangers results

Similarly to the ejector, heat exchangers are also crucial elements in modeling an ejector refrigeration system. In the systems studied, all the heat exchangers used were compact plate heat exchangers, which were calculated using the LMTD model. To validate the computational models of the plate heat exchangers, experimental measurements were carried out on the ejector refrigeration unit driven by 200 kW of the waste heat from an air compressor oil system. For validation purposes, the measurements recorded in the MC-1 and MC-2 measurement campaigns were utilized due to the stable operation of the refrigeration systems as well as the waste heat source. Moreover, in that system configuration, all the plate heat exchangers, i.e., the preheater, generator, evaporator, condenser, and recuperator, were installed. The refrigeration system underwent various changes in further measurement campaigns, as described in Chapter 3.4. In the MC-1 and MC-2 measurement campaigns, the tests were carried out in 3 series: 150 kW, 170 kW, and 200 kW, and were numbered as follows: no. 1 through no. 12 for the 150 kW

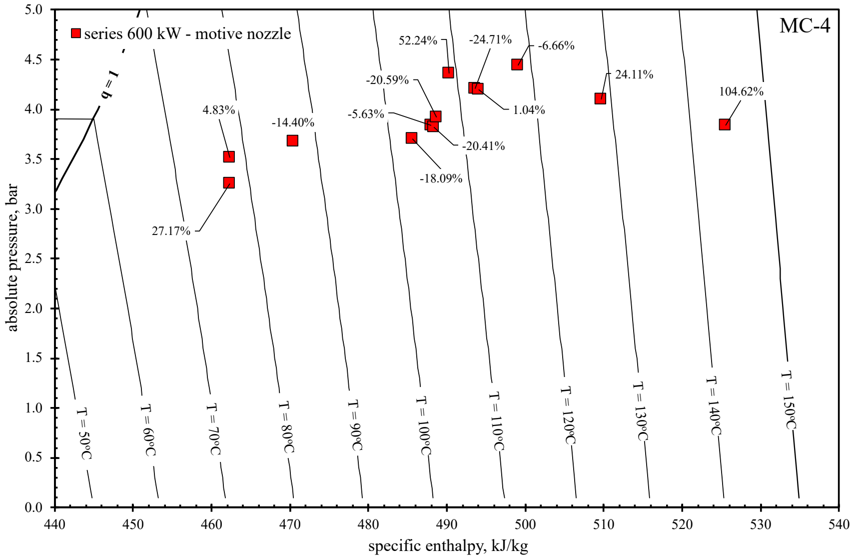

FIGURE 5.17: Relative discrepancy in the η_{ej} estimation for the MC-4 test campaign marked on ejector motive nozzle inlet parameters on the $p-h$ diagram

series, no. 13 through no. 19 for the 170 kW series, and no. 20 through no. 29 for the 200 kW series. For all heat exchangers, the results of the computational models were compared with experimental results for outlet temperatures and heat transfer rate transferred in the exchanger. In two cases, when the pressure measurement was performed upstream and downstream of the heat exchanger in the system, the results of the calculated pressure drop in the heat exchanger were also compared.

5.2.1 Validation of preheater model

The results of experimental measurements for the refrigerant preheater are rearranged in Table 5.4. On the cold side of the heat exchanger, the measurement of the refrigerant temperature was recorded with the help of temperature transmitters TT-7 and TT-8 according to the diagram of the refrigeration system shown in Fig. 3.2. To calculate thermodynamic parameters such as the specific enthalpy and the heat transfer rate transferred in the heat exchanger, pressure sensor PT-1 was used to measure the pressure downstream of the generator. On the hot medium side, hot water temperature measurements were recorded at the inlet and outlet of the preheater, which is indicated in the above system layout as the temperature sensors TT-hw2 and TT-hw3. On the refrigerant side, the mass flow rate measurement was used according to the FM-gen flow meter measurement, and on the hot water side, according to the FM-hw measurement. Because the pressure value upstream and downstream of the heat exchanger was not recorded, validation of the pressure drop was not undertaken.

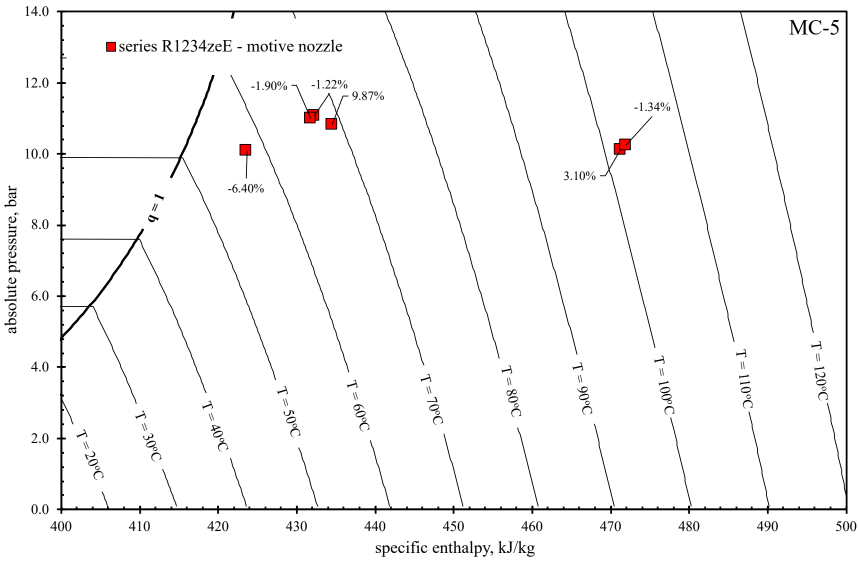

FIGURE 5.18: Relative discrepancy in the η_{ej} estimation for the MC-5 test campaign marked on ejector motive nozzle inlet parameters on the $p-h$ diagram

In the MC-1 and MC-2 measurement campaigns, the test points were recorded with pressure levels ranging from 2.79 ± 0.02 bar(a) to 3.87 ± 0.02 bar(a) on the refrigerant side. The refrigerant inlet temperature ranged from 42.1 ± 0.1°C to 52.1 ± 0.1°C, and the hot water temperature ranged from 51.5 ± 0.2°C to 63.9 ± 0.2°C. The heat transfer rate from hot water to refrigerant ranged from 6.3 ± 0.9 kW to 17.7 ± 1.3 kW. The measurement points at the inlet and outlet on the refrigerant side of the preheater are shown in the $p-h$ diagram on top of Fig. 5.19. In all cases, the heat exchanger was sufficient to reach the saturation parameters of the refrigerant at the heat exchanger outlet and even obtain the evaporation temperature.

Fig. 5.19 (bottom) shows the relative error in the estimation of the crucial operating parameters of the preheater. The relative error in estimating the outlet temperature of the refrigerant was within the limit of up to 0.1 K for all cases considered. This error is small primarily due to the achievement of the refrigerant saturation temperature; hence, it is not an essential parameter in the evaluation of the heat exchanger model. In this case, the hot water outlet temperature is a critical parameter in evaluating the model accuracy. The relative error in estimating this parameter was up to 0.2 K, confirming the model accuracy. The average error in calculating the heat transfer rate in the heat exchanger was 7.1%, falling within 5% to 9% overestimation, which can be considered satisfactory.

TABLE 5.4: Preheater experimental data from the MC-1 and MC-2 test campaigns

No.	t_{in}^{cold} °C	t_{out}^{cold} °C	t_{in}^{hot} °C	t_{out}^{hot} °C	$\dot{Q}$ kW
1	42.1	48.3	51.5	50.3	6.7
2	42.1	48.5	51.7	50.4	6.9
3	42.1	48.3	51.7	50.4	6.6
4	42.2	48.4	51.8	50.6	6.8
5	42.5	48.4	51.7	50.5	6.6
6	42.8	48.4	51.7	50.5	6.4
7	42.9	48.4	51.6	50.5	6.4
8	43.2	48.4	51.6	50.5	6.4
9	43.5	48.6	51.8	50.6	6.5
10	43.6	48.7	51.8	50.6	6.3
11	43.4	48.7	51.8	50.6	6.6
12	43.5	48.7	51.8	50.6	6.5
13	39.4	52.6	56.4	55.1	13.0
14	38.5	52.9	56.5	55.1	14.3
15	38.8	52.8	56.4	55.1	14.0
16	38.1	52.3	55.7	54.4	13.7
17	38.5	52.9	56.3	55.0	14.0
18	36.6	53.0	56.2	54.8	16.3
19	35.2	53.2	56.3	54.9	17.7
20	46.1	57.1	66.4	64.1	11.5
21	46.1	57.3	66.3	64.0	11.5
22	46.2	57.6	66.3	64.1	11.9
23	45.8	57.6	65.8	63.7	12.2
24	45.7	56.9	63.8	62.1	11.4
25	46.8	58.4	65.1	63.4	12.7
26	47.9	58.9	64.7	63.2	12.8
27	48.6	59.1	64.4	63.0	12.8
28	50.0	59.4	64.0	62.7	12.0
29	51.1	59.6	63.9	62.7	11.6

5.2.2 Validation of generator model

The experimental measurements for the generator are summarized in Table 5.5. On the cold side of the heat exchanger, the refrigerant temperature was measured using temperature transmitters TT-8 and TT-1, as shown in the refrigeration system layout in Fig. 3.2. Pressure transmitter PT-1, which measures the pressure downstream of the generator, was utilized to determine thermodynamic parameters like the specific enthalpy and heat transfer rate in the heat exchanger. On the hot medium side, the hot water temperature was recorded at the generator inlet and outlet using temperature sensors TT-hw1 and TT-hw2. Mass flow rates were measured using the FM-gen flow meter on the refrigerant side and the FM-hw measurement on the hot water side. Similarly to the preheater, the pressure was not recorded at the inlet of the generator, thus pressure drop validation was not performed.

Similarly to the preheater experimental results in the MC-1 and MC-2 measurement campaigns, the operating points were recorded with the pressure levels ranging from 2.79 ± 0.02 bar(a) to 3.87 ± 0.02 bar(a) on the refrigerant side. The refrigerant inlet temperature ranged from 49.7 ± 0.1°C to 61.0 ± 0.2°C, and the hot water temperature

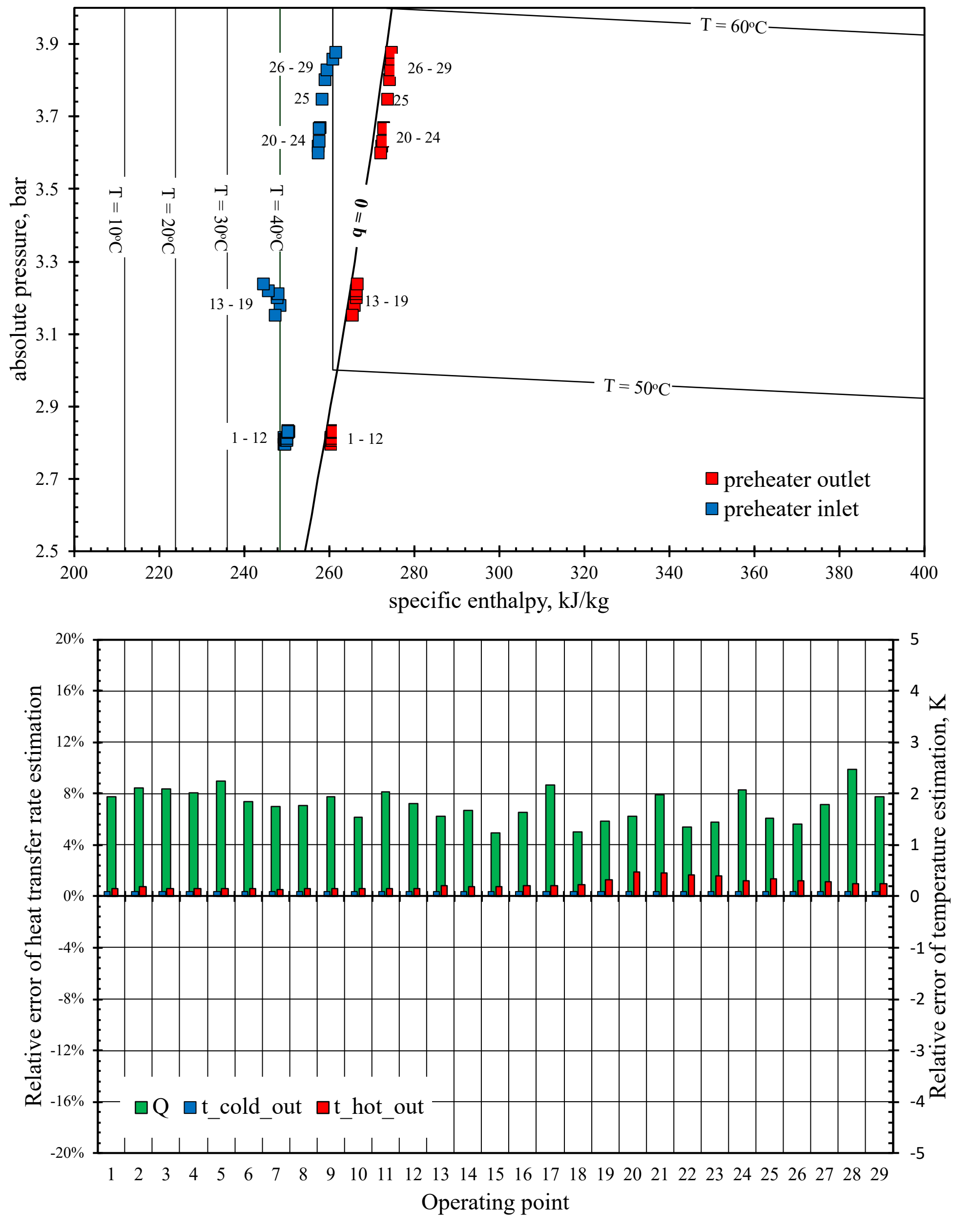

FIGURE 5.19: Preheater cold side inlet and outlet parameters from MC-1 and MC-2 presented on $p-h$ diagram (top) and the relative discrepancy in the preheater outlet temperatures and heat transfer rate estimation for all operating points (bottom)

TABLE 5.5: Generator experimental data from the MC-1 and MC-2 test campaigns

No.	t_{in}^{cold} °C	t_{out}^{cold} °C	t_{in}^{hot} °C	t_{out}^{hot} °C	$\dot{Q}$ kW
1	49.7	59.8	59.9	51.5	138.5
2	49.9	60.1	60.2	51.7	139.3
3	49.8	60.0	60.1	51.7	138.8
4	49.9	60.2	60.3	51.8	139.8
5	49.9	60.1	60.2	51.7	139.3
6	49.9	60.1	60.2	51.7	139.2
7	49.9	60.0	60.1	51.6	139.5
8	49.9	60.0	60.2	51.6	139.5
9	50.1	60.3	60.4	51.8	140.2
10	50.1	60.3	60.4	51.8	139.7
11	50.1	60.3	60.4	51.8	140.0
12	50.1	60.2	60.3	51.8	139.8
13	54.2	63.1	63.3	56.4	149.7
14	54.5	63.2	63.4	56.5	150.7
15	54.4	63.1	63.2	56.4	150.4
16	53.8	62.4	62.6	55.7	148.3
17	54.5	63.1	63.2	56.3	150.8
18	54.5	63.0	63.1	56.2	152.3
19	54.6	63.1	63.2	56.3	153.8
20	59.17	70.3	70.88	66.4	174.8
21	59.30	70.3	70.81	66.3	175.4
22	59.62	70.4	70.94	66.3	176.4
23	59.57	70.1	70.59	65.8	176.5
24	58.95	68.2	68.63	63.8	173.9
25	60.20	69.9	70.33	65.1	179.3
26	60.62	69.8	70.17	64.7	181.3
27	60.78	69.7	70.04	64.4	181.7
28	60.93	69.5	69.75	64.0	182.8
29	61.02	69.5	69.69	63.9	183.4

ranged from 59.9 ± 0.2°C to 70.4 ± 0.2°C. The heat transfer rate from the hot water to the refrigerant, causing evaporation and superheating, ranged from 138.5 ± 0.4 kW to 183.4 ± 0.5 kW. The measurement points at the inlet and outlet on the refrigerant side of the generator are shown in the $p - h$ diagram in Fig. 5.20 (top). As shown in the figure, in all cases, the refrigerant at the inlet was in the saturation state, according to the temperature. However, it has to be taken into account that the pressure at the generator inlet was not measured, and the generator outlet pressure was considered constant in this heat exchanger. This is an obvious simplification, and in reality, the pressure at the generator inlet must have been higher, considering pressure drops in this heat exchanger. Moreover, in all cases, the refrigerant reached the saturation parameters inside the heat exchanger. Then, the refrigerant was superheated at the generator outlet for cases no. 1 to no. 12 and no. 20 to no. 29. In cases no. 13 to no. 19, corresponding to the 170 kW measurement series in the MC-1 campaign, vapor superheat at the generator outlet was negligible, reaching 0.3 to 0.7 K.

Fig. 5.20 (bottom) shows the relative error in the estimation of the refrigerant and the hot water outlet temperatures and the estimation error of the heat transfer rate

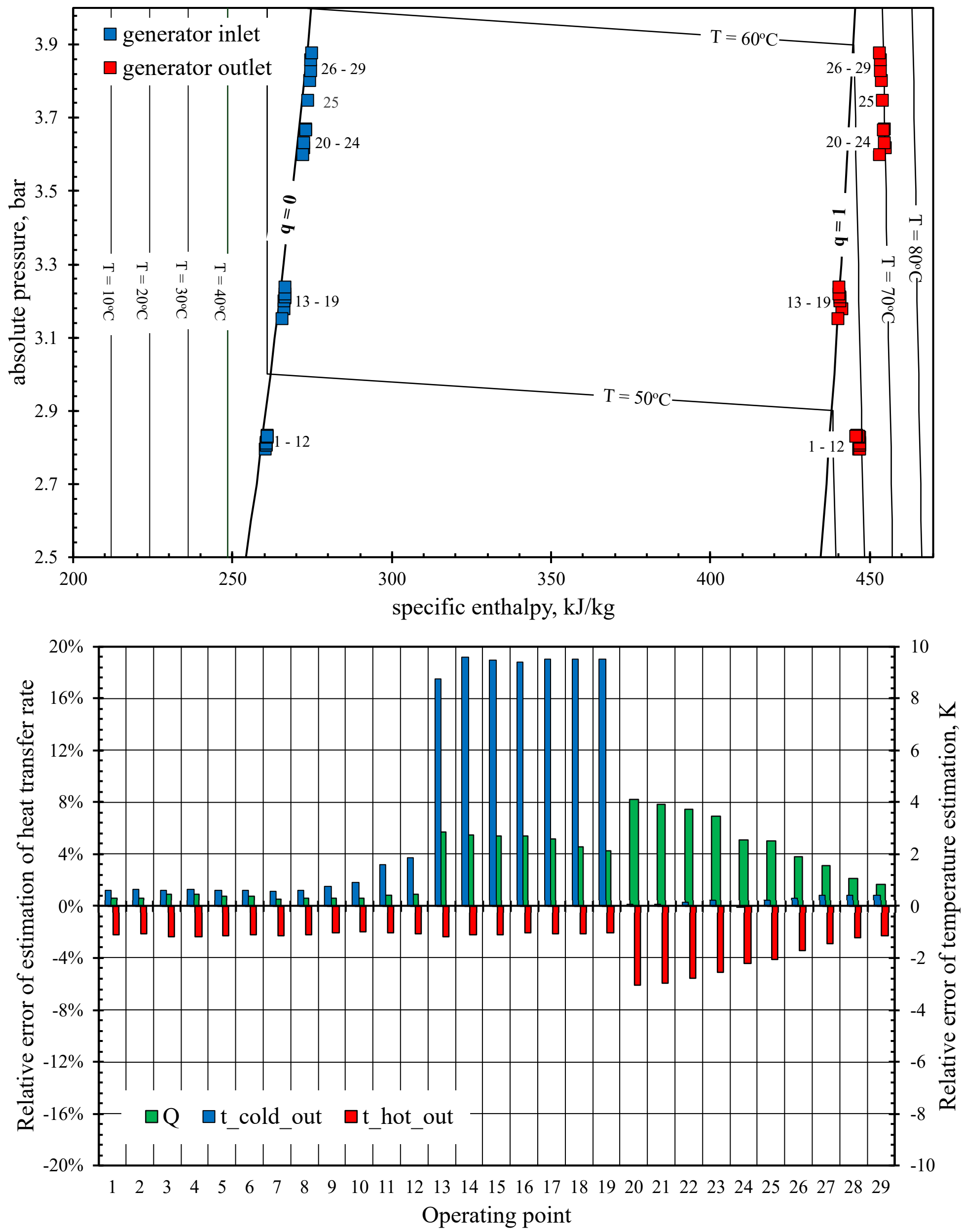

FIGURE 5.20: Generator cold side inlet and outlet parameters from MC-1 and MC-2 presented on $p-h$ diagram (top) and the relative discrepancy in the generator outlet temperatures and heat transfer rate estimation for all operating points (bottom)

transferred in the generator. As can be observed, the LMTD model of the plate heat exchanger very accurately reproduced the hot water outlet temperature of the heat exchanger, which was underestimated relative to experimental measurements by 1 to 3 K for all operating points. On the refrigerant side, for cases no. 1 to no. 12 corresponding to the MC-1 150 kW measurement series, a good representation of the measured values was also achieved with a relative error of up to 1.9 K. Similarly, good accuracy was achieved for points no. 20 to no. 29, corresponding to the 200 kW measurement series from the MC-2 campaign. For these tests, the model predicted vapor superheat corresponding to the superheat achieved during the bench tests. However, for tests no. 13 to no. 19, corresponding to the 170 kW measurement series from the MC-1 campaign, the refrigerant outlet temperature was overestimated by 8.8 to 9.5 K. This was because the model predicted that the exchanged heat transfer rate should be sufficient to achieve a vapor superheat of about 7 K at the generator outlet for all cases in this series. In the performed tests, the superheat was minimal. However, comparing these results with the error in the estimation of the heat transfer rate transferred in the heat exchanger, it can be concluded that a small error in the estimation of the heat transfer rate, at the level of 4% to 6%, caused such a large discrepancy in the outlet temperature here. The heat transfer rate estimation error was similar in other cases, reaching 0% to 8%. However, the results were considered satisfactory.

5.2.3 Validation of the evaporator model

The experimental measurements for the evaporator are detailed in Table 5.6. On the cold side of the heat exchanger, the inlet refrigerant pressure was measured using the pressure transmitter PT-9 and the outlet temperature using the temperature transmitter TT-2, as depicted in the refrigeration system layout in Fig. 3.2. The specific enthalpy at the inlet of the evaporator was assumed to be the same as enthalpy at the outlet of the circulating pump and estimated based on Eq. (4.163) described in Chapter 4.3. The above specific enthalpy is considered input data to the heat exchanger model and is included in Table 5.6. The specific enthalpy at the outlet of the evaporator is estimated based on the measured temperature and the pressure from the evaporator inlet, and the pressure drops in this heat exchanger are impossible to validate. On the hot medium side, the glycol-water solution temperature was recorded at the evaporator inlet and outlet using the temperature sensors TT-gl1 and TT-gl2. The mass flow rate measurements were taken using the FM-ev flow meter on the refrigerant side and the FM-gl meter on the glycol-water side. As seen in the table, all the measurements were performed for high-temperature cooling conditions, corresponding to the glycol-water solution inlet temperature around 19°C and outlet temperature around 16°C. Various cooling capacities from 5.7 ± 0.2 kW to 46.1 ± 0.6 kW were recorded as the result of the critical and sub-critical operation of the refrigeration system, depending on the waste heat parameters and the condensation temperature.

TABLE 5.6: Evaporator experimental data from the MC-1 and MC-2 test campaigns

No.	h_{in}^{cold} kJ/kg	t_{out}^{cold} °C	t_{in}^{hot} °C	t_{out}^{hot} °C	$\dot{Q}$ kW
1	215.7	19.0	19.0	16.7	17.9
2	215.7	18.9	18.9	16.4	18.0
3	215.7	18.4	18.4	16.2	17.2
4	215.7	18.1	18.1	15.8	17.3
5	215.7	18.4	18.4	15.6	15.3
6	215.8	18.8	18.8	15.8	13.0
7	215.8	18.7	18.7	15.7	11.8
8	215.9	18.5	18.5	15.4	10.7
9	216.0	18.7	18.7	15.7	8.8
10	216.0	19.1	19.1	16.0	8.9
11	216.4	17.4	17.4	15.0	5.7
12	216.8	17.5	17.5	15.4	5.7
13	214.7	14.5	14.5	11.9	26.5
14	215.0	19.8	19.8	16.1	26.9
15	215.4	18.8	18.8	15.4	26.4
16	215.3	18.8	18.8	15.4	26.2
17	215.7	19.1	19.1	15.8	25.2
18	216.0	19.5	19.5	16.3	12.8
19	217.1	19.9	19.9	16.3	5.7
20	217.8	19.6	19.6	14.8	45.3
21	217.9	19.6	19.6	14.8	45.5
22	217.9	19.6	19.6	14.8	45.9
23	218.0	19.7	19.7	14.8	46.1
24	218.1	19.5	19.5	14.3	42.8
25	219.1	18.9	18.9	13.6	40.7
26	220.9	18.7	18.7	14.2	32.3
27	222.7	18.4	18.4	14.5	24.0
28	224.5	19.0	19.0	15.5	14.0
29	225.9	20.0	20.0	15.8	6.5

Similarly to the previously validated heat exchanger models in the case of the evaporator, the experimental results from the MC-1 and MC-2 measurement campaigns were used to compare model results with experimental results. The measurement points at the inlet and outlet on the refrigerant side of the evaporator are shown in the $p-h$ diagram in Fig. 5.21 (top). The refrigerant pressure at the inlet of the evaporator was around 0.77 bar(a), corresponding to the refrigerant saturation temperature of 11°C. The specific enthalpy at this operating point ranged from 214.7 ± 0.02 kJ/kg to 225.9 ± 0.02 kJ/kg, giving the points close to the saturation line q = 0 or slightly exceeding it. The refrigerant outlet temperature ranged from 14.5 ± 0.1°C to 20 ± 0.2°C, corresponding to the vapor superheat from 3.5 ± 0.1 K to 9.1 ± 0.1 K.

In Fig. 5.21 (bottom), relative discrepancies of the outlet temperatures and the heat transfer rate estimation for all the operating points are presented. As can be seen, the outlet temperature of the cold side of the heat exchanger, which was the refrigerant in that case, was underestimated for all measured points. The relative error fluctuated between 0 and 1.5 K, which is considered highly accurate. On the hot side of the heat exchanger, an average relative error in the estimation of the outlet temperature of the

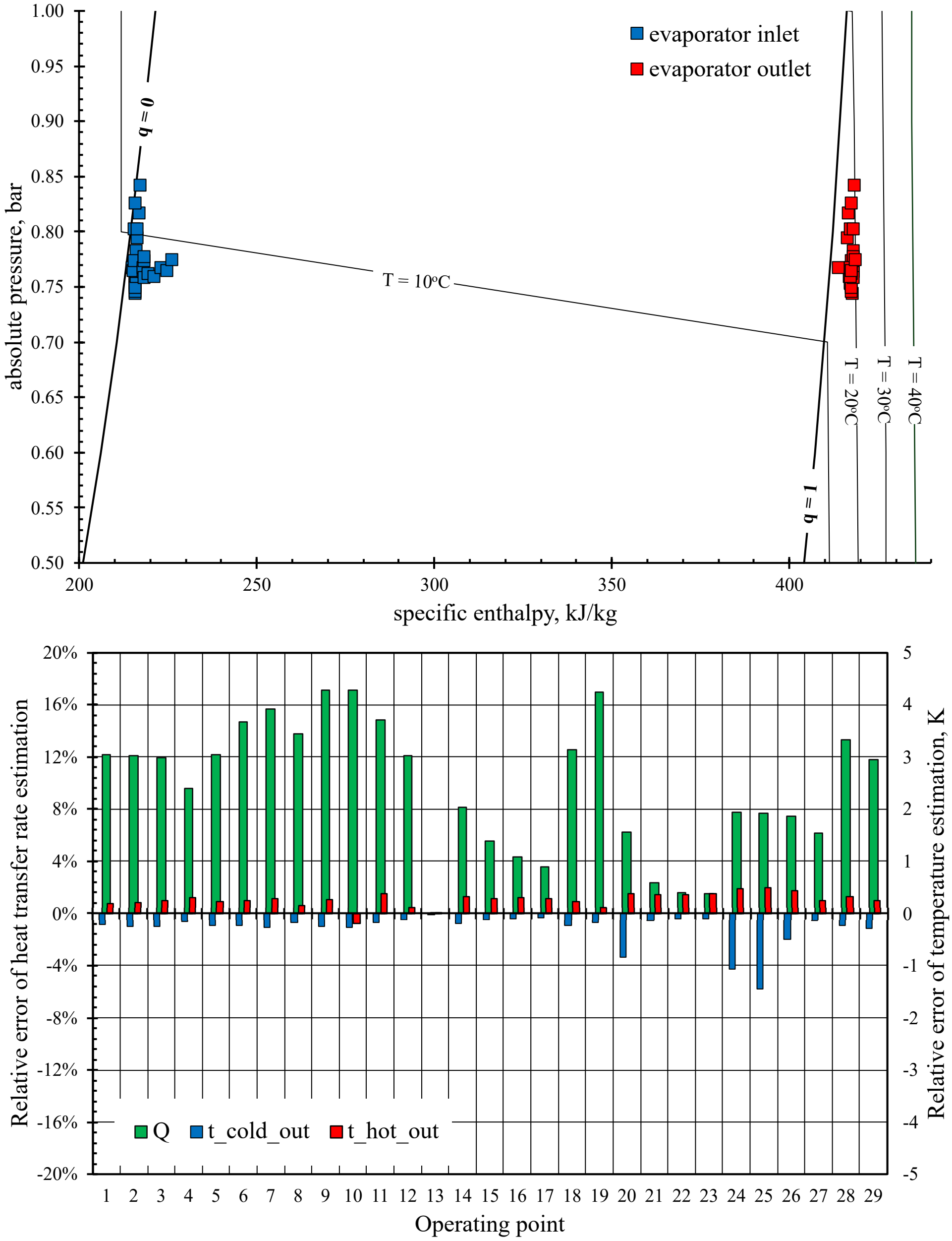

FIGURE 5.21: Evaporator cold side inlet and outlet parameters from MC-1 and MC-2 presented on the $p-h$ diagram (top) and the relative discrepancy in the evaporator outlet temperature and heat transfer rate estimation for all operating points (bottom)

glycol-water solution of 0.3 K was obtained, yielding a maximum error of 0.5 K. The error in estimating the heat transfer rate received from the cooled fluid was a maximum of 17%, but this was recorded for operating points with low cooling capacity, so despite the sizable percentage discrepancy, these results did not differ by more than 2.2 kW in the worst case. For operating points in the critical area, where a constant cooling capacity above 25 kW was recorded, the satisfactory accuracy of the calculation model was obtained, and the relative error did not exceed 9% at these locations. The LMTD model of the evaporator was considered sufficient for system design purposes.

5.2.4 Validation of the condenser model

The condenser model was also compared with the experimental results. The experimental measurements considering the condenser inlet and outlet measuring quantities are presented in Table 5.7. According to Fig. 3.2, the refrigerant temperature and pressure were measured at the inlet and outlet of the hot side of the heat exchanger with the temperature transmitters TT-4 and TT-5 and the pressure transmitters PT-4 and PT-5. The refrigerant mass flow rate was the sum of the values measured by the mass flow meters FM-gen and FM-ev. On the cold side of the heat exchanger, the temperatures at the inlet and outlet of cold water were measured by the temperature transmitters TT-cw1 and TT-cw2. The mass flow rate was measured indirectly by the volume flow meter FM-cw.

As seen in the table, all the inlet temperatures of cold water during test campaigns ranged between 12.3±0.1°C and 15.0±0.1°C. Controlling the cold water flow through the heat exchanger guaranteed the ability to influence the set condensation temperature of the refrigerant and the heat transfer rate transferred to the environment. It also influenced the water temperature at the exchanger outlet, which varied from 17.6±0.1°C to 30.6 ± 0.2°C for the selected measurement series. The heat transfer rate transferred to the environment through the cooling water loop ranged from 157.4 ± 0.8 kW to 241.4 ± 1.2 kW. The inlet temperature of the refrigerant for the tested operating parameters was between 19.7 ± 0.1°C and 31.0 ± 0.2°C, and the outlet temperature was between 13.1 ± 0.1°C and 21.6 ± 0.1°C. Under the given conditions, the refrigeration system was tested over a wide range of saturation temperatures in the condenser, which were between 19.8 ± 0.1°C and 30.9 ± 0.2°C. Due to pressure measurements at the inlet and outlet of the refrigerant, the pressure drop on the hot side of the condenser could be calculated, allowing this parameter to be compared in model calculations. The measured pressure drop ranged from 2.1 ± 0.02 kPa to 11.0 ± 0.03 kPa.

The top of Fig. 5.22 shows the inlet and outlet parameters of the condenser on the refrigerant side. As can be seen, the refrigerant at the condenser inlet was already at the saturation line, which could generate measurement errors. At the condenser outlet, the refrigerant liquid subcooling was achieved for all operating points, ranging from 6.6 ± 0.1 K to 10.5 ± 0.1 K.

TABLE 5.7: Condenser experimental data from the MC-1 and MC-2 test campaigns

No.	t_{in}^{cold} °C	t_{out}^{cold} °C	t_{in}^{hot} °C	t_{out}^{hot} °C	ΔP^{hot} kPa	$\dot{Q}$ kW
1	13.1	17.6	19.7	13.1	2.5	166.5
2	13.1	18.2	19.9	13.2	3.0	167.6
3	13.1	17.6	19.9	13.2	2.1	166.2
4	13.1	18.1	20.0	13.2	2.5	167.5
5	13.1	18.3	20.1	13.2	2.5	164.9
6	13.2	18.7	20.2	13.2	2.7	162.6
7	13.2	19.1	20.4	13.2	3.2	161.8
8	13.2	19.7	20.7	13.3	3.7	160.9
9	13.3	20.3	21.0	13.4	4.5	160.1
10	13.4	20.8	21.4	13.4	5.2	159.8
11	13.4	21.3	21.8	13.7	5.6	157.6
12	13.5	21.7	22.2	14.1	6.0	157.4
13	12.3	17.7	20.9	12.3	2.7	199.1
14	12.5	18.0	21.2	12.6	2.8	201.1
15	12.9	19.3	21.3	12.8	2.5	197.4
16	12.8	18.0	21.5	12.9	3.4	200.1
17	13.1	20.9	22.3	13.1	4.6	199.9
18	13.4	22.4	23.2	13.4	6.4	189.5
19	13.5	23.9	24.4	14.3	7.5	184.1
20	14.8	18.8	22.90	14.9	3.1	236.5
21	14.8	20.2	23.31	14.9	4.1	237.8
22	14.9	21.9	23.98	15.0	6.0	240.3
23	14.9	23.0	24.57	15.0	7.6	241.4
24	14.9	24.1	25.23	15.1	9.3	236.0
25	15.0	25.5	26.44	15.9	10.8	241.0
26	15.0	27.0	27.74	17.4	11.0	234.9
27	15.0	28.3	28.93	19.0	10.8	226.5
28	15.0	29.6	30.11	20.5	10.3	217.2
29	15.0	30.6	31.01	21.6	9.5	209.6

Fig. 5.22 (bottom) shows the relative errors of the computational model estimations of the characteristic quantities, i.e., the outlet temperatures on the hot and cold sides of the heat exchanger, the heat transfer rate returned to the cold water, and the pressure drop on the refrigerant side. The outlet temperature was accurately estimated on the cold water side, reaching a relative error ranging from -0.8 K underestimation to 0.2 overestimation of the measured value. On the refrigerant side, good accuracy was achieved for the on-design operating parameters of the refrigeration system, where the relative error was a maximum of 1.1 K. For the subcritical operating parameters of the prototype, the relative error in estimating the outlet temperature was 2.5 K at most. These inaccuracies resulted directly from the condenser heat transfer rate discrepancy, which ranged from -8.8% to 0%. Underestimation of the heat transfer rate resulted in insufficient liquid subcooling at the condenser outlet, causing the outlet temperature estimate inaccuracy. The underestimation of the heat transfer rate may not necessarily have been due to the inaccuracy of the correlations or the thermodynamic properties but also to the inlet parameters of the refrigerant, which may have already been partially liquefied. The modeled pressure losses in the heat

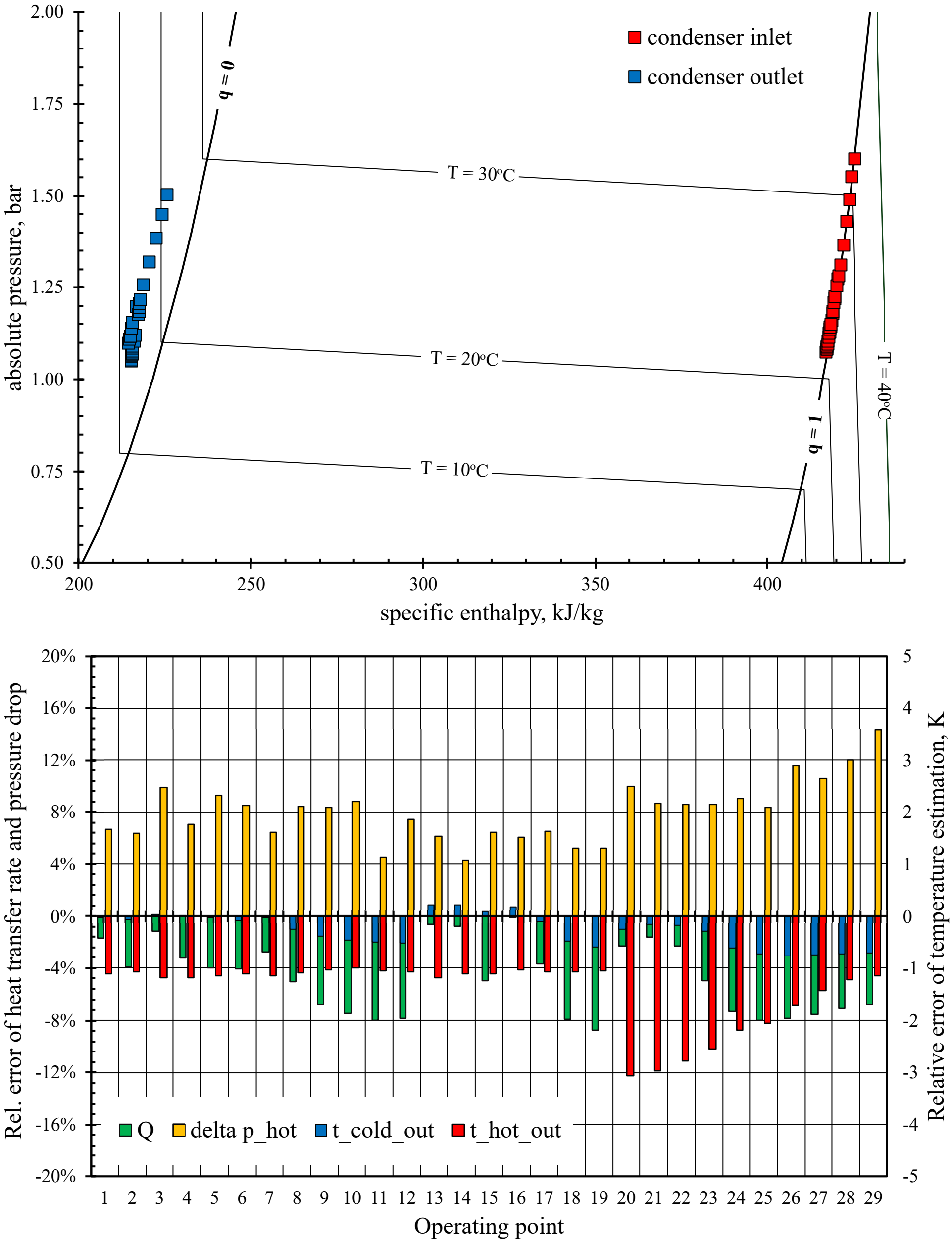

FIGURE 5.22: Condenser cold side inlet and outlet parameters from MC-1 and MC-2 presented on $p-h$ diagram (top) and the relative discrepancy in the condenser outlet temperature, pressure drop at the hot side, and the heat transfer rate estimation for all operating points (bottom)

exchanger were found to be satisfactory. The relative error of estimation of this quantity was 4.3% to 14.3%. The overestimation of this parameter is safe from the perspective of designing a refrigeration system using this calculation model.

5.2.5 Validation of the recuperator model

The last heat exchanger model considered was the recuperator model. Experimental data used for model validation is listed in Table 5.8, where the temperature of the refrigerant at the inlets and outlets of the heat exchanger on both the cold and hot sides, the heat transfer rate transferred in the heat exchanger and the pressure drop on the hot side are presented. According to Fig. 3.2, the refrigerant temperature and pressure were measured at the inlet and outlet of the hot side of the heat exchanger with the temperature transmitters TT-3 and TT-4 and the pressure transmitters PT-3 and PT-4. The refrigerant mass flow rate was the sum of values measured by the mass flow meters FM-gen and FM-ev. On the cold side of the recuperator, the outlet temperature was measured by the temperature transmitter TT-7. However, the outlet pressure was not recorded. Only the pressure measurement PT-6 was placed on the cold side inlet. Hence, the temperature measurement used to validate the recuperator model corresponds to the temperature measured at the condenser outlet by the temperature transmitter TT-5. This may generate additional errors during calculations.

As seen in Table 5.8 on the recuperator cold side, the inlet refrigerant liquid temperature was in the range of 13.1 ± 0.1°C to 21.6 ± 0.1°C. After passing the recuperator and receiving heat from the hot refrigerant vapor, the refrigerant liquid reached 35.2 ± 0.2°C to 51.1 ± 0.2°C at the outlet. On the heat exchanger hot side, the medium vapor temperature at the inlet to the recuperator was 51.3 ± 0.2°C to 62.3 ± 0.2°C. The refrigerant reached saturation parameters at the outlet from the recuperator, which can be observed in the $p-h$ diagram in Fig. 5.23 (top). The heat transferred in the recuperator ranged from 25.0 ± 0.4 kW to 36.5 ± 0.6 kW, which accounted for 15% to 20.5% percent of the waste heat used to drive the refrigeration system on those operating points. This confirmed the validity of using recuperation. The pressure drop measured on the gas side of the recuperator averaged 13.7 kPa, reaching as high as 19.2 ± 0.2 kPa at operating point no. 21.

Fig 5.23 (bottom) shows the relative discrepancies in estimating the outlet temperatures from the recuperator, as well as the heat transfer rate transferred in the heat exchanger and the pressure drop available in the measurements on the hot side of the recuperator. Very high accuracy was achieved in estimating the outlet temperature on the cold side of the medium, where the relative error ranged from -1.8 K to 1.9 K. On the hot side, the inaccuracy of temperature estimation was higher, ranging from 2.2 to 4.2 K. This was due to the underestimation of the heat transfer rate reaching as high as -10.8% and the inaccuracy of correlation for refrigerant vapor flow. Some calculations also gave a sizable overestimation of the heat transfer rate, reaching up to 17.9%. The model may also have generated errors because the operating points were close to the

TABLE 5.8: Recuperator experimental data from the MC-1 and MC-2 test campaigns

No.	t_{in}^{cold} °C	t_{out}^{cold} °C	t_{in}^{hot} °C	t_{out}^{hot} °C	ΔP^{hot} kPa	$\dot{Q}$ kW
1	13.1	42.1	51.4	19.7	11.7	25.0
2	13.2	42.1	51.3	19.9	11.9	25.2
3	13.2	42.1	51.3	19.9	11.5	25.1
4	13.2	42.2	51.3	20.0	11.6	25.3
5	13.2	42.5	51.8	20.1	11.4	25.4
6	13.2	42.8	52.3	20.2	11.2	25.5
7	13.2	42.9	52.5	20.4	10.7	25.5
8	13.3	43.2	52.7	20.7	10.5	25.6
9	13.4	43.5	53.1	21.0	10.2	25.8
10	13.4	43.6	53.2	21.4	10.1	25.8
11	13.7	43.4	53.0	21.8	9.7	25.6
12	14.1	43.5	52.9	22.2	9.6	25.3
13	12.3	39.4	48.5	20.9	15.1	28.8
14	12.6	38.5	47.5	21.2	15.0	28.2
15	12.9	38.8	47.8	21.3	14.8	27.9
16	12.8	38.1	47.1	21.5	14.5	27.1
17	13.1	38.5	47.6	22.3	14.4	27.9
18	13.4	36.6	45.7	23.2	12.7	25.9
19	14.3	35.2	44.3	24.4	11.7	24.2
20	14.9	46.1	56.8	22.9	19.1	37.8
21	14.9	46.1	56.8	23.3	19.2	38.1
22	15.0	46.2	56.8	24.0	19.0	38.5
23	15.0	45.8	56.5	24.6	18.8	38.3
24	15.1	45.7	55.8	25.2	17.7	37.5
25	15.9	46.8	57.1	26.4	17.9	38.9
26	17.4	47.9	58.3	27.7	16.5	38.4
27	19.0	48.6	59.4	28.9	15.2	37.2
28	20.5	50.0	61.0	30.1	13.6	37.0
29	21.6	51.1	62.3	31.0	12.7	36.5

saturation line on the hot side of the heat exchanger. However, a good representation of the pressure drop on the hot side of the refrigerant was achieved, ranging from -2.9% to 6.0%. The recuperator model was found to be functional and sufficient for design calculations.

5.3 Ejector refrigeration system results

The previous subsections discussed the validation results of the mathematical model developed for the refrigeration system components. However, this subsection presents a detailed analysis of the experimental results for the two prototype refrigeration systems, partially described earlier as the results used for the model validation. These experimental results were crucial for validating the model and, most importantly, for implementing the first industrial-scale ejector refrigeration systems and developing the technology. The detailed discussion provides a better understanding of the efficiency and performance of these systems under real operating conditions.

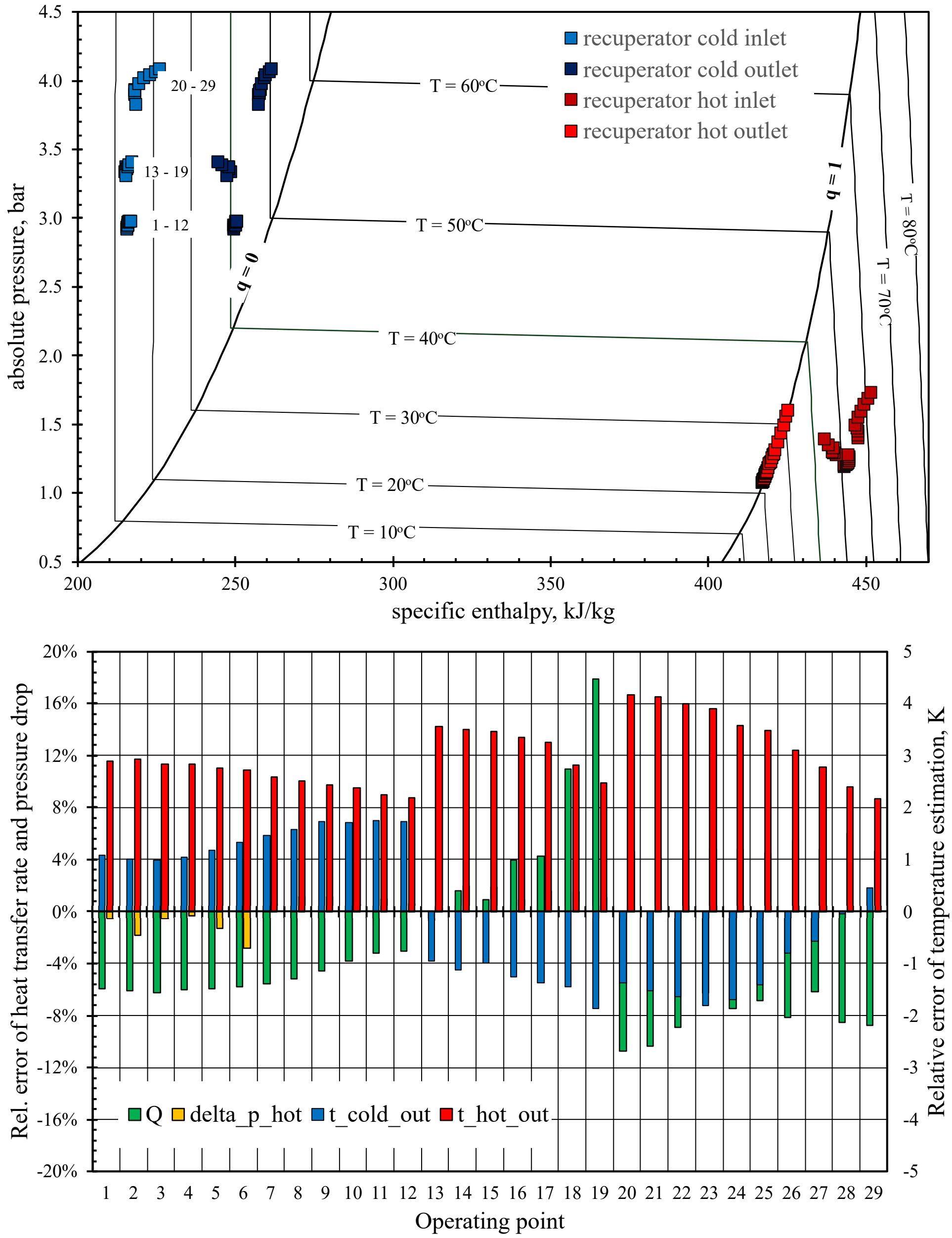

FIGURE 5.23: Recuperator cold side inlet and outlet parameters from MC-1 and MC-2 presented on $p-h$ diagram (top) and the relative discrepancy in the recuperator outlet temperature, pressure drop at the hot side, and heat transfer rate estimation for all operating points (bottom)

5.3.1 The operating conditions of refrigeration systems

To accurately assess the performance parameters of the ejector refrigeration systems, it is essential to gather comprehensive information about several key aspects. This includes the driving waste heat, which powers the system, the characteristics of the cooled medium, and the conditions on the condenser side. Those parameters influence three levels of pressure, which determine the ejector operation and are crucial for evaluating the performance of the refrigeration systems.

Ejector-based refrigeration system driven by 200 kW waste heat

The experimental tests on the prototype refrigeration system called the MARANI CHILLER 200 were carried out for five series of measurements and two variants of ejector geometry, which was described in Chapter 3.2. The real waste heat source, i.e. the oil cooling loop of the air compressors, drove the prototype. The parameters of waste heat are presented in Fig. 5.24. As can be seen in the figure that illustrates the 150 kW series from the MC-1 test campaign, it was possible to obtain very stable conditions for driving the refrigeration system. Waste heat transfer rate ranged from 147.6 ± 0.9 kW to 150.3 ± 0.9 kW was obtained. These conditions deviated significantly from the rated parameters of the refrigeration system designed to be driven with the waste heat capacity of 200 kW. It is worth noting that for the mentioned capacity range, the saturation temperature in the generator reached a value in the range of 48.4 ± 0.1°C to 48.8 ± 0.1°C, which can be considered ultra-low waste heat parameters. For this measurement series, the tests were recorded for so-called high-temperature cooling, for which the refrigerant saturation temperature in the evaporator was maintained at 10.3 ± 0.02°C to 12.7 ± 0.02°C. In the second series of the above measurement campaign, it was possible to obtain higher parameters of waste heat, whose stable transfer rate taken over the preheater and generator ranged from 169.1 ± 1.1 kW to 173.9 ± 1.1 kW. By reducing the pressure loss downstream of the circulating pump, it was possible to increase the saturation temperature in the generator, which for this series of measurements fluctuated between 52.4 ± 0.1°C and 53.3 ± 0.1°C. However, due to the still too-low heat transfer rate, the refrigerant vapor at the generator outlet did not achieve the superheat required by the ejector. The evaporator maintained the parameters for high-temperature cooling, where the saturation temperature was 11.0 ± 0.1°C to 13.4 ± 0.1°C. As in the case of the 150 kW series, it was impossible to conduct tests for standard cooling conditions, which required the operation of the ejector for higher pressure ratios.

After changing the geometry of the ejector justified by the low values of the adopted component efficiencies of the ejector model, which were unexpected at the design stage, as well as modifying the heating system and attaching another compressor to the heat recovery system, the MC-2 measurement campaign was carried out. A heat transfer rate of 185.3 ± 0.6 kW to 194.9 ± 0.5 kW was achieved on the supply and the saturation temperature in the generator settled at 57.0 ± 0.1°C to 59.7 ± 0.1°C. The high-temperature cooling parameters were still maintained in the evaporator, resulting in a saturation temperature in the range of 10.8 ± 0.1°C to 11.4 ± 0.1°C. This series was carried out while keeping the nominal parameters of the refrigeration system.

In the last test campaign, MC-3, two series were recorded after abandoning the recuperator to reduce flow resistance downstream of the ejector. The two series were conducted for two evaporator pressure levels. The first series of the tests were performed for the so-called standard cooling conditions, for which the glycol temperature was maintained at around 12°C at the inlet and 6°C at the outlet of the evaporator. The refrigerant saturation temperature at the evaporator was stable at an average value of 3.0°C. The saturation temperature in the generator during the tests in this series was also stable and averaged 57.7°C. The waste heat transfer rate ranged from 211.9 ± 0.3 kW to 223.9 ± 0.4 kW. The refrigeration system was again tested under high-temperature cooling conditions in the second series of tests. For the first four operating points with the lowest condensation temperature, it was impossible to carry out the tests keeping the glycol temperature within 19°C at the inlet and 16°C at the outlet of the evaporator. That resulted from exceeding the cooling capacity of 50 kW, which was the maximum value in experimental tests due to the power of the electric boiler simulating the artificial load on the evaporator. Therefore, the temperature was maintained at 12°C/9°C for the first three operating points and the fourth at 14°C/11°C. For the last operating points, where the system was already operating in the off-design operational area, it was possible to obtain the required glycol parameters by reaching an average temperature of 18°C at the evaporator inlet and 16°C at the outlet. The saturation temperature in the evaporator was between 10.0 ± 0.1°C and 11.8 ± 0.1°C. During this test series, there were problems with the waste heat supply due to the unstable operation of the air compressors. The heat transfer rate ranged from 176.8 ± 1.1 kW to 204.5 ± 1.1 kW. It should be mentioned that after removing the recuperator from the refrigeration system, the required waste heat transfer rate needed for nominal system operation increased by about 20 kW, which was previously recovered before the condenser. Because of this, the generator achieved a saturation temperature of 51.8°C on average, resulting in the inferior operation of the refrigeration system.

Ejector system driven by 600 kW waste heat

As mentioned in Chapter 3.2, experimental measurements were carried out on a 600 kW test stand with steam as the driving medium. The operating characteristics of the heating system, which was simultaneously responsible for driving the refrigeration system and simulating the evaporator load, affected the unstable operation of the prototype. For an unstable heat source, thirteen operating points were obtained using the R1233zd(E) refrigerant in the MC-4 test campaign. The waste heat parameters and saturation temperatures in the generator, evaporator, and condenser are presented in Fig. 5.25 (top). The waste heat transfer rate transferred to drive the generator ranged from 493.6 ± 2.0 kW for point no. 4 to 642.1 ± 1.3 kW for point no. 9. The generator

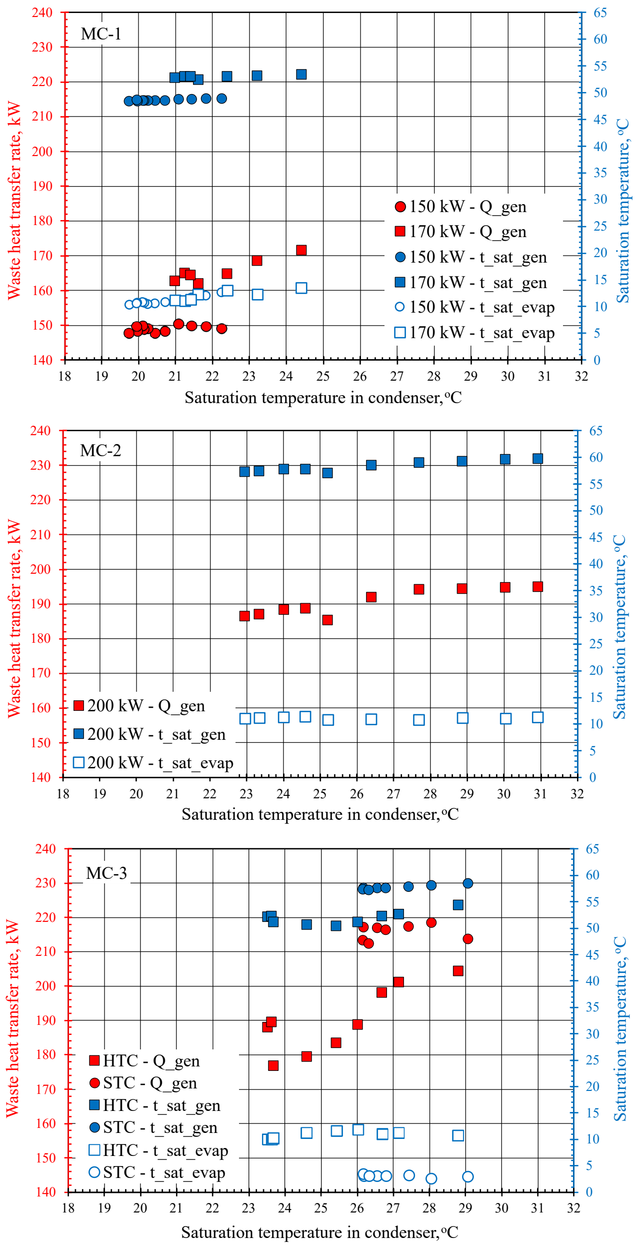

FIGURE 5.24: Operating conditions of the ejector refrigeration system MARANI CHILLER 200, i.e., waste heat transfer rate (Q_{gen}), saturation temperatures in the generator ($t_{sat,gen}$) and the evaporator ($t_{sat,evap}$) in the test campaigns MC-1 to MC-3 in a function of the condensation temperature

maintained the refrigerant saturation temperature of 53.5 ± 0.1°C to 64.7 ± 0.1°C. Due to the system design to receive heat from the hot water, the large surface area of the generators and the preheater prevented the increase in the generator saturation temperature, and any attempt to increase the driving heat resulted in the increased superheating at the generator outlet. This parameter was for all cases above 20 K, reaching as high as 85.3 ± 0.5 K for point no. 13. Standard chilled water parameters were maintained in the evaporator, resulting in saturation temperatures between 0 ± 0.1°C and 6.1 ± 0.1°C. The condensation temperature ranged from 20.2 ± 0.1°C to 27.3 ± 0.1°C.

After modifying the heating system to lower the saturation temperature of the heating steam below atmospheric pressure, reducing the area of the generator, and changing the refrigerant to R1234zd(E), measurements were performed in the MC-5 tests campaign, for which six operating points were obtained. A 1.20 ± 0.02 bar(a) driving steam saturation pressure was obtained for the operating points no. 1 and no. 2 and an average of 0.54 ± 0.02 bar(a) for operating points no. 3 to no. 6. The waste heat transfer rate and generator, evaporator, and condenser saturation temperatures are shown in Fig. 5.25 (bottom). The driving heat transfer rate was around the rated parameters from 570.6 ± 1.9 kW for the operating point no. 3 to 632.0 ± 1.2 kW for the operating point no. 2. The saturation temperature in the generator settled at 52.2°C on average. The superheat of the medium at the generator outlet for the first two points averaged 51.5 K and from 7.2 ± 0.4 K to 15.7 ± 0.2 K for the operapoints no. 3 to no. 6. Standard cooling conditions were maintained in the evaporator by keeping the glycol parameters in the 6°C/12°C regime, resulting in a saturation temperature of 4.2°C on average. The condensation temperature ranged from 22.4 ± 0.1C to 25.5 ± 0.1C.

5.3.2 Influence of the condensation temperature on refrigeration system coefficient of performance

Fig. 5.26 shows the performance characteristics of the ejector refrigeration system in the form of the dependence of the COP and refrigeration capacity $\dot{Q}_0$ as a function of the saturation temperature in the condenser.

For the 150 kW series in the test campaign MC-1, when the refrigeration system operated far from its nominal parameters, COP of 0.12 ± 0.001 was obtained for on-design conditions, which corresponded to the cooling capacity $\dot{Q}_0$ of 17.5 ± 0.03 kW. The ejector system operated at on-design conditions until the condensation temperature reached 20°C. Then, the refrigeration system worked with the decreasing parameters to 23°C of the condensation temperature. For on-design conditions and the increased waste heat parameters, COP of 0.16 ± 0.01 and $\dot{Q}_0$ of 26.5 ± 0.03 kW were achieved in the 170 kW series in MC-1. The on-design operation was obtained until the condensation temperature of 22°C was reached. The ejector work was extinguished for the condensation temperature around 25°C. Finally, after modification of ejector geometry and increasing the waste heat parameters (200 kW series in MC-2), $\dot{Q}_0$ of 46 ± 0.07 kW and COP of 0.24 ± 0.001 were achieved for the on-design operating conditions. The

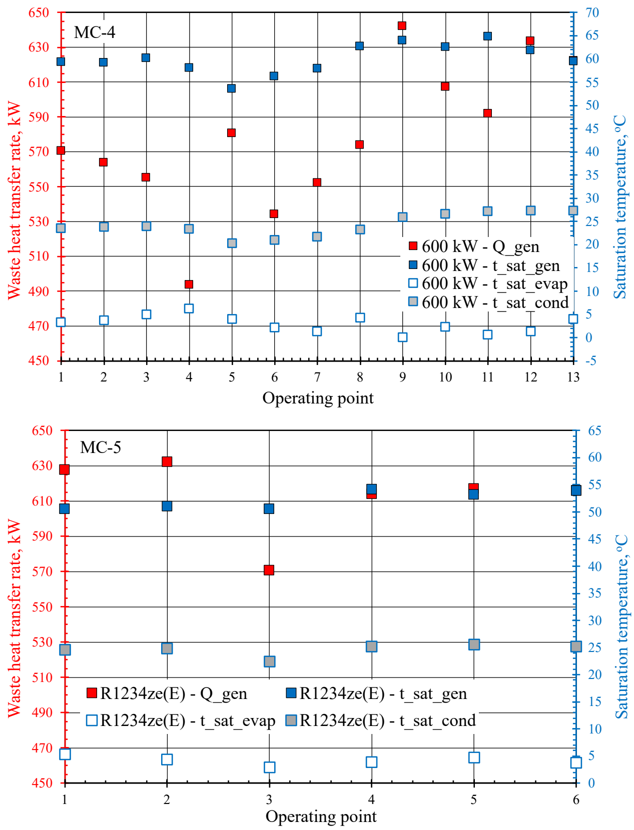

FIGURE 5.25: Operating conditions of the ejector refrigeration system MARANI CHILLER 600, i.e., waste heat transfer rate (Q_{gen}), saturation temperatures in the generator ($t_{sat,gen}$), evaporator ($t_{sat,evap}$) and condenser ($t_{sat,cond}$) in the tests campaigns MC-4 and MC-5 for all operating points

characteristics decreased at a saturation temperature of about 25°C, extinguishing the ejector operation until a level of 32°C. From Fig. 5.26, a simple relationship of increasingly better system performance can be deduced as the waste heat transfer rate increases and approaches the design values. No significant effect of the refrigerant lack of superheating at the ejector motive inlet was noticed for the 170 kW series of MC-2. However, to unequivocally assess this parameter impact on the refrigeration system performance, it would be necessary to carry out a series of measurements under similar waste heat parameters to obtain a range of operating points with variable superheating at the generator outlet. Such tests, however, are challenging to perform on a refrigeration unit driven by waste heat from an industrial process such as air compression, limiting control over its parameters.

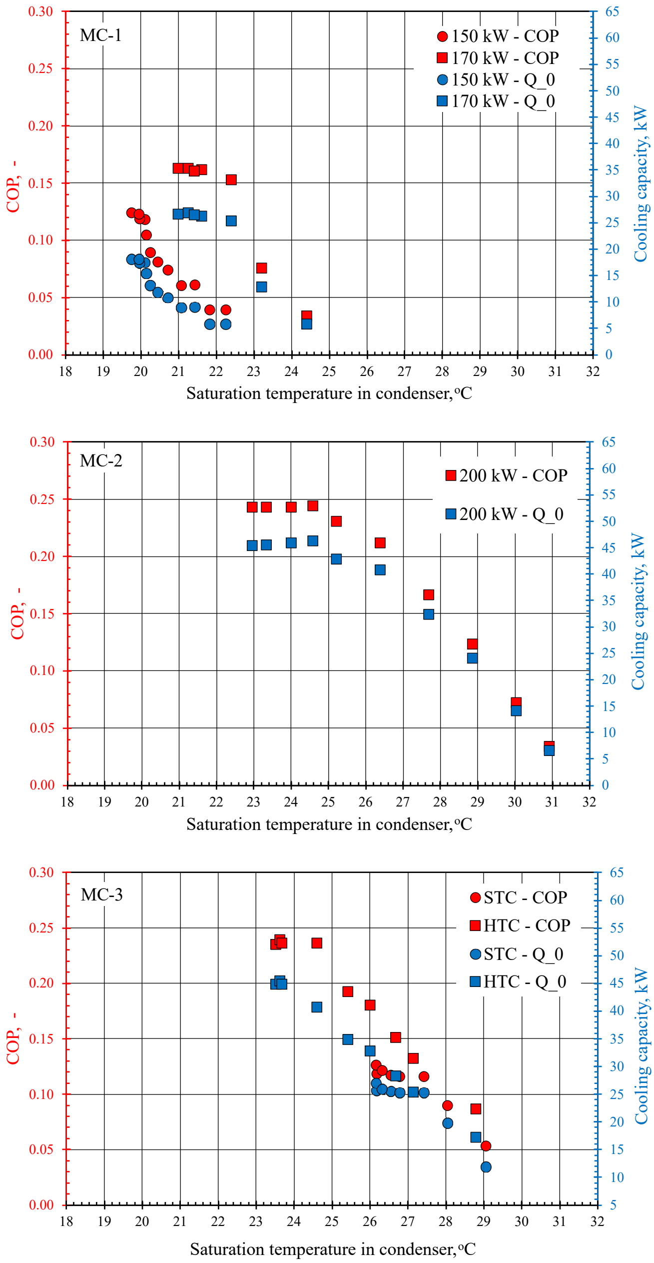

FIGURE 5.26: Performance of the ejector refrigeration system MARANI CHILLER 200, i.e., cooling capacity ($\dot{Q}_0$) and coefficient of performance (COP) in measuring campaigns MC-1 to MC-3 in a function of the condensation temperature

In the MC-3 measurement campaign, after removing the recuperator for high-temperature cooling in the 16°C/19°C series, COP of 0.24 ± 0.001 and a cooling capacity of 45.4 ± 0.07 kW were again obtained in the critical area. The critical point was again at about 25°C of saturation temperature in the condenser. Therefore, it can be concluded that the pressure loss reduction downstream of the ejector did not have the positive effect of shifting the critical point to higher values of saturation pressure in the condenser relative to the 200 kW series from the MC-2 measurement campaign. However, it should be considered, as mentioned above, that for this test series, it was necessary to lower the saturation temperature in the evaporator to adjust the cooling capacity to the available power of the heating boiler, loading the evaporator. With the previous parameters, the cooling capacity exceeded 50 kW, which was unacceptable due to the insufficient artificial heat load on the evaporator. In addition, it should be taken into account that the system was not operating at rated conditions due to the waste heat transfer rate used to drive the ejector to replace the sum of the heat transfer rates previously fed to the generator and recovered in the recuperator. To achieve similar parameters, it would have been necessary to supply the cooling system with the waste heat load of about 220 kW, which was impossible due to the unstable operation of the heat source, i.e., the air compressors in this test series. Therefore, it is more comparable regarding conditions to the 170 kW series in the MC-1 campaign. It can then be concluded that pressure loss reduction downstream of the ejector by removing the recuperator ensured a shift of the critical point by about 3 K on the condensation temperature line due to the required lower pressure ratio of the ejector. The more efficient operation of the cooling system was confirmed by the ability to run a series of measurements at the standard chilled water parameters of 6°C/12°C. The required stable waste heat transfer rate was achieved for this measurement series. As a result, COP of 0.13 ± 0.001 was obtained in the on-design operation area, reaching a maximum cooling capacity of 26.9 ± 0.04 kW. This was a lower performance than expected, but it allowed the utility of the R1233zd(E) refrigerant to be evaluated in two evaporator operating modes. The critical point for the given parameters was at a condensation temperature of about 27.5°C, which was the expected value.

5.3.3 Key results from the ejector refrigeration system MARANI CHILLER 600

In the case of a prototype refrigeration system powered by the 600 kW waste heat, it was not possible to obtain consistent measurement series to determine the performance characteristics of the unit in the case of the MC-4 test campaign. The parameters obtained for single operating points with diversified supply parameters were used to evaluate the system operation. Fig. 5.27 shows the performance of the MARANI CHILLER 600 cooling system for all operating points from the MC-4 test campaign, using R1233zd(E) as the working fluid. The graphs show cooling capacity ($\dot{Q}_0$) and coefficient of performance (COP). As can be seen, driving the cooling system with high-temperature waste heat (of temperature above 140°C) and increasing the saturation temperature in the generator increased the cooling system capacity, compared to tests on the 200 kW system, where saturation temperature of about 60°C was obtained. Moreover, the system was able to operate at standard chilled water parameters. The maximum COP of 0.29 ± 0.001 was obtained for the condensation temperature of 23.4°C ±0.03°C, achieving the cooling capacity of 145.4 ± 0.2 kW. The R1233zd(E) refrigerant was still sensitive to pressure drops downstream the ejector in these parameters, which resulted in the operating points with a maximum COP of 0.12 ± 0.001 and the maximum cooling capacity of 73.6 ± 0.1 kW when the saturation temperature in the condenser exceeded 25°C. It could be concluded that the ejector refrigeration system using low-pressure HFO refrigerant could achieve satisfactory performance, driven by the waste heat of higher parameters.

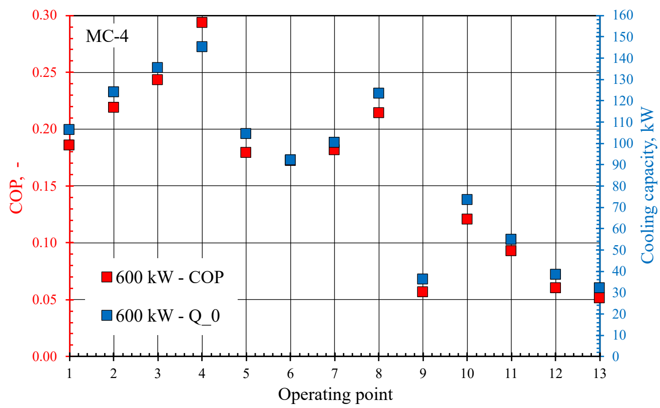

FIGURE 5.27: Performance of the ejector refrigeration system MARANI CHILLER 600, i.e., cooling capacity ($\dot{Q}_0$) and coefficient of performance (COP) in measuring campaign MC-4 for all operating points

For the MC-5 measurement series, due to the stable operating parameters of the heating system and decreasing the driving steam pressure, it was possible to determine the device operating points for supply with low-grade waste heat for points no. 3 to no. 6. For the first two points, the high superheat of the refrigerant vapor was measured at the generator outlet. The key parameters determining the system performance, i.e., cooling capacity $\dot{Q}_0$ and COP, can be seen in Fig. 5.28. For points no. 3 to no. 6, the prototype for standard cooling conditions achieved COP of 0.25 ± 0.001 in the critical operating condition, resulting in a cooling capacity of about 126.1 ± 0.2 kW. In the case of a 200 kW refrigeration system using R1233zd(E) for the STC series in the MC-3 campaign, the achieved cooling capacity for similar operating conditions was half that, and it was possible only after minimizing the pressure losses downstream the ejector. This confirmed that the R1233zd(E) refrigerant can be used for high-temperature cooling, but the high-pressure R1234ze(E) is a more suitable solution at standard parameters. The use of recuperation in refrigeration systems with R1233ze(E) and R1234ze(E) is rational from the thermodynamic point of view as it causes COP increase and reduces the required driving heat transfer rate. Still, in the case of low-pressure R1233ze(E) refrigerant, it has an unfavorable effect on the efficiency of the ejector operation due to the excessive sensitivity of the slight pressure drops.

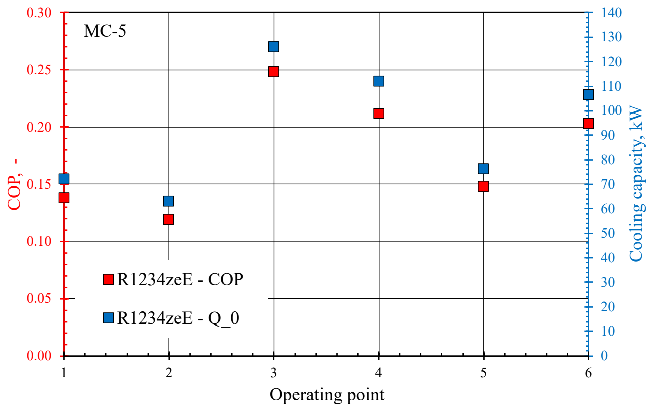

FIGURE 5.28: Performance of the ejector refrigeration system MARANI CHILLER 600, i.e., cooling capacity ($\dot{Q}_0$) and coefficient of performance (COP) in measuring campaign MC-5 for all operating points

Chapter 6

Summary and conclusions

The PhD thesis presents an in-depth study on developing an application to select components for ejector refrigeration systems powered by low-temperature waste heat from industrial processes. The study encompasses creating a mathematical model, testing prototype refrigeration units, and a comparative experimental analysis of different refrigerants.

An ejector refrigeration system model with a single-phase ejector and plate heat exchanger models was developed and validated by experimental measurements from the first industrial-scale prototypes of an ejector refrigeration system driven by low-grade waste heat of 200 kW and 600 kW. The first of these systems was investigated under actual industrial operating conditions while connected to an actual source of waste heat in the form of the oil system of an air compressor unit operating in a production operating regime. The second prototype refrigeration system was tested on a specially adapted test installation fed with waste heat from a steam generator.

The above prototypes utilized a novel, environmentally friendly working fluid from the HFO group, R1233zd(E), known for its low-pressure levels within the tested temperature ranges. The ejector system configuration with the recuperator for partial heat recovery behind the ejector was used. The physical separation of the waste heat recovery exchanger into a preheating section in the preheater and a refrigerant evaporating and superheating section in the generator was an innovative design. Large gas ejector sizes for this type of refrigeration system were employed, and a refrigeration system driven by 600 kW of waste heat used a system of three ejectors operating in parallel and connected using an innovative manifold. This was the first time an ejector cooling system was tested on such a large scale, involving parallel connected plate heat exchangers. The experimental results from these prototypes provided valuable data for validating the mathematical model and demonstrating the practical feasibility of the proposed technology.

Five measurement campaigns were carried out for two prototypes and several system configurations. In the case of the ejector refrigeration system driven by the waste heat of 200 kW, three measurement campaigns were carried out for the high-temperature cooling variant, i.e., for glycol parameters (16°C/19°C). In the last test campaign also, the standard cooling variant, i.e., for glycol parameters 6°C/12°C was possible to examine. Two ejector geometry variants and two refrigeration system configurations (with and without recuperator) were tested. The prototype was measured for several variants of waste heat, considering ultra-low and low-grade parameters under nominal and operating conditions lower than nominal. In the case of a refrigeration system nominally driven by 600 kW waste heat, two measurement campaigns were performed testing the refrigeration system for two refrigerants, R1233zd(E) and R1234ze(E).

A comprehensive mathematical model was developed to rapidly select components for ejector refrigeration systems. An algorithm consists of models of individual components. The results of the model of the most essential device of the refrigeration system, i.e., the supersonic ejector, were preliminarily verified based on available in the literature experimental results for phased-out refrigerants, achieving high accuracy of estimation of the MER in the critical and sub-critical region of operation. A relative error of less than 10% for calibrated component efficiencies of the ejector model was obtained. The high sensitivity of the ejector model was observed for the proper assumption of the mixing chamber efficiency.

The model was extensively validated against experimental data from the prototype systems. The validation process involved comparing model predictions with measured values of crucial parameters, such as MER, pressure ratio, and efficiency, under various operating conditions. The ejector component efficiencies used in the ejector model calculations were optimized to ensure the maximum accuracy of MER estimation for each measurement series. A satisfactory accuracy of estimation was obtained for crucial parameters of the ejector operation (i.e., the mass entrainment ratio, the pressure ratio, and the ejector efficiency). For the ejector component efficiencies dedicated separately for each series of measurements performed using the MARANI CHILLER 200 prototype, the average relative discrepancies of mass entrainment ratio, the pressure ratio, and the ejector efficiencies estimation of 5.0%, 5.6%, and 15.3%, respectively. However, the model is sensitive to a change in the adopted component efficiencies, especially in the case of the R1233zd(E) refrigerant, and requires their calibration when a significant change is made in the operating parameters of the ejector. This was confirmed by attempting to calibrate the model for all operating points recorded in the three measurement series comprising measurement campaigns MC-1 and MC-2 in the case of the MARANI CHILLER 200 and calibrating the model for all operating points recorded for the MARANI CHILLER 600 system in measurement campaign MC-4, which differed significantly in the boundary conditions, occurred at the ejectors motive nozzle inlets.

To design an ejector for the given operating conditions, experimental results with a similar superheat at the inlets of the ejector should be used to estimate the fixed ejector component efficiencies. When the novel refrigerant R1233zd(E) was used as the working fluid, a surprisingly low value was obtained for the isentropic expansion efficiency in the ejector suction nozzle compared to refrigerants previously described in the literature. However, optimizing ejector component efficiencies for high accuracy in the MER estimation may result in reduced accuracy in the ejector efficiency estimation. Therefore, to select appropriate values for the ejector component efficiencies, it is necessary to classify these parameters according to their relevance or to balance the model accuracy between the mentioned performance parameters.

In the case of the R1234ze(E) working fluid used in the last measurement campaign, the ejector model provided broader applicability regardless of the device boundary parameters, achieving average errors in the mass entrainment ratio, the pressure ratio, and the ejector efficiency estimation of 4.4%, 0% and 3.97%, respectively. This conclusion, however, would need to be confirmed by performing more numerous measurement series. This can also be associated with higher operating pressures of the device, which also varies the impact of the minimum measurement errors of the pressure transducers used.

The models of plate heat exchangers, i.e., preheater, generator, condenser, evaporator, and recuperator, were also validated. For this purpose, measurements taken in the first two measurement campaigns were used due to the stable operating conditions and the single occurrence of all the mentioned heat exchangers in the system. High accuracy was obtained in estimating the heat exchanger outlet temperatures and heat transfer rates. For the recuperator and evaporator, it was possible to compare pressure drops on the hot side of the heat exchanger, which also gave satisfactory results. The estimation errors of the above parameters were generally below 10%. For some operating points, estimation errors were within 20%. As a rule, these were operating points close to the saturation line, which generated errors due to the impossibility of accurately comparing the mentioned heat transfer rates.

As a result of experimental tests, a COP of 0.25 for the ejector cooling system MARANI CHILLER 200 was achieved for high-temperature cooling conditions after applying modifications to the ejector geometry, a promising result in the face of ultra-low-temperature waste heat. The use of R1233zd(E) refrigerant offers many advantages in terms of low GWP and non-flammability, non-toxicity, and low operating pressure, avoiding limits and additional investment costs. The above-mentioned parameters and performance make this refrigerant promising, especially in real industrial applications. However, using the low-pressure refrigerant R1233zd(E) posed significant challenges. The most notable challenge was ensuring the system efficient operation due to the sensitive influence of the pressure drops on the ejector performance.

This conclusion was confirmed primarily in the MC-3 measurement campaign, which was performed for a cooling system driven by the 200 kW waste heat after eliminating the recuperator. It had a very significant effect on improving the energy efficiency of the refrigeration system. Still, the slight pressure losses it generated, on the order of 0.2 to 0.3 bar(a), caused a significant drop in the saturation temperature in the condenser. This resulted in the need to operate the ejector for higher pressure ratios, which reduced its efficiency and caused the unit to go into subcritical mode too quickly. After eliminating the pressure losses, the system operated much more efficiently for similar operating parameters, achieving a COP of 0.25 for waste heat supply lower than nominal and high-temperature cooling. Before eliminating pressure losses under similar operating conditions, the system operated with a COP of 0.16. The elimination of the recuperator also made it possible to perform a series of measurements for standard cooling. However, the results obtained were not considered satisfactory. For such operating conditions, a much more efficient refrigerant is high-pressure R1234ze(E), which achieved a COP of 0.25 under similar operating conditions for the MARANI CHILLER 600 refrigeration system.

Future research will focus on further optimizing the mathematical model to enhance its accuracy and efficiency. This includes refining the model parameters and improving the computational algorithms to reduce processing time. Additionally, the model will be expanded to include a wider range of operating conditions and system configurations, making it more versatile and applicable to different industrial scenarios. Furthermore, the implementation, development, and testing of the prototypes are planned to explore the performance of the ejector refrigeration systems under various industrial conditions to check the efficiency and operation flexibility under continuous operation. This will involve scaling up the prototypes, testing them in real-world industrial conditions, and evaluating their long-term reliability and maintenance requirements.

Bibliography

[1] J. Gagan, K. Śmierciew, M. Łukaszuk, D. Butrymowicz, A. Pawluczuk, M. Mastrowski, M. Bergander, and A. Cebula, "Experimental assessment of the first industrial implementation of ejector refrigeration system operating with R1233zd(e) driven by ultra-low temperature heat source," *International Journal of Refrigeration*, vol. 154, pp. 138–150, 2023, ISSN: 0140-7007. DOI: `https://doi.org/10.1016/j.ijrefrig.2023.07.003`. [Online]. Available: `https://www.sciencedirect.com/science/article/pii/S0140700723001974`.

[2] M. Mastrowski, J. Smolka, D. Butrymowicz, L. Antczak, J. Gagan, and K. Śmierciew, "Experimental validation of the theoretical ejector model in a low-grade waste heat refrigeration system using R1233zdE as a working fluid," *Applied Thermal Engineering*, vol. 236, p. 121 716, 2024, ISSN: 1359-4311. DOI: `https://doi.org/10.1016/j.applthermaleng.2023.121716`. [Online]. Available: `https://www.sciencedirect.com/science/article/pii/S1359431123017453`.

[3] G. Kosmadakis, "Industrial waste heat potential and heat exploitation solutions," *Applied Thermal Engineering*, vol. 246, p. 122 957, 2024, ISSN: 1359-4311. DOI: `https://doi.org/10.1016/j.applthermaleng.2024.122957`. [Online]. Available: `https://www.sciencedirect.com/science/article/pii/S1359431124006252`.

[4] M. Hajlasz, S. Helmcke, F. Liebach, T. Schleyer, and K. Somers, *Waste not: Unlocking the potential of waste heat recovery*, 2023. [Online]. Available: `https://www.mckinsey.com/capabilities/sustainability/our-insights/waste-not-unlocking-the-potential-of-waste-heat-recovery#/`.

[5] C. Forman, I. K. Muritala, R. Pardemann, and B. Meyer, "Estimating the global waste heat potential," *Renewable and Sustainable Energy Reviews*, vol. 57, pp. 1568–1579, 2016, ISSN: 1364-0321. DOI: `https://doi.org/10.1016/j.rser.2015.12.192`. [Online]. Available: `https://www.sciencedirect.com/science/article/pii/S1364032115015750`.

[6] K. Semkov, E. Mooney, M. Connolly, and C. Adley, "Efficiency improvement through waste heat reduction," *Applied Thermal Engineering*, vol. 70, no. 1, pp. 716–722, 2014, ISSN: 1359-4311. DOI: `https://doi.org/10.1016/j.applthermaleng.2014.05.030`. [Online]. Available: `https://www.sciencedirect.com/science/article/pii/S1359431114003913`.

[7] M. Soda and A. Beyene, "Multiphase ultra-low grade thermal energy storage for organic rankine cycle," *International Journal of Energy Research*, vol. 40, no. 1, pp. 51–60, 2016. DOI: https://doi.org/10.1002/er.3300. eprint: https://onlinelibrary.wiley.com/doi/pdf/10.1002/er.3300. [Online]. Available: https://onlinelibrary.wiley.com/doi/abs/10.1002/er.3300.

[8] T. Hung, T. Shai, and S. Wang, "A review of organic rankine cycles (orcs) for the recovery of low-grade waste heat," *Energy*, vol. 22, no. 7, pp. 661–667, 1997, ISSN: 0360-5442. DOI: https://doi.org/10.1016/S0360-5442(96)00165-X. [Online]. Available: https://www.sciencedirect.com/science/article/pii/S036054429600165X.

[9] M. Papapetrou, G. Kosmadakis, A. Cipollina, U. La Commare, and G. Micale, "Industrial waste heat: Estimation of the technically available resource in the eu per industrial sector, temperature level and country," *Applied Thermal Engineering*, vol. 138, pp. 207–216, 2018, ISSN: 1359-4311. DOI: https://doi.org/10.1016/j.applthermaleng.2018.04.043. [Online]. Available: https://www.sciencedirect.com/science/article/pii/S1359431117347919.

[10] M. Luberti, R. Gowans, P. Finn, and G. Santori, "An estimate of the ultralow waste heat available in the european union," *Energy*, vol. 238, p. 121 967, 2022, ISSN: 0360-5442. DOI: https://doi.org/10.1016/j.energy.2021.121967. [Online]. Available: https://www.sciencedirect.com/science/article/pii/S0360544221022155.

[11] J. Ling-Chin, H. Bao, Z. Ma, W. Taylor, and A. P. Roskilly, "State-of-the-art technologies on low-grade heat recovery and utilization in industry," in *Energy Conversion*, I. H. Al-Bahadly, Ed., Rijeka: IntechOpen, 2018, ch. 4. DOI: 10.5772/intechopen.78701. [Online]. Available: https://doi.org/10.5772/intechopen.78701.

[12] K. Ebrahimi, G. F. Jones, and A. S. Fleischer, "A review of data center cooling technology, operating conditions and the corresponding low-grade waste heat recovery opportunities," *Renewable and Sustainable Energy Reviews*, vol. 31, pp. 622–638, 2014, ISSN: 1364-0321. DOI: https://doi.org/10.1016/j.rser.2013.12.007. [Online]. Available: https://www.sciencedirect.com/science/article/pii/S1364032113008216.

[13] AtlasCopco, *An introduction to air compressor heat recovery*. [Online]. Available: https://www.atlascopco.com/en-us/compressors/greenproduction/energy-recovery-systems.

[14] Kaeser, *Heat recovery*. [Online]. Available: https://www.kaeser.com/ie-en/products/rotary-screw-compressors/heat-recovery.

[15] M. Broniszewski and S. Werle, "The study on the heat recovery from air compressors," *E3S Web Conf.*, vol. 70, p. 03 001, 2018. DOI: 10.1051/e3sconf/20187003001. [Online]. Available: https://doi.org/10.1051/e3sconf/20187003001.

[16] D. Vittorini and R. Cipollone, "Energy saving potential in existing industrial compressors," *Energy*, vol. 102, pp. 502–515, 2016, ISSN: 0360-5442. DOI: https://doi.org/10.1016/j.energy.2016.02.115. [Online]. Available: https://www.sciencedirect.com/science/article/pii/S0360544216301773.

[17] S. Brückner, S. Liu, L. Miró, M. Radspieler, L. F. Cabeza, and E. Lävemann, "Industrial waste heat recovery technologies: An economic analysis of heat transformation technologies," *Applied Energy*, vol. 151, pp. 157–167, 2015, ISSN: 0306-2619. DOI: https://doi.org/10.1016/j.apenergy.2015.01.147. [Online]. Available: https://www.sciencedirect.com/science/article/pii/S0306261915004584.

[18] J.-N. Gerdes, M. Munder, and A. Sauer, "Evaluation of technical and economic potential of waste heat distribution networks in industrial sites," *Energy Reports*, vol. 9, pp. 219–226, 2023, 2022 The 3rd International Conference on Power, Energy and Electrical Engineering, ISSN: 2352-4847. DOI: https://doi.org/10.1016/j.egyr.2022.12.112. [Online]. Available: https://www.sciencedirect.com/science/article/pii/S2352484722027135.

[19] B. Liu, M. Jia, and Y. Liu, "Estimation of industrial waste heat recovery potential in China: Based on energy consumption," *Applied Thermal Engineering*, vol. 236, p. 121 513, 2024, ISSN: 1359-4311. DOI: https://doi.org/10.1016/j.applthermaleng.2023.121513. [Online]. Available: https://www.sciencedirect.com/science/article/pii/S1359431123015429.

[20] R. Singh, S. Dogra, S. Dixit, N. I. Vatin, R. Bhardwaj, A. K. Sundramoorthy, H. Perera, S. P. Patole, R. K. Mishra, and S. Arya, "Advancements in thermoelectric materials for efficient waste heat recovery and renewable energy generation," *Hybrid Advances*, vol. 5, p. 100 176, 2024, ISSN: 2773-207X. DOI: https://doi.org/10.1016/j.hybadv.2024.100176. [Online]. Available: https://www.sciencedirect.com/science/article/pii/S2773207X2400037X.

[21] X. Feng, F. Shi, G. Qiao, Y. Li, and C. Liu, "Integrating organic rankine cycle with thermoelectric generator in various applications utilizing low-grade energy: A review," *Sustainable Energy Technologies and Assessments*, vol. 68, p. 103 882, 2024, ISSN: 2213-1388. DOI: https://doi.org/10.1016/j.seta.2024.103882. [Online]. Available: https://www.sciencedirect.com/science/article/pii/S2213138824002789.

[22] S. Hur, S. Kim, H.-S. Kim, A. Kumar, C. Kwon, J. Shin, H. Kang, T. H. Sung, J. Ryu, J. M. Baik, and H.-C. Song, "Low-grade waste heat recovery scenarios: Pyroelectric, thermomagnetic, and thermogalvanic thermal energy harvesting,"

Nano Energy, vol. 114, p. 108 596, 2023, ISSN: 2211-2855. DOI: https://doi.org/10.1016/j.nanoen.2023.108596. [Online]. Available: https://www.sciencedirect.com/science/article/pii/S2211285523004330.

[23] Z. Shengjun, W. Huaixin, and G. Tao, "Performance comparison and parametric optimization of subcritical organic rankine cycle (orc) and transcritical power cycle system for low-temperature geothermal power generation," *Applied Energy*, vol. 88, no. 8, pp. 2740–2754, 2011, ISSN: 0306-2619. DOI: https://doi.org/10.1016/j.apenergy.2011.02.034. [Online]. Available: https://www.sciencedirect.com/science/article/pii/S0306261911001334.

[24] D. K. Kim, J. S. Lee, J. Kim, M. S. Kim, and M. S. Kim, "Parametric study and performance evaluation of an organic rankine cycle (orc) system using low-grade heat at temperatures below 80°c," *Applied Energy*, vol. 189, pp. 55–65, 2017, ISSN: 0306-2619. DOI: https://doi.org/10.1016/j.apenergy.2016.12.026. [Online]. Available: https://www.sciencedirect.com/science/article/pii/S0306261916317779.

[25] K.-M. Adamson, T. G. Walmsley, J. K. Carson, Q. Chen, F. Schlosser, L. Kong, and D. J. Cleland, "High-temperature and transcritical heat pump cycles and advancements: A review," *Renewable and Sustainable Energy Reviews*, vol. 167, p. 112 798, 2022, ISSN: 1364-0321. DOI: https://doi.org/10.1016/j.rser.2022.112798. [Online]. Available: https://www.sciencedirect.com/science/article/pii/S1364032122006827.

[26] C. Arpagaus, F. Bless, M. Uhlmann, J. Schiffmann, and S. S. Bertsch, "High temperature heat pumps: Market overview, state of the art, research status, refrigerants, and application potentials," *Energy*, vol. 152, pp. 985–1010, 2018, ISSN: 0360-5442. DOI: https://doi.org/10.1016/j.energy.2018.03.166. [Online]. Available: https://www.sciencedirect.com/science/article/pii/S0360544218305759.

[27] M. Rehfeldt, T. Fleiter, and F. Toro, "A bottom-up estimation of the heating and cooling demand in european industry," *Energy Efficiency*, vol. 11, pp. 1057–1082, 2018, ISSN: 1570-6478. DOI: https://doi.org/10.1007/s12053-017-9571-y. [Online]. Available: https://link.springer.com/article/10.1007/s12053-017-9571-y.

[28] X. Zhai and R. Wang, "A review for absorbtion and adsorbtion solar cooling systems in china," *Renewable and Sustainable Energy Reviews*, vol. 13, no. 6, pp. 1523–1531, 2009, ISSN: 1364-0321. DOI: https://doi.org/10.1016/j.rser.2008.09.022. [Online]. Available: https://www.sciencedirect.com/science/article/pii/S1364032108001652.

[29] X. Wu, S. Xu, and M. Jiang, "Development of bubble absorption refrigeration technology: A review," *Renewable and Sustainable Energy Reviews*, vol. 82, pp. 3468–3482, 2018, ISSN: 1364-0321. DOI: https://doi.org/10.1016/

j.rser.2017.10.109. [Online]. Available: https://www.sciencedirect.com/science/article/pii/S1364032117314806.

[30] A. I. Papadopoulos, A.-S. Kyriakides, P. Seferlis, and I. Hassan, "Absorption refrigeration processes with organic working fluid mixtures- a review," *Renewable and Sustainable Energy Reviews*, vol. 109, pp. 239–270, 2019, ISSN: 1364-0321. DOI: https://doi.org/10.1016/j.rser.2019.04.016. [Online]. Available: https://www.sciencedirect.com/science/article/pii/S136403211930228X.

[31] J. Rodríguez-Muñoz and J. Belman-Flores, "Review of diffusion–absorption refrigeration technologies," *Renewable and Sustainable Energy Reviews*, vol. 30, pp. 145–153, 2014, ISSN: 1364-0321. DOI: https://doi.org/10.1016/j.rser.2013.09.019. [Online]. Available: https://www.sciencedirect.com/science/article/pii/S1364032113006783.

[32] I. Dincer and T. A. H. Ratlamwala, "Fundamentals of absorption refrigeration systems," in *Integrated Absorption Refrigeration Systems: Comparative Energy and Exergy Analyses*. Cham: Springer International Publishing, 2016, pp. 1–25, ISBN: 978-3-319-33658-9. DOI: 10.1007/978-3-319-33658-9_1. [Online]. Available: https://doi.org/10.1007/978-3-319-33658-9_1.

[33] J. Chen, S. Jarall, H. Havtun, and B. Palm, "A review on versatile ejector applications in refrigeration systems," *Renewable and Sustainable Energy Reviews*, vol. 49, pp. 67–90, 2015, ISSN: 1364-0321. DOI: https://doi.org/10.1016/j.rser.2015.04.073. [Online]. Available: https://www.sciencedirect.com/science/article/pii/S1364032115003433.

[34] G. Besagni, R. Mereu, and F. Inzoli, "Ejector refrigeration: A comprehensive review," *Renewable and Sustainable Energy Reviews*, vol. 53, pp. 373–407, 2016, ISSN: 1364-0321. DOI: https://doi.org/10.1016/j.rser.2015.08.059. [Online]. Available: https://www.sciencedirect.com/science/article/pii/S1364032115009223.

[35] A. Paliwoda, *Ejector-based refrigeration systems (in Polish: Urządzenia chłodnicze strumienicowe)*. Wydawnictwo Naukowo-Techniczne, 1971.

[36] D. Butrymowicz, P. Baj, K. Śmierciew, and J. Gagan, *Refrigeration technology (in Polish: Technika chłodnicza)*. PWN, 2021.

[37] J. Sarkar, "Ejector enhanced vapor compression refrigeration and heat pump systems—a review," *Renewable and Sustainable Energy Reviews*, vol. 16, no. 9, pp. 6647–6659, 2012, ISSN: 1364-0321. DOI: https://doi.org/10.1016/j.rser.2012.08.007. [Online]. Available: https://www.sciencedirect.com/science/article/pii/S1364032112004765.

[38] B. Huang and J. Chang, "Empirical correlation for ejector design," *International Journal of Refrigeration*, vol. 22, no. 5, pp. 379–388, 1999, ISSN: 0140-7007. DOI: https://doi.org/10.1016/S0140-7007(99)00002-X. [Online]. Available: https://www.sciencedirect.com/science/article/pii/S014070079900002X.

[39] I. W. Eames, S. W. Worall, and S. Aphornratana, "An experimental investigation of steam ejectors for applications in jet-pump refrigerators powered by low-grade heat," *Proceedings of the Institution of Mechanical Engineers*, vol. 213, no. 5, pp. 351–361, 1999. DOI: 10.1243/0957650991537734. [Online]. Available: https://doi.org/10.1243/0957650991537734.

[40] B. J. Huang, C. B. Jiang, and F. L. Hu, "Ejector Performance Characteristics and Design Analysis of Jet Refrigeration System," *Journal of Engineering for Gas Turbines and Power*, vol. 107, no. 3, pp. 792–802, Jul. 1985, ISSN: 0742-4795. DOI: 10.1115/1.3239802. [Online]. Available: https://doi.org/10.1115/1.3239802.

[41] K. Śmierciew, J. Gagan, D. Butrymowicz, and J. Karwacki, "Experimental investigations of solar driven ejector air-conditioning system," *Energy and Buildings*, vol. 80, pp. 260–267, 2014, ISSN: 0378-7788. DOI: https://doi.org/10.1016/j.enbuild.2014.05.033. [Online]. Available: https://www.sciencedirect.com/science/article/pii/S037877881400437X.

[42] X. Ma, W. Zhang, S. Omer, and S. Riffat, "Experimental investigation of a novel steam ejector refrigerator suitable for solar energy applications," *Applied Thermal Engineering*, vol. 30, no. 11, pp. 1320–1325, 2010, ISSN: 1359-4311. DOI: https://doi.org/10.1016/j.applthermaleng.2010.02.011. [Online]. Available: https://www.sciencedirect.com/science/article/pii/S1359431110000700.

[43] Z. Chen, H. Zhao, F. Kong, G. Liu, L. Wang, and Y. Lai, "Synergistic effect of adjustable ejector structure and operating parameters in solar-driven ejector refrigeration system," *Solar Energy*, vol. 250, pp. 295–311, 2023, ISSN: 0038-092X. DOI: https://doi.org/10.1016/j.solener.2023.01.001. [Online]. Available: https://www.sciencedirect.com/science/article/pii/S0038092X23000014.

[44] J. Beyrami and A. Hakkaki-Fard, "Performance evaluation of the solar-driven multi-ejector refrigeration cycle without an auxiliary heat source," *Applied Thermal Engineering*, vol. 217, p. 119 214, 2022, ISSN: 1359-4311. DOI: https://doi.org/10.1016/j.applthermaleng.2022.119214. [Online]. Available: https://www.sciencedirect.com/science/article/pii/S1359431122011450.

[45] S. Shen, X. Qu, B. Zhang, S. Riffat, and M. Gillott, "Study of a gas–liquid ejector and its application to a solar-powered bi-ejector refrigeration system," *Applied Thermal Engineering*, vol. 25, no. 17, pp. 2891–2902, 2005, ISSN: 1359-4311. DOI:

https://doi.org/10.1016/j.applthermaleng.2005.02.012. [Online]. Available: https://www.sciencedirect.com/science/article/pii/S1359431105000785.

[46] T. Jaruwongwittaya and G. Chen, "Application of two stage ejector cooling system in a bus," *Energy Procedia*, vol. 14, pp. 187–197, 2012, 2011 2nd International Conference on Advances in Energy Engineering (ICAEE), ISSN: 1876-6102. DOI: https://doi.org/10.1016/j.egypro.2011.12.916. [Online]. Available: https://www.sciencedirect.com/science/article/pii/S1876610211043323.

[47] B. M. Anan, M. A. Kassem, and A. Hamed, "Comparison and performance analysis of single and double-stage in-series ejector refrigeration systems using various refrigerants," *Energy Conversion and Management*, vol. 313, p. 118 606, 2024, ISSN: 0196-8904. DOI: https://doi.org/10.1016/j.enconman.2024.118606. [Online]. Available: https://www.sciencedirect.com/science/article/pii/S0196890424005478.

[48] E. Ersayın and L. Ozgener, "Modeling and performance assessment of a combined geothermal-ejector refrigeration system," *Geothermics*, vol. 123, p. 103 120, 2024, ISSN: 0375-6505. DOI: https://doi.org/10.1016/j.geothermics.2024.103120. [Online]. Available: https://www.sciencedirect.com/science/article/pii/S0375650524002074.

[49] M. Parvez, O. Khan, S. Lal, and M. Ahmad, "Thermodynamic analysis of a solar-biomass cogeneration power and cooling by employing an ejector and single-effect absorption refrigeration system," *Biomass and Bioenergy*, vol. 184, p. 107 143, 2024, ISSN: 0961-9534. DOI: https://doi.org/10.1016/j.biombioe.2024.107143. [Online]. Available: https://www.sciencedirect.com/science/article/pii/S0961953424000965.

[50] K. Shestopalov, O. Khliyeva, V. Ierin, O. Konstantinov, N. Khliiev, G. Neng, and M. Kozminykh, "Novel marine ejector-compression waste heat-driven refrigeration system: Technical possibilities and environmental advantages," *International Journal of Refrigeration*, vol. 158, pp. 202–215, 2024, ISSN: 0140-7007. DOI: https://doi.org/10.1016/j.ijrefrig.2023.11.015. [Online]. Available: https://www.sciencedirect.com/science/article/pii/S014070072300436X.

[51] *United Nations Industrial Development Organization (UNIDO), Kigali Amendment to Montreal Protocol on substances that deplete the ozone layer*, 2016.

[52] A. Selvaraju and A. Mani, "Experimental investigation on R134a vapour ejector refrigeration system," *International Journal of Refrigeration*, vol. 29, no. 7, pp. 1160–1166, 2006, ISSN: 0140-7007. DOI: https://doi.org/10.1016/j.ijrefrig.2006.01.004. [Online]. Available: https://www.sciencedirect.com/science/article/pii/S0140700706000326.

[53] I. W. Eames, A. E. Ablwaifa, and V. Petrenko, “Results of an experimental study of an advanced jet-pump refrigerator operating with R245fa,” *Applied Thermal Engineering*, vol. 27, no. 17, pp. 2833–2840, 2007, ISSN: 1359-4311. DOI: https://doi.org/10.1016/j.applthermaleng.2006.12.009. [Online]. Available: https://www.sciencedirect.com/science/article/pii/S135943110600425X.

[54] T. Sankarlal and A. Mani, “Experimental studies on an ammonia ejector refrigeration system,” *International Communications in Heat and Mass Transfer*, vol. 33, no. 2, pp. 224–230, 2006, ISSN: 0735-1933. DOI: https://doi.org/10.1016/j.icheatmasstransfer.2005.08.002. [Online]. Available: https://www.sciencedirect.com/science/article/pii/S0735193305001454.

[55] D. Butrymowicz, M. J. Bergander, K. Śmierciew, and J. Karwacki, “Ejector-based air conditioner utilizing natural refrigerants,” *International Refrigeration and Air Conditioning Conference, Paper 1052*, 2010. [Online]. Available: http://docs.lib.purdue.edu/iracc/1052.

[56] A. Khalid Shaker Al-Sayyab, A. Mota-Babiloni, and J. Navarro-Esbrí, “Novel compound waste heat-solar driven ejector-compression heat pump for simultaneous cooling and heating using environmentally friendly refrigerants,” *Energy Conversion and Management*, vol. 228, p. 113 703, 2021, ISSN: 0196-8904. DOI: https://doi.org/10.1016/j.enconman.2020.113703. [Online]. Available: https://www.sciencedirect.com/science/article/pii/S0196890420312279.

[57] Y. Fang, S. Croquer, S. Poncet, Z. Aidoun, and Y. Bartosiewicz, “Drop-in replacement in a R134 ejector refrigeration cycle by hfo refrigerants,” *International Journal of Refrigeration*, vol. 77, pp. 87–98, 2017, ISSN: 0140-7007. DOI: https://doi.org/10.1016/j.ijrefrig.2017.02.028. [Online]. Available: https://www.sciencedirect.com/science/article/pii/S0140700717300907.

[58] K. Śmierciew, J. Gagan, D. Butrymowicz, M. Łukaszuk, and H. Kubiczek, “Experimental investigation of the first prototype ejector refrigeration system with hfo-1234ze(e),” *Applied Thermal Engineering*, vol. 110, pp. 115–125, 2017, ISSN: 1359-4311. DOI: https://doi.org/10.1016/j.applthermaleng.2016.08.140. [Online]. Available: https://www.sciencedirect.com/science/article/pii/S1359431116315010.

[59] R. Suresh and S. P. Datta, “Drop-in replacement of conventional automotive refrigeration system to hybrid-ejector system with environment-friendly refrigerants,” *Energy Conversion and Management*, vol. 266, p. 115 819, 2022, ISSN: 0196-8904. DOI: https://doi.org/10.1016/j.enconman.2022.115819. [Online]. Available: https://www.sciencedirect.com/science/article/pii/S019689042200615X.

[60] H. Rostamnejad and V. Zare, “Performance improvement of ejector expansion refrigeration cycles employing a booster compressor using different refrigerants: Thermodynamic analysis and optimization,” *International Journal of Refrigeration*, vol. 101, pp. 56–70, 2019, ISSN: 0140-7007. DOI: https://doi.org/10.1016/j.ijrefrig.2019.02.031. [Online]. Available: https://www.sciencedirect.com/science/article/pii/S0140700719300817.

[61] A. U. Atmaca, A. Erek, and O. Ekren, “Investigation of new generation refrigerants under two different ejector mixing theories,” *Energy Procedia*, vol. 136, pp. 394–401, 2017, 4th International Conference on Energy and Environment Research ICEER 2017, ISSN: 1876-6102. DOI: https://doi.org/10.1016/j.egypro.2017.10.271. [Online]. Available: https://www.sciencedirect.com/science/article/pii/S1876610217352219.

[62] C. Mateu-Royo, J. Navarro-Esbrí, A. Mota-Babiloni, and Ángel Barragán-Cervera, “Theoretical performance evaluation of ejector and economizer with parallel compression configurations in high temperature heat pumps,” *International Journal of Refrigeration*, vol. 119, pp. 356–365, 2020, ISSN: 0140-7007. DOI: https://doi.org/10.1016/j.ijrefrig.2020.07.016. [Online]. Available: https://www.sciencedirect.com/science/article/pii/S0140700720303182.

[63] Ümit İşkan and M. Direk, “Experimental performance evaluation of the dual-evaporator ejector refrigeration system using environmentally friendly refrigerants of R1234ze(E), ND, R515a, R456a, and R516a as a replacement for R134a,” *Journal of Cleaner Production*, vol. 352, p. 131 612, 2022, ISSN: 0959-6526. DOI: https://doi.org/10.1016/j.jclepro.2022.131612. [Online]. Available: https://www.sciencedirect.com/science/article/pii/S095965262201229X.

[64] X. Wang, Y. Yan, B. Li, X. Hao, N. Gao, and G. Chen, “Prospect of solar-driven ejector-compression hybrid refrigeration system with low GWP refrigerants in summer of Guangzhou and Beijing,” *International Journal of Refrigeration*, vol. 117, pp. 230–236, 2020, ISSN: 0140-7007. DOI: https://doi.org/10.1016/j.ijrefrig.2020.04.035. [Online]. Available: https://www.sciencedirect.com/science/article/pii/S0140700720301912.

[65] Şaban Ünal, M. T. Erdinç, H. Akgün, and M. Bilgili, “Effects of alternative refrigerants on the ejector dimensions for single and dual ejectors enhanced bus air conditioning system,” *International Communications in Heat and Mass Transfer*, vol. 143, p. 106 685, 2023, ISSN: 0735-1933. DOI: https://doi.org/10.1016/j.icheatmasstransfer.2023.106685. [Online]. Available: https://www.sciencedirect.com/science/article/pii/S073519332300074X.

[66] V. Nair, “HFO refrigerants: A review of present status and future prospects.,” *International Journal of Refrigeration*, vol. 122, pp. 156–170, 2021, ISSN: 0140-7007. DOI: https://doi.org/10.1016/j.ijrefrig.2020.10.039. [Online].

Available: https://www.sciencedirect.com/science/article/pii/S014070072030459X.

[67] J. Mahmoudian, A. Rocchetti, F. Mazzelli, and A. Milazzo, "A heat-powered ejector chiller working with low-GWP fluid R1233zd(e) (Part 1: Experimental results)," *International Journal of Refrigeration*, vol. 121, pp. 1–9, 2021, ISSN: 0140-7007. DOI: https://doi.org/10.1016/j.ijrefrig.2020.10.015. [Online]. Available: https://www.sciencedirect.com/science/article/pii/S0140700720304254.

[68] B. Huang, J. Chang, C. Wang, and V. Petrenko, "A 1-D analysis of ejector performance," *International Journal of Refrigeration*, vol. 22, no. 5, pp. 354–364, 1999, ISSN: 0140-7007. DOI: https://doi.org/10.1016/S0140-7007(99)00004-3. [Online]. Available: https://www.sciencedirect.com/science/article/pii/S0140700799000043.

[69] Y. Zhu, W. Cai, C. Wen, and Y. Li, "Shock circle model for ejector performance evaluation," *Energy Conversion and Management*, vol. 48, no. 9, pp. 2533–2541, 2007, ISSN: 0196-8904. DOI: https://doi.org/10.1016/j.enconman.2007.03.024. [Online]. Available: https://www.sciencedirect.com/science/article/pii/S0196890407000957.

[70] A. Khalil, M. Fatouh, and E. Elgendy, "Ejector design and theoretical study of R134a ejector refrigeration cycle," *International Journal of Refrigeration*, vol. 34, no. 7, pp. 1684–1698, 2011, Ejector Technology, ISSN: 0140-7007. DOI: https://doi.org/10.1016/j.ijrefrig.2011.01.005. [Online]. Available: https://www.sciencedirect.com/science/article/pii/S0140700711000181.

[71] N. S. Kumar and K. T. Ooi, "One dimensional model of an ejector with special attention to fanno flow within the mixing chamber," *Applied Thermal Engineering*, vol. 65, no. 1, pp. 226–235, 2014, ISSN: 1359-4311. DOI: https://doi.org/10.1016/j.applthermaleng.2013.12.055. [Online]. Available: https://www.sciencedirect.com/science/article/pii/S1359431113009526.

[72] C. Shi, H. Chen, W. Chen, S. Zhang, D. Chong, and J. Yan, "1D model to predict ejector performance at critical and sub-critical operation in the refrigeration system," *Energy Procedia*, vol. 75, pp. 1477–1483, 2015, Clean, Efficient and Affordable Energy for a Sustainable Future: The 7th International Conference on Applied Energy (ICAE2015), ISSN: 1876-6102. DOI: https://doi.org/10.1016/j.egypro.2015.07.271. [Online]. Available: https://www.sciencedirect.com/science/article/pii/S1876610215010395.

[73] W. Chen, C. Shi, S. Zhang, H. Chen, D. Chong, and J. Yan, "Theoretical analysis of ejector refrigeration system performance under overall modes," *Applied Energy*, vol. 185, pp. 2074–2084, 2017, Clean, Efficient and Affordable Energy for a Sustainable Future, ISSN: 0306-2619. DOI: https://doi.org/10.1016/j.

apenergy.2016.01.103. [Online]. Available: https://www.sciencedirect.com/science/article/pii/S0306261916300915.

[74] B. Saleh, "Performance analysis and working fluid selection for ejector refrigeration cycle," *Applied Thermal Engineering*, vol. 107, pp. 114–124, 2016, ISSN: 1359-4311. DOI: https://doi.org/10.1016/j.applthermaleng.2016.06.147. [Online]. Available: https://www.sciencedirect.com/science/article/pii/S1359431116310614.

[75] V. Kumar and G. Sachdeva, "1-d model for finding geometry of a single phase ejector," *Energy*, vol. 165, pp. 75–92, 2018, ISSN: 0360-5442. DOI: https://doi.org/10.1016/j.energy.2018.09.071. [Online]. Available: https://www.sciencedirect.com/science/article/pii/S0360544218318358.

[76] H. Guo, L. Wang, and X. Wang, "A full operating conditions ejector model for refrigeration systems driven by low-grade heat sources," *Case Studies in Thermal Engineering*, vol. 60, p. 104 670, 2024, ISSN: 2214-157X. DOI: https://doi.org/10.1016/j.csite.2024.104670. [Online]. Available: https://www.sciencedirect.com/science/article/pii/S2214157X24007019.

[77] H. Zhu, J. Liu, J. Yu, and P. Yang, "Compound-choking theory and artificial neural networks-based hybrid modeling for supersonic ejectors," *International Journal of Heat and Mass Transfer*, vol. 228, p. 125 616, 2024, ISSN: 0017-9310. DOI: https://doi.org/10.1016/j.ijheatmasstransfer.2024.125616. [Online]. Available: https://www.sciencedirect.com/science/article/pii/S0017931024004472.

[78] H. Zhu, J. Liu, J. Yu, and P. Yang, "Artificial neural network-based predictive model for supersonic ejector in refrigeration system," *Case Studies in Thermal Engineering*, vol. 49, p. 103 313, 2023, ISSN: 2214-157X. DOI: https://doi.org/10.1016/j.csite.2023.103313. [Online]. Available: https://www.sciencedirect.com/science/article/pii/S2214157X23006196.

[79] J. Van den Berghe, B. R. Dias, Y. Bartosiewicz, and M. A. Mendez, "A 1D model for the unsteady gas dynamics of ejectors," *Energy*, vol. 267, p. 126 551, 2023, ISSN: 0360-5442. DOI: https://doi.org/10.1016/j.energy.2022.126551. [Online]. Available: https://www.sciencedirect.com/science/article/pii/S0360544222034387.

[80] A. Mwesigye and S. B. Dworkin, "Performance analysis and optimization of an ejector refrigeration system using alternative working fluids under critical and subcritical operation modes," *Energy Conversion and Management*, vol. 176, pp. 209–226, 2018, ISSN: 0196-8904. DOI: https://doi.org/10.1016/j.enconman.2018.09.021. [Online]. Available: https://www.sciencedirect.com/science/article/pii/S0196890418310161.

[81] S. Aphornratana, S. Chungpaibulpatana, and P. Srikhirin, “Experimental investigation of an ejector refrigerator: Effect of mixing chamber geometry on system performance,” *International Journal of Energy Research*, vol. 25, no. 5, pp. 397–411, 2001.

[82] E. W. Lemmon, I. H. Bell, M. L. Huber, and M. O. McLinden, *NIST Standard Reference Database 23: Reference Fluid Thermodynamic and Transport Properties-REFPROP, Version 10.0, National Institute of Standards and Technology*, 2018. DOI: `https://doi.org/10.18434/T4/1502528`. [Online]. Available: `https://www.nist.gov/srd/refprop`.

[83] R. D. Zucker and O. Biblarz, *Fundamentals of gas dynamics*. John Wiley & Sons, 2019.

[84] H. Schlichting and J. Kestin, *Boundary layer theory*. Springer, 1961, vol. 121.

[85] S. Elbel and P. Hrnjak, “Experimental validation of a prototype ejector designed to reduce throttling losses encountered in transcritical R744 system operation,” *International Journal of Refrigeration*, vol. 31, no. 3, pp. 411–422, 2008, ISSN: 0140-7007. DOI: `https://doi.org/10.1016/j.ijrefrig.2007.07.013`. [Online]. Available: `https://www.sciencedirect.com/science/article/pii/S0140700707001508`.

[86] M. A. Branch, T. F. Coleman, and Y. Li, “A subspace, interior, and conjugate gradient method for large-scale bound-constrained minimization problems,” *SIAM Journal on Scientific Computing*, vol. 21, no. 1, pp. 1–23, 1999. DOI: `10.1137/S1064827595289108`. [Online]. Available: `https://doi.org/10.1137/S1064827595289108`.

[87] R. P. Brent, “Algorithms for minimization without derivatives,” in G. Forsythe, Ed. Englewood Cliffs, New Jersey: Prentice - Hall, 1973, ch. 3-4, pp. 19–60.

[88] W. McKinney, “Data Structures for Statistical Computing in Python,” in *Proceedings of the 9th Python in Science Conference*, Stéfan van der Walt and Jarrod Millman, Eds., 2010, pp. 56 –61. DOI: `10.25080/Majora-92bf1922-00a`.

[89] H. Lee, “Compact heat exchangers,” in *Thermal Design*. John Wiley & Sons, Ltd, 2010, ch. 5, pp. 240–381, ISBN: 9780470949979. DOI: `https://doi.org/10.1002/9780470949979.ch5`. [Online]. Available: `https://onlinelibrary.wiley.com/doi/abs/10.1002/9780470949979.ch5`.

[90] J. Zhang, A. Desideri, M. R. Kærn, T. S. Ommen, J. Wronski, and F. Haglind, “Flow boiling heat transfer and pressure drop characteristics of R134a, R1234yf and R1234ze in a plate heat exchanger for organic Rankine cycle units,” *International Journal of Heat and Mass Transfer*, vol. 108, pp. 1787–1801, 2017, ISSN: 0017-9310. DOI: `https://doi.org/10.1016/j.ijheatmasstransfer.2017.01.026`. [Online]. Available: `https://www.sciencedirect.com/science/article/pii/S0017931016335025`.

[91] A. S. Wanniarachchi, U. Ratnam, B. E. Tilton, and K. Dutta-Roy, “Approximate correlations for chevron-type plate heat exchangers,” in *Proc. 30th National Heat Transfer Conference*, vol. 12, HTD-Vol. 314, New York: ASME, 1995, pp. 145–151. [Online]. Available: https://www.osti.gov/biblio/445441.

[92] B. Thonon, R. Vidil, and C. Marvillet, “Recent research and developments in plate heat exchangers,” *Journal of Enhanced Heat Transfer*, vol. 2, no. 1-2, pp. 149–155, 1995, ISSN: 1065-5131.

[93] D. Lee, D. Kim, S. Park, J. Lim, and Y. Kim, “Evaporation heat transfer coefficient and pressure drop of R-1233zd(e) in a brazed plate heat exchanger,” *Applied Thermal Engineering*, vol. 130, pp. 1147–1155, 2018, ISSN: 1359-4311. DOI: https://doi.org/10.1016/j.applthermaleng.2017.11.088. [Online]. Available: https://www.sciencedirect.com/science/article/pii/S1359431117353280.

[94] W. Akers, H. Deans, and O. Crosser, “Condensing heat transfer within horizontal tubes, chem eng progr,” in *Symposium Ser. No. 29*, vol. 55, 1959.

[95] O. J. Kwon, J. H. Jung, and Y. T. Kang, “Development of experimental nusselt number and friction factor correlations for condensation of r-1233zd(e) in plate heat exchangers,” *International Journal of Heat and Mass Transfer*, vol. 158, p. 120 008, 2020, ISSN: 0017-9310. DOI: https://doi.org/10.1016/j.ijheatmasstransfer.2020.120008. [Online]. Available: https://www.sciencedirect.com/science/article/pii/S0017931020310644.

[96] J. Yang, A. Jacobi, and W. Liu, “Heat transfer correlations for single-phase flow in plate heat exchangers based on experimental data,” *Applied Thermal Engineering*, vol. 113, pp. 1547–1557, 2017, ISSN: 1359-4311. DOI: https://doi.org/10.1016/j.applthermaleng.2016.10.147. [Online]. Available: https://www.sciencedirect.com/science/article/pii/S1359431116326680.

[97] H. Martin, “A theoretical approach to predict the performance of chevron-type plate heat exchangers,” *Chemical Engineering and Processing: Process Intensification*, vol. 35, no. 4, pp. 301–310, 1996, ISSN: 0255-2701. DOI: https://doi.org/10.1016/0255-2701(95)04129-X. [Online]. Available: https://www.sciencedirect.com/science/article/pii/025527019504129X.

[98] P. Virtanen, R. Gommers, T. E. Oliphant, *et al.*, “SciPy 1.0: Fundamental Algorithms for Scientific Computing in Python,” *Nature Methods*, vol. 17, pp. 261–272, 2020. DOI: 10.1038/s41592-019-0686-2.

[99] C. R. Harris, K. J. Millman, S. J. van der Walt, *et al.*, “Array programming with NumPy,” *Nature*, vol. 585, no. 7825, pp. 357–362, Sep. 2020. DOI: 10.1038/s41586-020-2649-2. [Online]. Available: https://doi.org/10.1038/s41586-020-2649-2.

[100] J. D. Hunter, “Matplotlib: A 2d graphics environment,” *Computing in Science & Engineering*, vol. 9, no. 3, pp. 90–95, 2007. DOI: 10.1109/MCSE.2007.55.

[101] J. García del Valle, J. Saíz Jabardo, F. Castro Ruiz, and J. San José Alonso, "An experimental investigation of a r-134a ejector refrigeration system," *International Journal of Refrigeration*, vol. 46, pp. 105–113, 2014, ISSN: 0140-7007. DOI: `https://doi.org/10.1016/j.ijrefrig.2014.05.028`. [Online]. Available: `https://www.sciencedirect.com/science/article/pii/S0140700714001406`.

[102] J. Smolka, Z. Bulinski, A. Fic, A. J. Nowak, K. Banasiak, and A. Hafner, "A computational model of a transcritical R744 ejector based on a homogeneous real fluid approach," *Applied Mathematical Modelling*, vol. 37, no. 3, pp. 1208–1224, 2013, ISSN: 0307-904X. DOI: `https://doi.org/10.1016/j.apm.2012.03.044`. [Online]. Available: `https://www.sciencedirect.com/science/article/pii/S0307904X12002077`.

[103] R. Storn and K. Price, "Differential evolution - a simple and efficient heuristic for global optimization over continuous spaces," *Journal of Global Optimization*, vol. 11, pp. 341–359, Jan. 1997. DOI: `10.1023/A:1008202821328`.

[104] H. Li, F. Cao, X. Bu, L. Wang, and X. Wang, "Performance characteristics of R1234yf ejector-expansion refrigeration cycle," *Applied Energy*, vol. 121, pp. 96–103, 2014, ISSN: 0306-2619. DOI: `https://doi.org/10.1016/j.apenergy.2014.01.079`. [Online]. Available: `https://www.sciencedirect.com/science/article/pii/S0306261914001093`.

Abstract

Rising electricity prices and environmental regulations make it increasingly economically justified to utilize low-temperature waste heat generated as a by-product of many technological processes. One of the potential applications to convert waste heat into cooling capacity using an ejector refrigeration system. Despite numerous descriptions in the literature, such systems have not found industrial applications up to date. In order to implement this technology in industry, a number of tests are needed, including those involving the operation of the ejector refrigeration systems under real conditions of industrial waste heat supply. Practical tools for the design of the devices in question must be also developed. This study delves into the development and validation of a comprehensive mathematical model for an ejector refrigeration system, specifically focusing on the design and selection of components for efficient operation.

The research involved developing a 0-D ejector and plate heat exchanger models, incorporating key parameters such as geometry, fluid properties, and efficiencies to predict performance under various operating conditions. The model was rigorously tested and validated against experimental data from two prototype systems driven by the waste heat of 200 kW and 600 kW built and tested under real industrial conditions. These prototypes utilized the low GWP and low-pressure HFO refrigerant R1233zd(E) for waste heat recovery, showcasing the feasibility of this environmentally friendly refrigerant in the ejector refrigeration systems, especially for high-temperature cooling. The well-calibrated ejector model, along with the plate heat exchanger models, which are the most important components of the ejector cooling system, confirmed their accuracy and usefulness for design purposes. The ejector component characteristic efficiencies were optimized for the ejector calculation model, and ejector key performance parameters were estimated to be highly accurate. The average relative error in the estimation was 5.0%, 5.6%, and 15.6% for the mass entrainment ratio, pressure ratio, and ejector total efficiency, respectively. The ejector model accuracy was highly sensitive to the correct estimation of the mixing loss coefficient. The research also highlighted the importance of utilizing experimental data from similar superheat conditions to accurately estimate fixed ejector coefficients during the design process. Also, the plate heat exchanger models were considered accurate, giving the relative error of estimation of the outlet temperatures and heat transfer rates below 10% for most cases. The resulting accuracy is sufficient from the perspective of refrigeration system design.

The study revealed significant challenges associated with using the low-pressure

R1233zd(E) refrigerant, specifically the sensitivity of the system performance to pressure drops. Given this fact, several measures to reduce pressure losses were taken, and several refrigeration system configurations were tested. A refrigeration system operating with R1233zd(E) was also compared with high-pressure R1234ze(E).

The satisfying performance of the refrigeration system using R1233zd(E) was confirmed for high-temperature cooling conditions, equivalent to the glycol temperature of 16°C/19°C (outlet/inlet of the evaporator), where the COP was 0.25 under critical operating parameters. However, using this refrigerant requires several steps to reduce the minimum pressure loss in the refrigeration system. For standard cooling conditions, equivalent to the glycol temperature of 6°C/12°C (outlet/inlet of the evaporator) requiring higher pressure ratios, the system operating with R1234ze(E) refrigerant achieved better performance, where COP reached 0.25.

Streszczenie

Rosnące ceny energii elektrycznej i przepisy dotyczące ochrony środowiska sprawiają, że wykorzystanie niskotemperaturowego ciepła odpadowego generowanego jako produkt uboczny wielu procesów technologicznych staje się coraz bardziej uzasadnione ekonomicznie. Jednym z potencjalnych sposobów jego zagospodarowania, jest jego wykorzystanie do wytworzenia wydajnośc chłodniczej za pomocą strumienicowego układu chłodniczego, który może zastąpić konwencjonalne systemy chłodzenia zużywające energię elektryczną. Pomimo licznych opisów w literaturze, takie systemy nie znalazły do tej pory zastosowań przemysłowych. W celu wdrożenia tej technologii w przemyśle potrzebne jest wykonanie wielu badań implementacyjnych, w tym obejmujących pracę strumienicowych urządzeń chłodniczych w rzeczywistych warunkach zasilania przemysłowym ciepłem odpadowym. W dalszym etapie istnieje również potrzeba opracowania efektywnych narzędzi do projektowania omawianych urządzeń. Niniejsza praca dotyczy opracowania i walidacji kompleksowego modelu matematycznego dla strumienicowego układu chłodniczego, w szczególności koncentrując się na projektowaniu i doborze komponentów do wydajnej pracy.

Badania obejmowały opracowanie modeli 0-D strumienicy i modeli płytowych wymienników ciepła z uwzględnieniem kluczowych parametrów, takich jak geometria, właściwości płynu i wydajność w celu określenia wydajności w różnych warunkach pracy. Model został przetestowany i zweryfikowany w oparciu o dane eksperymentalne z dwóch prototypowych systemów napędzanych ciepłem odpadowym o mocy 200 kW i 600 kW, zbudowanych i przetestowanych w rzeczywistych warunkach przemysłowych. Prototypy te wykorzystywały niskociśnieniowy czynnik chłodniczy HFO R1233zd(E) o niskim GWP do odzyskiwania ciepła odpadowego. Przeprowadzone badania wskazały na możliwą wydajną pracę strumienicowych układów chłodniczych, wykorzystujących ten przyjazny dla środowiska czynnik chłodniczy, zwłaszcza do chłodzenia wysokotemperaturowego. Dobrze skalibrowany model strumienicy wraz z modelami płytowych wymienników ciepła, które są najważniejszymi komponentami strumienicowego układu chłodzenia, potwierdziły swoją dokładność i przydatność do celów projektowych. Charakterystyczne sprawności komponentów strumienicy zostały zoptymalizowane dla modelu obliczeniowego, a kluczowe parametry wydajności strumienicy zostały oszacowane z dużą dokładnością. Średni błąd względny oszacowania wynosił 5,0%, 5,6% i 15,6% odpowiednio dla stosunku eżekcji, stosunku sprężania i całkowitej sprawności strumienicy. Dokładność modelu strumienicy była bardzo wrażliwa na

prawidłowe oszacowanie sprawności komory mieszania strumienicy. Badania podkreśliły również znaczenie wykorzystania danych eksperymentalnych o podobnych warunkach przegrzania na dolocie strumienicy w celu dokładnego oszacowania stałych współczynników modelu podczas procesu projektowania. Ponadto modele płytowych wymienników ciepła zostały uznane za dokładne, dając względny błąd oszacowania temperatur wylotowych i strumieni wymienionego ciepła poniżej 10% dla większości przypadków. Uzyskana dokładność jest wystarczająca z punktu widzenia projektowania systemów chłodniczych.

Badanie ujawniło znaczące wyzwania związane ze stosowaniem niskociśnieniowego czynnika chłodniczego R1233zd(E), w szczególności wrażliwość wydajności systemu na spadki ciśnienia. Biorąc pod uwagę ten fakt, w pracy podjęto szereg działań w celu zmniejszenia strat ciśnienia i przetestowano kilka konfiguracji układu chłodniczego. Układ chłodniczy pracujący z czynnikiem R1233zd(E) został również porównany z wysokociśnieniowym czynnikiem R1234ze(E).

Zadowalająca wydajność układu chłodniczego wykorzystującego R1233zd(E) została potwierdzona dla wysokotemperaturowych warunków chłodzenia, równoważnych temperaturze glikolu 16°C/19°C (wylot/wlot parownika), gdzie współczynnik COP wynosił 0,25 przy krytycznych parametrach roboczych. Jednak użycie tego czynnika chłodniczego wymaga kilku prac w celu zmniejszenia minimalnej straty ciśnienia w układzie chłodniczym. W przypadku standardowych warunków chłodzenia, równoważnych temperaturze glikolu 6°C/12°C (wylot/wlot parownika) wymagających wyższych stosunków ciśnień, system działający z czynnikiem chłodniczym R1234ze(E) osiągnął lepszą wydajność, gdzie COP wynosiło 0,25.